Brightest Cluster Galaxies: Optical Properties at Intermediate Redshift

by

Christopher John Bildfell
B.Sc., University of Western Ontario, 2003

A Thesis submitted in Partial Fulfillment of the
Requirements for the Degree of

MASTER OF SCIENCE

in the

DEPARTMENT OF PHYSICS AND ASTRONOMY

Supervisory Committee

Brightest Cluster Galaxies: Optical Properties at Intermediate Redshift

by

Christopher John Bildfell
B.Sc., University of Western Ontario, 2003

Supervisory Committee

Dr. A. Babul, (Department of Physics and Astronomy)

Co-Supervisor

Dr. H. Hoekstra, (Department of Physics and Astronomy)

Co-Supervisor

Dr. A. G. Brolo, (Department of Chemistry)

Outside Member

Dr. F. Diacu, (Department of Mathematics)

External Examiner

Supervisory Committee:

Dr. A. Babul, Co-Supervisor (Department of Physics and Astronomy)

Dr. H. Hoekstra, Co-Supervisor (Department of Physics and Astronomy)

Dr. A. Brolo, Outside Member (Department of Chemistry)

Dr. F. Diacu, External Examiner (Department of Mathematics)

Abstract

Galaxies grow and evolve via the repeated process of hierarchical merging, with smaller galaxies being cannibalized by larger and correspondingly brighter ones. Thus in galaxy clusters it is the brightest cluster galaxy (BCG) that lies at the top of the galaxian food chain and deep within the cluster potential the BCG grows to become one of the most massive galaxies in the universe. Baryonic feedback processes associated with the formation of the BCG (eg., AGN, star formation, stellar winds and chemical enrichment) affect the balance between heating and cooling of the intra-cluster medium (ICM) which in turn, through replenishment of the cold gas reservoir of the BCG, feeds back on these processes. This interconnection between the BCG and the state of the cluster gas has direct implications for theories of both galaxy and cluster evolution. Thanks to recent advances in observational techniques it has become possible to study the link between BCG and host cluster properties across a wide range of multi-wavelength information. Using deep imaging data taken with the Canada-France-Hawaii Telescope as part of the Canadian Cluster Comparison Project (CCCP), we examine the surface brightness distributions in g' and r' of 28 BCGs in a redshift range $0.15 \lesssim z \lesssim 0.55$ residing in massive clusters with $T_x \geq 5$ and compare them to the global X-ray properties of their hosts.

We fit $R^{1/4}$ models to the surface brightness profiles and find that the Kormendy relation of BCGs, when corrected for passive evolution, is consistent with that of the local elliptical population. We identify a subset of BCGs with extraordinarily blue centers ($0.1 < dlog(g' - r')/dlog(r) < 1.3$ within 15 h_{70}^{-1} kpc) extending several times the fwhm of the psf. These objects all lie on the most luminous side of the scatter in the L_x-T_x relation for a given T_x, an effect which previous authors have shown can be explained by cooling of the ICM (McCarthy et al. 2004). We find independent evidence from previous studies that these systems are all hosts of recent star formation. The blue cores in these BCGs cause them to be displaced from the red sequences of their host clusters; in the most extreme cases this displacement is $\sim 1mag$. These findings are contradictory to the current paradigm of elliptical galaxy formation within clusters where star formation is thought to have a negligible effect in the most massive cluster ellipticals at late cosmic times. Furthermore BCG total magnitude is found to correlate with host cluster deviation from the mean L_x-T_x relation. We argue that cooling and pre-heating of the Intra-Cluster-Medium has an important affect on the global and structural properties of the stellar component of BCGs. Not all BCGs are red and dead, there is a need to incorporate an external source of cold gas replenishment into quenching models of galaxy formation in clusters in order to reconcile these observations.

Table of Contents

List of Tables

List of Figures

Acknowledgments

There are many jobs in this world. Some people are lawyers or doctors, some people sell tickets from inside a booth, some people wash the elephants at the zoo and some people sew the little labels onto the insides of my shirts. I study astronomy. Not a day goes by that I don't think about how wonderful my job is and how lucky I am to have been given this amazing opportunity to unravel the mysteries of the cosmos on a regular basis and get paid for it. Of course there are many, many people who have helped me obtain such an opportunity to whom I am very grateful and there is absolutely no way that I could have gotten this far on my own. As I sit here and write these acknowledgments the list of people who I can think to thank grows on and on and so although I will try to remember you all, I apologize in advance if I have left anyone out. For those of you that don't appear here but should, please feel free to slap me in the face (lightly) or kick me in the shins (softly) the next time we meet.

First off, I would like to thank the Universe. You've been so mysterious and so fantastically interesting. The more I learn about you the more addicted I become to trying to understand you. You've been good to me so far (looking past some of those cruel pranks you've pulled... you know the ones) and if the next twenty years are half as good as the last, we're in for some great times together old buddy.

Well, sorry about that, Reader. The remainder of these acknowledgments will be dedicated to thanking real people; and here goes.

To my co-supervisors, thank you both for sticking with me and guiding me to where I am today. I have learned so much from your teachings and I am truly fortunate to have been working under the weight of so much talent. Thanks Arif, for showing me how to see the whole picture and ask the right questions. Thanks Henk, for having the patience to go through all the gory details (line-by-line).

Thanks go out to the remainder of my thesis committee. To Dr. Alexandre

Brolo for your years of service and to Dr. Florin Diacu for acting as the external examiner on such short notice.

I had no idea how much administrative red-tape there was associated with being in graduate school. There are always so many forms to fill out, things to register for, events to remember and attend and the occasional cheque to be reminded to pick up. Luckily these little bumps in the road were all navigated smoothly throughout my degree thanks to the amazing job of the graduate student secretaries. Thank you Joy, thank you Rosemary and thank you Geri. I should probably also mention Susan Gnucci here as well, thanks for all the accounting services and reminding me when it was time for a haircut.

Thanks to Stephenson Yang for healing my computer when it was sick, helping my files find their way when they were lost and smacking some sense into any program that started acting up. The department would crumble without you. Thanks to Stephanie Yang for bringing some of that youthful attitude around and cutting through all the stuffiness. Thanks Russ Robb for all your helpful teaching advice and for putting up with all of my whining about "this lab has such-and-such problem!", "We're all out of overhead markers!" and other favorites.

Thanks go out to Jon Willis and Luc Simard for all the helpful discussion and project advice. Thanks to Andiseh Mahdavi for collaborating and helping to improve the quality of my work. Thanks to Steven Gwyn for your help with fitsio, fortran, supermongo and other geeky stuff.

Thank you Ian McCarthy (sigh...). You're were a good office-mate and I'm grateful for the many valuable discussions we've had over the years about science. But I'm probably more grateful for all the discussions we've had that were not about science. You're a real pal, even though I own you in the post, this one's for you, bud.

To Greg Poole, thanks for the useful discussions and office distractions.

To Jeff Stoesz, thanks for always making time when you were busy and I had

questions. Thanks for all the stuff you left me when you moved to Italy. You're a great guy Jeff and a real friend.

To Eric Hsiao, thanks for the science talk and help with K-corrections. You're an IDL master!

Thanks to Pho Hoa for being the only restaurant in victoria that's open late and doesn't cost me a month's salary.

To Robin, Reyna, Brady and Jim, I'm indebted to all of you for providing an outlet for me unwind from the rigors of grad student life.

To Richard Liang, the godfather of little-Windsor Vancouver chapter. Always hospitable, my guide to the city and an old friend in the pioneer days on the west coast. To many more dim sum dumplings and random drop-ins for years to come.

To Katy Fraser and Shiela Hollanders and the good time after-school pop-bys. Thanks for the curry girls. The village just wasn't the same after you left.

To the Pagliacci's boys, Chris Simard, Matt Howe and Mike Hollier, I apologize for making you feel that your hoops skills were inadequate at times but such is the way of all things. Thanks for the games guys.

Thanks go out to my second family: Andrew Tesolin, Kristen Stockstill, Jeff Donaldson, Jeanie Di Giacomo, Aaron Walsh and Sarah Choi. You are my support group on the island. Thanks for being there, I hope I have the chance to repay all those favors.

To Dave Tesolin, thanks for putting up with me at 611. Here's to summer BBQs and scary haunted houses.

To my loving family. All my grandparents, aunts, uncles and cousins. I couldn't imagine belonging to any other group of people that would have given me as rich an experience as all of you have. And especially to my sister, Gudrin, and all four of my parents: Linda, Dave, Ron and Erin. Thank you for caring so much and helping me become the well-adjusted member of society that I am today. Thank you for all your support. Perhaps someday I can repay you, but most likely not, so

don't get too excited.

Finally, thanks to Anudeep Kanwar. You're a shining star on a cloudy night, a character in the cast of so many wonderful memories and companion on a fantastic voyage of culinary exploration. Thanks for all the surprises and everything else.

Chapter 1 | *Introduction*

1.1 Galaxy Formation

We stand at the dawn of a new era of understanding our place in the universe. Over the past hundred years or so the evolution of astronomy and astrophysics has proceeded at a constantly quickening pace. Theoretical and observational advancements have proceeded in lock-step, primarily driven by technological progress. Construction of powerful observatories, development of modern computing, photographic imaging and analysis techniques have been the main driving forces. In only a century we have transformed our accepted view of the universe from one which is nicely confined to the borders of our galaxy to the current picture of an infinite universe, containing billions of galaxies within our observable horizon, which is expanding at an ever increasing, yet not alarming rate.

It was Edwin Hubble and his development of the Hubble tuning-fork picture of galaxies that began the study of galaxy formation and evolution. Of course we now know that Hubble's original view of galactic evolution was backwards, it still remains today as a prominent way of classifying galaxy morphology. There have been many efforts since to try to fit the wide range of observed galaxy morphologies into a coherent picture of galactic evolution. The general consensus is that there are three main types: spheroids, disks and irregulars. With the aid of powerful computing facilities we have developed numerical simulations that help us understand the dynamical differences between the various galaxy morphological types. Disk galaxies are thought to form naturally from rotating gaseous systems while

spheroids are thought to be the result of violent merger events between multiple smaller systems. We also understand from the dynamics of the different galaxy types that there must be a significant amount of non-luminous dark matter present within them in order to explain their shapes. These and many other properties of galaxies are well integrated into the modern paradigm of galactic systems.

Yet despite all of the obvious successes that have been achieved in this field there are still many outstanding questions. The existence of galaxy scaling relations such as the Tully-Fisher relation for disk galaxies, the Fundamental Plane relation for spheroids as well as the Magorrian relation for galactic bulges pose a set of new challenges to our understanding. These tightly obeyed, empirical scalings laws between the seemingly independent dynamical variables of galaxies are created by the interaction between gravitational processes and non-gravitational feedback. Although these scalings are always obeyed in the formation and evolution of galaxies, we do not understand the highly complex interaction of all the relevant processes that conspires to create these simple relations.

In order to understand the nature and importance of the relevant formation processes (hierarchical merging, gas physics, star formation, stellar winds, heating from Active Galactic Nuclei (AGN), black-hole accretion, etc.) we can use the observed galaxy scaling laws as guides. Through the study of how these processes affect the scaling relations and the observed structure within them we can assess the influence of each and their dependence upon one another. Only when we fully understand the details of all physical processes required to build galaxies can we be satisfied that we have discovered a complete model of galaxy formation.

We are most interested in galaxies which evolve in the extreme environments of deep cluster gravitational potentials. In these systems there is an opportunity to observe the effects of enhanced merging, gas cooling and AGN feedback on the formation of massive elliptical galaxies. Through careful examination of their optical properties as well as correlation with their host cluster X-ray properties, we hope

to gain some useful insight towards the roles of these galaxy-building processes.

1.2 Brightest Cluster Galaxies

This work examines in detail the optical properties of Brightest Cluster Galaxies (BCGs), the most massive galaxies in the universe. These galaxies typically lie deep within the cluster potential where high merger rates propel them to the top of the galaxy food chain. We are concerned with the global and structural properties of these extreme and exotic objects. Through careful examination of these properties, as well as their evolution and relevant scaling relations, we hope to uncover clues that will contribute to the currently accepted models of galaxy formation. The currently accepted standard picture of BCGs is that they are old, red, gas free systems, representing the highest end of the galaxy mass function.

The member galaxies of a given cluster typically lie together in the galaxy color-magnigtude diagram along a locus called the red sequence (eg. Gladders & Yee 2005). BCGs are often selected as the brightest galaxies lying on their host cluster's red sequence. Many BCGs, but not all, are the cD type galaxies which are typically centrally located within the cluster and possess a large, extended stellar envelope. We note that while not all clusters will have a cD galaxy, which tend to be a product of the later relaxed stages of cluster evolution, all cluster will contain a brightest member (ie. the BCG).

There is growing evidence that BCGs comprise a special population of galaxies separate from the rest of the massive ellipticals (Kormendy & Bender 1996; Postman et al. 1995; Faber et al 1997; Ravindranath et al 2001; Patel et al. 2006). The distinction of BCGs from the remainder of the massive elliptical population is most likely due to the BCGs forming in the high density environments found in the centers of rich galaxy clusters. In these central regions, high baryon concentrations lead to enhanced non-gravitational feedback processes (AGN, radiative cooling, stellar

winds, etc.). In addition, because BCGs tend to form from mergers of galaxies with initial velocities that are aligned with the direction of nearby cosmic filaments, they are constructed from a merging satellite population that may have drastically different orbit parameters than those that go into building their more common elliptical cousins.

The work presented here is part of an attempt to investigate the uniqueness of BCGs as evidenced by their optical properties and to examine how they correlate with their host cluster's X-ray properties. The results have implications for theories of galaxy evolution as well as the connection between BCG formation and the evolution of the ICM.

Chapter 2 | *Data*

The data used for this work are a part of the Canadian Cluster Comparison Project (CCCP). The CCCP is a mainly X-ray selected sample of 50 galaxy clusters. The sample is selected from the ASCA cluster catalogue of Horner (2001) and satisfies the criteria that X-ray temperature of each cluster $T_x > 5keV$ and that the redshift of each cluster is in the range $0.15 \leq z \leq 0.55$. Deep optical imaging data was obtained on these clusters using the Canada-France-Hawaii Telescope (CFHT). The full sample comprises a set of 30 clusters observed in the g' and r' filters and 20 clusters observed in the B and R filters. The analysis presented here is based on the subset of 30 clusters with g' and r' data. These data were acquired using the MegaCam instrument; a 36 CCD mosaic that covers a square degree on the sky in 340 megapixels giving it a resolution of 0.186 arcseconds per pixel. MegaCam is an excellent instrument for studying galaxy clusters because it facilitates the observation of both large-scale ($\sim Mpc$) and small-scale ($\sim kpc$) spatial variations in their optical properties with unprecedented depth coverage.

The primary goal of the CCCP is to use weak gravitational lensing to probe the relationships between cluster baryonic mass tracers and variation in the properties of the hot Intra-Cluster Medium (ICM). In particular, the survey is designed to examine the scatter in X-ray cluster scaling laws (eg. $M - T, L_x - T$) and relate this scatter to the lensing masses. The CCCP sample is unique. No optical survey of galaxy clusters can match its depth, with $\mu_{lim,1\sigma} \sim 26\ mag/(")^2$ in both g' & r', and redshift coverage $z \sim [0.15, 0.55]$. While this data set is primarily obtained to measure cluster weak-lensing masses, it also holds the potential to answer many of the outstanding questions that persist about the formation and evolution of galaxies

Table 2.1: Image Parameters for the Selected CCCP Data

Name	$\mu_{sky,g'}$	$\mu_{lse,g'}$	$\mu_{sky,r'}$	$\mu_{lse,r'}$	$t_{exp,g'}$	$t_{exp,r'}$
3C295	26.73	28.73	26.58	27.88	4 × 600s	12 × 600s
Abell 115	26.45	26.68	26.38	25.67	4 × 450s	8 × 600s
Abell 223a	26.38	26.22	26.13	25.26	4 × 450s	8 × 600s
Abell 223b	26.50	26.86	26.08	25.23	4 × 450s	8 × 600s
Abell 520	26.28	25.44	26.14	24.31	4 × 450s	8 × 600s
Abell 521	26.40	26.55	26.36	25.38	4 × 450s	8 × 600s
Abell 586	26.32	23.76	24.96	23.22	4 × 450s	8 × 600s
Abell 611	26.47	26.68	26.36	25.14	4 × 450s	8 × 600s
Abell 697	26.54	26.46	26.45	25.74	4 × 450s	8 × 600s
Abell 851	26.36	26.90	26.43	26.29	4 × 600s	12 × 600s
Abell 959	26.39	27.08	26.28	25.31	4 × 450s	8 × 600s
Abell 1234	26.27	26.75	26.17	25.48	4 × 450s	8 × 600s
Abell 1246	26.39	27.09	26.28	25.86	4 × 450s	8 × 600s
Abell 1758b	26.72	28.71	26.55	28.55	4 × 450s	8 × 600s
Abell 1835	26.42	25.45	26.25	24.61	4 × 450s	8 × 600s
Abell 1914	26.77	28.09	26.34	27.68	4 × 450s	8 × 600s
Abell 1942	26.44	26.05	26.23	24.95	4 × 450s	8 × 600s
Abell 2104	26.56	26.13	26.47	25.13	4 × 450s	8 × 600s
Abell 2111	26.63	26.61	26.36	25.37	4 × 450s	8 × 600s
Abell 2163	26.53	25.87	26.25	25.05	4 × 450s	8 × 600s
Abell 2204	25.77	22.86	25.75	22.35	4 × 450s	8 × 600s
Abell 2259	26.50	26.34	26.24	24.81	4 × 450s	8 × 600s
Abell 2261	26.53	26.51	26.39	25.43	4 × 450s	8 × 600s
Abell 2537	26.72	26.60	26.16	25.39	4 × 450s	8 × 600s
CL0910+41	26.64	27.09	26.51	25.90	4 × 600s	12 × 600s
CL1938+54	26.37	25.22	26.12	24.30	4 × 450s	8 × 600s
MS0440+02	26.56	24.59	26.11	23.46	4 × 450s	8 × 600s
MS0451-03	26.47	26.56	26.42	26.03	4 × 600s	12 × 600s
MS1008-12	26.14	24.12	25.92	22.76	4 × 450s	8 × 600s
RXJ1347.5-1145	26.65	26.55	26.35	25.58	4 × 600s	12 × 600s

Image parameters of the selected clusters from the CCCP. The quantities μ_{sky} and μ_{lse} are the g' and r' 1σ limiting magnitudes and large-scale-errors respectively; both quantities are measured in $mag/"^2$. Exposure times are also listed. Clusters with z < 0.4 were observed for 4 × 450s in g' and 8 × 600s in r' while clusters with z > 0.4 were observed for 4 × 600s in g' and 8 × 600s in r'.

within dense cluster environments.

The cosmological parameters used throughout this work are $h = 0.7$, $\Omega_m = 0.3$ and $\Lambda = 0.7$.

2.1 BCG Selection

The task of identifying the BCG in each cluster is critical to the success of this study. For the majority of the clusters in our sample this task is an easy one. These are the systems which contain cD galaxies. These conspicuous galaxies are easily outshine the rest of the cluster members in the optical wavelengths studied here and often contain large, extended envelopes of stars. It is the clusters which do not contain obvious cD galaxies which pose a potential problem.

There are some clusters for which we have two or even three potential BCG candidates. In order to select one of these candidates over another we must further specify that the BCG of interest is the candidate galaxy which is most influenced by the cluster's gravitational potential throughout its evolutionary history. This additional qualification allows us to take advantage of some of the outstanding X-ray observations that are available in the Chandra and XMM-Newton archives. In order to single out the BCG candidate galaxy most influenced by its extreme cluster environment in these questionable cases we select the candidate that sits closest to the X-ray centroid of its host cluster. For a relaxed cluster, we expect the X-ray centroid to trace the deepest point in the cluster potential. In the following discussion we describe the systems with multiple BCG candidates and outline the reasoning used in the final BCG selection.

• Abell 520: This cluster has a highly disturbed X-ray morphology indicative of a major merger. There are two BCG candidates lying on the outskirts of the cluster X-ray contours. The NE candidate is chosen as the BCG over the SW candidate because it lies closer to the centroid of the overall X-ray distribution. The SW

BCG candidate is associated with a group having an average line-of-sight rest-frame velocity of 465 km s^{-1} and the NE BCG candidate has an average line-of-sight rest-frame velocity of 67 km s^{-1} which is closer to the main group's average line-of-sight rest-frame velocity of -740 km s^{-1} (Mahdavi et al. 2007 in prep.). The evidence from kinematic and X-ray morphology point to the NE candidate as the BCG but given the fact that these two galaxies are separated at such large distances it may be interesting to treat them both as BCGs in separate sub-clusters. We will explore this further in future work.

• Abell 851 contains several candidate BCGs. We narrow the selection to a closely spaced group of three bright galaxies that lie nearest the centre of X-ray emission in an XMM-Newton 24 ks exposure. Of these three remaining candidates we select the southernmost galaxy as the BCG because it appears to have the largest extended stellar envelope. It is likely however that these three galaxies will merge into a single massive BCG as this highly disturbed system at $z = 0.41$ approaches a more dynamically relaxed state.

• Abell 959 also contains several BCG candidates. There are two galaxies in particular that lie at small projected distances from the X-ray peak. Of these two we choose the northernmost candidate as the BCG because it lies slightly closer to the X-ray centroid. It is worth mentioning here that this selection is somewhat uncertain because the X-ray image that is used to arrive at this selection is from Rosat which has a significantly lower resolution than the XMM-Newton and Chandra images used in some of our other BCG selection.

• Abell 1234: There are two potential BCG candidates in this clusters. They are identified as the NW candidate and the SE candidate. There is no available X-ray data for this cluster in either the XMM-Newton or Chandra archives. We select the NW candidate as the BCG because it is more centrally located within the cluster and it appears to have a slightly more extended stellar envelope.

• Abell 1246: This cluster contains two potential BCG candidates. These object

are overlapping on the sky and distinguished as the N candidate and S candidate. The S candidate has a higher peak surface brightness. The N candidate however has a position angle that is more aligned with the overall extended profile of these two components. The extended profile also seems to be more centered on the N candidate. We choose the N candidate as the BCG.

• Abell 1914: This cluster has two BCG candidates with on in the NE and the other in the SW. The SW candidate has a brighter peak surface brightness than the NE candidate but it lies further from the X-ray centroid by a significant margin. We choose the NE candidate as the BCG.

• Abell 2111: This cluster has a pair of BCG candidates. We select the N candidate as the BCG over the S candidate because it is closer to the X-ray peak (Chandra 10ks exposure) and it has a much more extended low surface brightness envelope.

• CL0910+41: This cluster has a very bright BCG that sits near the center of the optical light distribution (SDSSJ091345.5+405628). This galaxy is unlike many other BCGs in that it is compact, extremely blue in color and contains very little evidence of an extended stellar envelope. These differences raise the concern that this galaxy may be a foreground source that projects onto the cluster. Goto 2005 identifies this galaxy as a Hyper Luminous InfraRed Galaxy (HLIRG) with an infrared luminosity $L_{ir} > 10^{13} L_{\odot}$ at $z = 0.442$ which makes this galaxy a confirmed cluster member and validates our BCG selection in this case. The extraordinary properties of this galaxy as a BCG make particularly interesting. We discuss in later chapters how this galaxy fits with the rest of the BCG population within the CCCP sample and show that it is consistent with the rest of the sample forming a coherent and continuous picture of BCG formation.

2.2 Reduction

The initial data reduction and processing is performed on site at the observatory (CFHT) with the Elixir automated instrument and software pipeline. Elixir performs the critical preprocessing procedures such as bias subtraction and flat-fielding and the reader is directed to the Elixir website* for more details.

The images of each cluster are aligned and median-stacked using the SWarp software package developed by E. Bertin at Terapix. In each image stack for clusters below redshift 0.4 there are 8 r'-band images and 4 g'-band images with single image exposure times of $600s$ and $450s$ respectively. The inverse square reduces the observed flux by a factor of $(1+z)^{-2}$. The exposure times of the highest redshift clusters are correspondingly increased in order to satisfy the lensing signal requirement of observing increasingly faint and more distant galaxies. For this reason image stacks of clusters above a redshift of 0.4 contain 12 r' images and 4 g' images with exposure times of $600s$. The effect of stacking N frames is to improve the signal to noise ratio by a factor of $\sqrt{N}$ and to exclude most of the high energy cosmic rays through the median filtering process. Because the g' stack has less frames (lower N) than the r' stack, it is harder to determine a robust median in each pixel stack. This effect leads to more cosmic rays being being included in the final stacked g image stacks than the r' image stacks. Although some of the cosmic rays are still present in the final stacked images they do not seriously affect our photometry. Only the relatively low energy events survive after median filtering and very few pixels are affected as cosmic rays, being singular events, are not dispersed by the point-spead function.

*http://www.cfht.hawaii.edu/Instruments/Elixir/

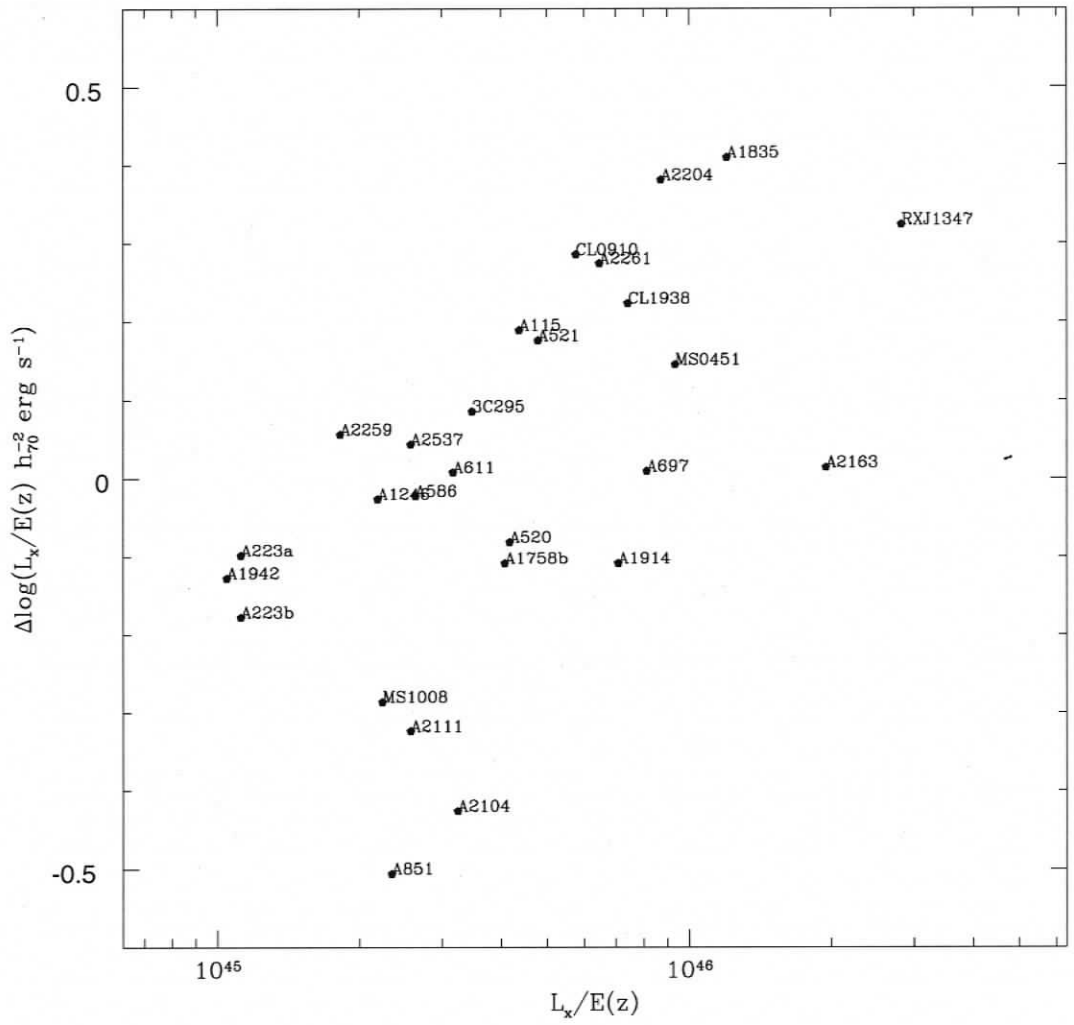

Figure 6.6: $\Delta log(L_x/E(z))$ vs $L_x/E(z)$ for the clusters with X-ray data in the CCCP sample. This correlation is an artifact of the incompleteness of the CCCP cluster sample.

BCGs tend to reach a maximum stellar mass (assuming a constant M/L for BCGs) which does not grow appreciably with an increase in cluster mass. This property of a constant average BCG total magnitude across the range of cluster temperatures and presumably masses implies that BCGs can be as standard candle distance estimators

given a large enough sample. The lack of correlation with temperature also implies that any trend seen in figure 6.4 between $M_{B,tot}$ and L_x is not simply due to increased BCG luminosity for more massive and X-ray luminous clusters but is more likely due to a difference in the structural properties from one cluster to another at a given mass. If it is indeed differences between the ICM structural properties that assist the growth of the BCG stellar component one must be extremely careful to understand and correct for these effects prior to using these galaxies as distance estimators.

6.5 Dependence on BCG/X-ray peak offset

The effects of cooling are most dramatic in the centers of relaxed clusters. From figure 6.4 we can see that BCGs lying close to the center of their host clusters X-ray peak are brighter and more likely to be correlated with the scatter in L_x-T_x. We examine here how BCG absolute B-band magnitude and host cluster $\Delta log(L_x/E(z))$ relate to the projected offset of the BCG from the X-ray peak (R_{offset}) which we use as a measure of the dynamical state of a BCG within its host cluster. In figure 6.7 we show the distributions of BCG total magnitude (corrected to Johnson B) as a function of projected offset. The trend seen in this figure indicates an increase in brightness for BCGs that lie near the peak of the X-ray emission. There are no faint BCGs with small offsets and no bright BCGs with large offsets.

There are multiple possible explanations for the trend seen in figure 6.7. Perhaps this trend is simply the result of the dependence of dynamical friction on satellite mass ($f_d \propto m_{sat}$). The resulting relaxation times are shorter for more massive systems and if we assume a constant density for the halo and identical initial velocities of the satellites, it is easy to show that $\frac{t_{relax,1}}{t_{relax,2}} \propto \frac{m_{sat,2}}{m_{sat,1}}$. Thus more massive/brighter BCGs would sink to the center of the potential faster than less massive BCGs and the corresponding probability of finding a BCG with a small offset increases with

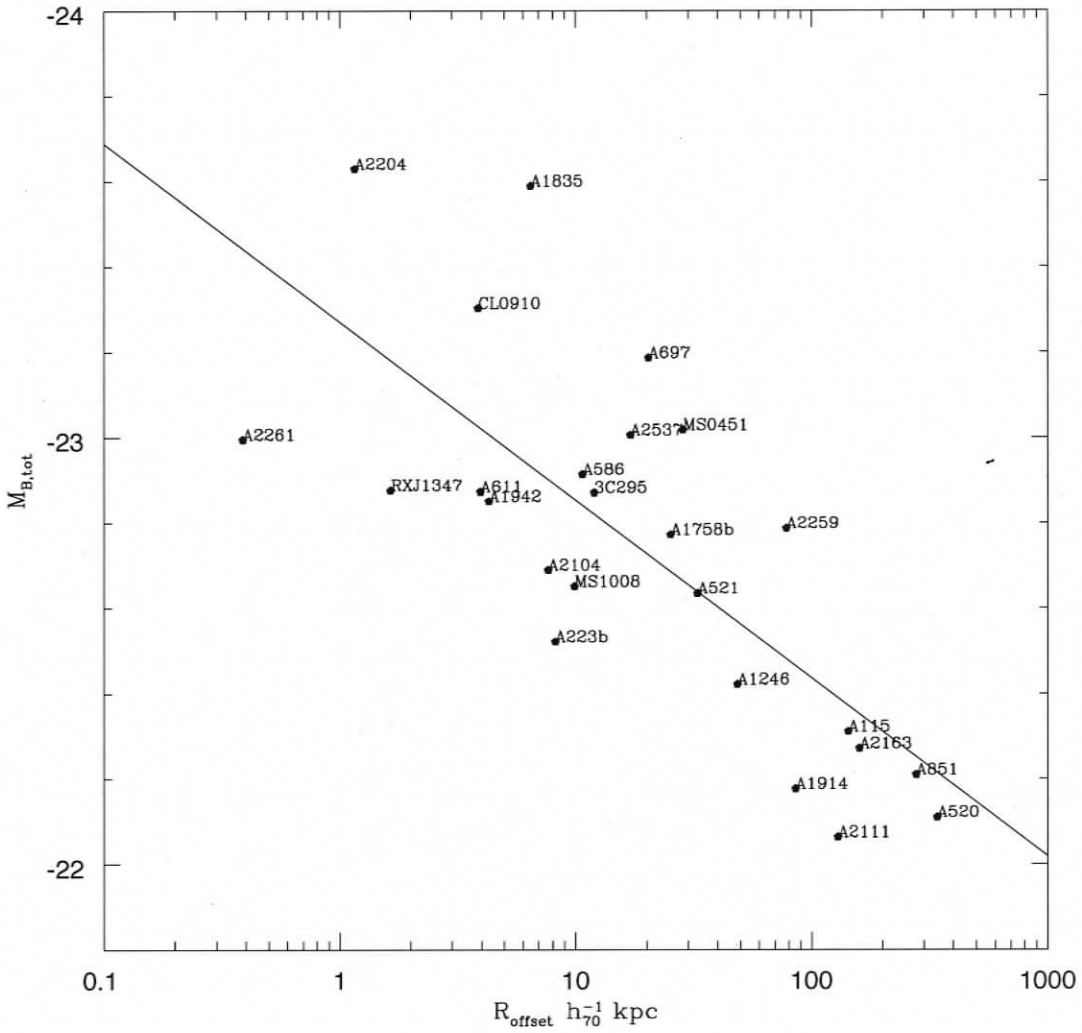

Figure 6.7: BCG $M_{B,tot}$ vs. BCG/X-ray offset. The solid line corresponds to the least-squares fit to the data.

BCG mass. Another explanation for the behavior seen in figure 6.7 is star formation associated with cooling of the ICM. This star formation would need to be concentrated near the X-ray peak. Those BCGs which lie at large offsets would not benefit from this growth mechanism and as a result they would appear much fainter than their small offset equivalents. The observed range in BCG total magnitude across

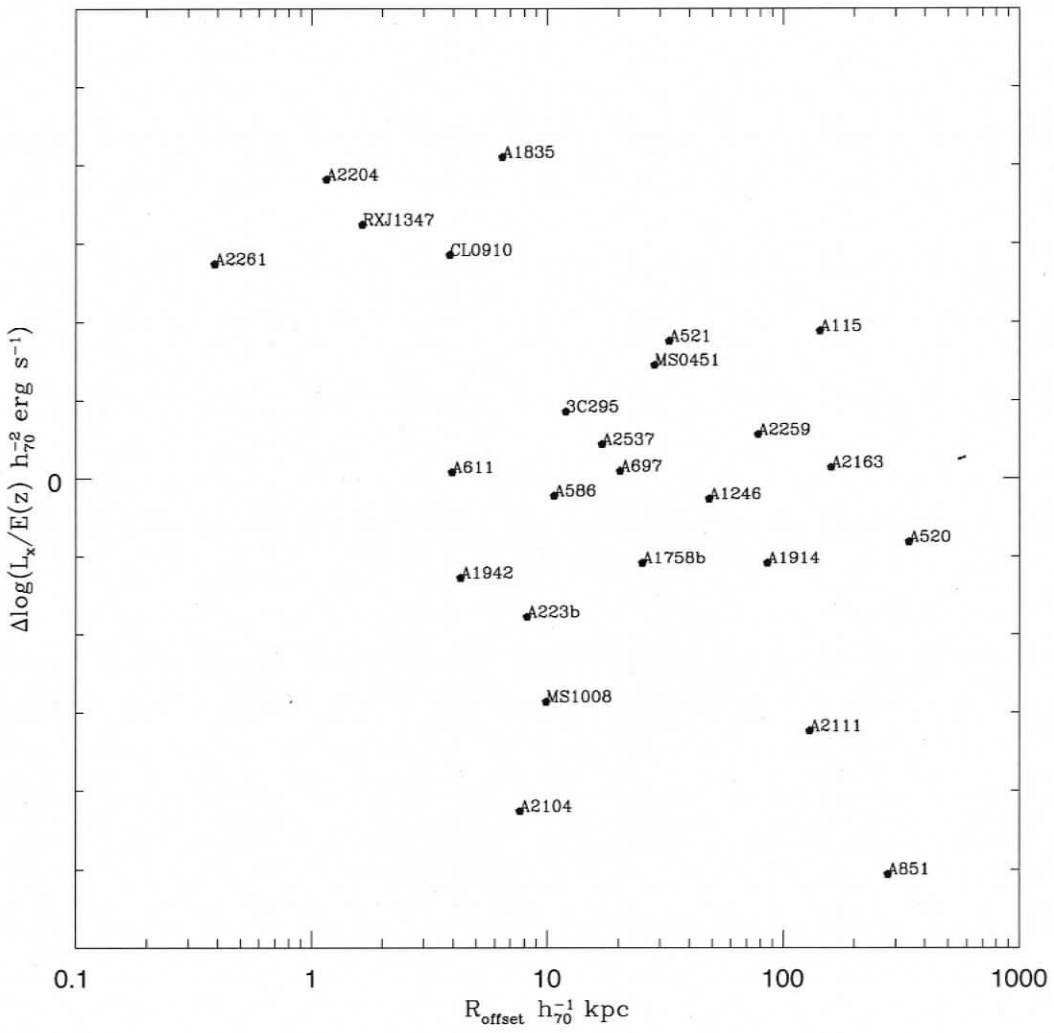

Figure 6.8: $\Delta log(L_x/E(Z))$ vs. BCG/X-ray offset.

the range in offset is 1.6 magnitudes which corresponds to a 56.25% increase in mass (assuming a constant M/L_B for BCGs). For a BCG with an initial stellar mass of $10^{12} M_\odot$ we would therefore require a constant star formation rate of 562.5 $M_\odot/yr$ maintained over 1 Gyr or equivalently 41.1 $M_\odot/yr$ maintained over a hubble time in order to account for the difference in stellar masses. This is an extraordinarily large amount of star formation even when compared to the most extreme cases such

as Abell 1835 which has an estimated star formation rate of 100-200 $M_{\odot}/yr$. In addition, it is unlikely that these high star formation rates are maintained over the long periods needed to explain the observed range in BCG luminosity by this mechanism alone. Merging could also contribute to the observed trend as a BCG with a small offset orbits deep within the densest regions of the cluster where the high merger rate within this environment would allow the BCG to grow at a much faster rate than a BCG with a large offset that lies in a region of lower density/merger rate.

In figure 6.8 we show the dependance of cluster $\Delta log(L_x/E(z))$ on the projected offset R_{offset} between the BCG and the peak of the X-ray emission. The most interesting feature here is the fact that the systems with the highest values of $\Delta log(L_x/E(z))$ are all clustered at small R_{offset}. These systems are also the ones that contain blue core/starforming BCGs (Abell 1835, Abell 2204, CL0910+41 & RXJ1347.5-1145). Abell 2261 however, sits at small R_{offset} with a large value of $\Delta log(L_x/E(z))$ yet does not have a blue core in its BCG's color profile (see figure 5.7). Although this may seem somewhat strange, we do note that there is a decrease in central intensity below what is expected from an $R^{1/4}$ model in the BCG surface brightness for this cluster (see figure 5.3). A possible explanation for this feature is that the cold gas/dust building up in the center of this cluster is causing self-absorbtion of the galaxy light. Work by Bonamente et al. (2006) shows that A2261 has a central cooling time $t_{cool} < 0.5t_{hubble}$ and a central temperature gradient indicating that it has an actively cooling core. From analysis of sub-mm images taken with SCUBA on JCMT, Chapman et al. (2002) find a significant amount of dust ($3.5h_{70}^{-2}M\odot$) associated with the BCG in A2261. The existence of a system such as A2261, where large amounts of cold gas remains unconverted into stars, is consistent with a scenario in which blue cores are the result of a merger-induced burst of star formation following the replenishment of the cold gas reservoir of the BCG.

In this section we have established that faint BCGs are only found at large projected X-ray offsets while all bright BCGs are found to have small projected X-ray offsets. This property of galaxy clusters is likely established by a combination of a stronger effect of dynamical friction for more massive BCGs as well as an increase in the amount of star formation from ICM cooling for BCGs with small X-ray offsets. There is also some evidence for clusters with high values of $\Delta log(L_x/E(z))$ to have small X-ray offsets. Cooling takes baryons from the outer regions of the cluster and moves them inward, steepening the density profile. A change to the density profile results in a change in the dynamical friction force felt by the galaxies. If the cool-core systems are more effective at sinking their galaxies to the center of their potential wells, then their BCGs will grow faster via the effects of cooling and increased merger rates in the high-density cluster cores. The effect of the host cluster environment on the growth of BCGs is evident and we propose a few mechanisms as possible ways of explaining the observed trends between the BCG optical properties and those of their host cluster X-ray emission. Although we can observe their cumulative effect, the relative importance of each of these BCG growth mechanisms is still in question. Realistic numerical simulations that incorporate the effects of collisional and non-collisional processes along with their influence and dependence upon the gravitational potential would be an excellent way to investigate these processes in greater detail.

Chapter 7 | *Conclusions*

In this work we examine the Brightest Cluster Galaxies in a sub-sample of galaxy cluster belonging to the Canadian Cluster Comparison Project. These clusters are primarily X-ray selected and represent the extreme mass/temperature end of the cluster mass/temperature function. The full sample spans the entire range of scatter in the observed cluster scaling relations L_x-T_x and M_x-T_x making it an ideal sample for probing the various processes that create this scatter. Clusters in the CCCP sample all have $T_x \geq 5\ keV$ and lie in a redshift range $0.15 \lesssim z \lesssim 0.55$. We fit simple, circularly symmetric, psf-convolved, $r^{1/4}$ models to the surface brightness profiles to the BCG surface brightness profiles. We examine in correlations between total magnitude, effective radius, effective surface brightness, color, redshift as well as the host cluster X-ray temperature, luminosity, deviation from the mean L_x-T_x relation and BCG/X-ray peak offset. The following conclusions highlight the most important results of this study:

• BCGs are reasonably well fit by a simple $r^{1/4}$ surface brightness model. There are two fairly common features that cause deviation from this simple model. The more common feature of the two is the cD envelope/ICL profile which is seen as an excess in surface brightness at large radius. The cD envelope/ICL profile has been incorporated in the BCG surface brightness model in previous work by adding a second $r^{1/4}$ component (Gonzalez et al. 2005) although we do not attempt to do so here. The second type of deviation from an $r^{1/4}$ model that we observe in this study occurs at small radius and can appears as an excess or deficiency from an $r^{1/4}$ model. This feature is more pronounced in g' than r' when it appears as a surface

brightness excess.

• Several of BCGs in our sample have abnormally blue centers. These objects tend to have color profiles that become bluer towards the BCG center. The blue regions in the cores of these BCGs are in all cases several time the fwhm of the psf; indicating that they are not due to the presence of a point source. These regions are responsible for some of the deviations from pure $r^{1/4}$ surface brightness models mentioned above. We interpret these regions as young stellar populations that have recently formed in these systems. The star-forming regions in these systems are bright enough in g' to cause a significant displacement of their BCGs from the host cluster's red sequence (up to $\sim$ 1 magnitude in the most extreme case). This displacement would cause these blue-core BCGs to be rejected in Luminous Red Galaxy (LRG) surveys if the selection is based on red-sequence membership criterion.

• The BCGs in the CCCP sample display a wide range in effective radius r_e ($25 \lesssim r_e \lesssim 200\ h^{-1}kpc$) and effective V-band surface brightness $\mu_{e,V}$ ($21 \lesssim \mu_{e,V} \lesssim 27$ mag). This observed range in optical properties reflects the wide range of formation histories and physical processes that are important in building the stellar content and shaping its distribution in these rare systems. By fitting the effective surface brightness evolution and assuming homology, we determine a mass to light ratio evolution in BCGs of: $\Delta logM/L_V = -0.69\Delta z$. This is a slightly steeper redshift dependence than that obtained by van Dokkum & Franx (1998) for cluster ellipticals. Correcting for the effects of this evolution we obtain a Kormendy relation which matches that of the local elliptical galaxy population (Kormendy 1977).

• The outer color profiles of the BCGs in the CCCP samples are qualitatively consistent with age/metallicity gradients. An age gradient indicates an inside-

out formation history. In such a scenario the core of the galaxy is formed first and the outer envelope is accreted at later times by canabalizing younger satellite galaxies. If the data are interpreted as a metallicity gradient the implication is that the level of chemical enrichment increases towards the centers BCGs. We cannot distinguish between these two scenarios with the current observations. Future work is planned to obtain spectra of the BCGs with which we would be able to break this age/metallicity degeneracy and comment further on their formation histories.

• The integrated color profiles of the BCGs in the CCCP sample display a range in (g'-r'). Most of the BCGs have rest-frame colors of $0.4 \leq (g' - r') \leq 0.7$ but the blue-core BCGs have much bluer colors. The most extreme system CL0910+41 has a (g'-r') color of about -0.3. The assumption of a purely elliptical galaxy spectrum for these blue objects is not valid.

• The majority of the BCGs have nearly identical values of the logarithmic color gradient within the inner $15h_{70}^{-1}kpc$ of $d(g' - r')/dlog(r) \sim -0.15$. The BCGs with blue cores, meaning those with positive values of $d(g' - r')/dlog(r)$, only occur in clusters that lie on the high luminosity side of the L_x-T_x relation. These systems display a range in their inner color gradients of $0.1 \leq$d(g'-r')/dlog(r)≤ 1.4 reflecting a variety of star-formation properties.

• BCG total luminosity is observed to correlate with cluster L_x as well as the scatter in the L_x-T_x relation measured by $\Delta log(L_x/E(z))$. The correlation with $\Delta log(L_x/E(z))$ is more apparent for those systems in which the BCG lies within a 20 $h_{70}^{-1}kpc$ projected offset from the X-ray emission peak. This seems to indicate that cooling plays a significant role in building up the luminosity/stellar mass of the BCG.

• Within the CCCP sample, a BCG's total luminosity correlates with the projected offset from its host cluster's X-ray peak emission such that BCGs with small

offsets are brighter than BCGs with large offsets. This correlation holds for BCGs in clusters on both sides of the scatter in L_x-T_x.

• The clusters with the highest values of $\Delta log(L_x/E(z))$ all have BCGs which lie at small projected offset from the host X-ray emission peak. These also coincide with the subset of BCGs that have blue cores in all but one case: Abell 2261. Abell 2261's BCG contains a central surface brightness deficit from an $r^{1/4}$ model. It may be that the central regions of the BCG are obscured by dust accreting from the cooling ICM in this case. Spectral followup observations of this region would be able to determine if this is indeed the case.

We have shown that not all BCGs are simple stellar populations. The current quenching model of cluster galaxy formation cannot explain the blue core BCG systems that are observed in the CCCP sample. Some BCGs continue to form stars long after their less luminous red-sequence counterparts have exhausted their respective cold gas supplies. The clusters which contain blue-core BCGs lie on the high luminosity side of the L_x-T_x relation which tends to be dominated by systems that are efficiently cooling. Blue-core BCGs also all lie at small projected offset from the peaks of their host cluster X-ray emission. This suggests that the source of the cold gas replenishment in blue-core BCGs is external and probably supplied by the cooling ICM.

The existence of a general trend of increased BCG luminosity with decreasing projected offset is very interesting. There are various physical processes that would drive systems in this direction. We have shown that star formation in BCGs is ongoing and dependent upon the distance of the BCG from the X-ray peak. The high star formation rates required to explain the full range in BCG magnitude, as well as the fact that this trend is also observed for cluster which do not have extreme values of $\Delta log(L_x/E(z))$, implies that there are other factors that help to create this correlation. Mass segregation through the m^2 dependence of the

dynamical friction force f_d would cause the brighter/more massive BCGs to sink to the centers of their host clusters faster than fainter/less massive BCGs. The presence of increased galaxy density within the inner regions of clusters would also tend to reinforce this correlation through an increase in merger activity for any BCG that passes through the cluster central regions. It is likely that all of these processes act together to build up the stellar mass in BCGs. The details of structure within this correlation and the importance of various mechanisms in establishing it are of great interest and the subject of future work.

BCGs are not standard candles. They can have highly extended profiles that contain multiple physical components that are difficult to separate photometrically. Although they can be useful tools for describing the general properties of these systems, simple, circularly symmetric, single component $r^{1/4}$ models are not fully adequate to describe the range of variation in the observed features of BCG surface brightness profiles. The total luminosity of BCGs is dependent on various cluster X-ray properties. These dependencies must be fully understood and corrected for before using BCGs as distance estimators in cosmological or large-scale structure studies.

Bibliography

The following abbreviations are used in this bibliography:

MNRAS: Monthly Notices of the Royal Astronomical Society

ApJ: The Astrophysical Journal

ApJ: The Astrophysical Journal Letters

ApJSS: The Astrophysical Journal Supplement Series

AJ: The Astronomical Journal

A&A: Astronomy and Astrophysics

Ap&SS: Astrophysics and Space Science

ARA&A: Annual Reviews of Astronomy and Astrophysics

PASP: Proceedings from the Astronomical Society of the Pacific

PhST: Physica Scripta volume T

Balogh M. L., Babul A., Voit G. M., McCarthy I. G., Jones L., Geraint L., Ebeling H. **2006**, MNRAS, 336, 624B

Bertin E. & Arnouts S **1996** A&AS, 117, 393

Bernstein J. P. & Bhavsar S. P. **2001** MNRAS, 322, 625B

Binney J. & Tremaine S. **1987**, *Galactic Dynamics*, Princeton University Press

Binney J. & Merrifield M. **1998**, *Galactic Astronomy*, Princeton University Press

Bonamente M., Joy M., LaRoque S., Carlstrom J., Reese E. & Dawson K. **2005** AAS, 20717018B

Bower R. G., Benson A. J., Malbon R., Helly J. C., Frenk C. S., Baugh C. M., Cole S., Lacey C. G. **2006** MNRAS, 370, 645B

Bruzual A. & Charlot S. **1993** ApJ, 405, 538

Chapman S. C., Scott D., Borys C. & Fahlman G. G. **2002** MNRAS, 330, 92C

Coleman G. D., Wu C. C. & Weedman D. W. **1980** ApJS, 43, 393

Cooper M. C., Newman J. A., Croton D. J., Weiner B. J., Willmer C. N. A., Gerke B. F., Madgwick D. S, Faber S. M., Davis M., Coil A. L., Finkbeiner D. P., Guhathakurta P., Koo D. C. **2006** MNRAS, 370, 198C

Crawford C. S., Allen S. W., Ebeling H., Edge A. C., Fabian A. C. **1999** MNRAS, 306, 857C

Cimatti A., Daddi E., Renzini A. **2006** ApJ 638, 72K

David L. P., Slyz A., Jones C., Forman W., Vrtilek S. D. & Arnaud K. A. **1993** ApJ, 412, 479D

Djorgovski S., Davis M. **1987** ApJ, 313, 59D

Dressler A., Lynden-Bell D., Burstein D., Faber S. M., Terlevich R., Wegner G. **1987** ApJ, 313, 42D

Edge A. C. & Stewart G. C. **1991** MNRAS, 252, 414E

Edge A. C. & Stewart G. C. **1991** MNRAS, 252, 428E

Eggen O. J., Lynden-Bell D. & Sandage A. R. **1962** ApJ, 136, 748E

Faber S. M., Tremaine S., Ajhar E. A., Byun Y. I., Dressler A., Gebhardt K., Grillmair C., Kormendy J., Lauer T. R., Richstone D. **1997** AJ, 114, 1771F

Feldmeier J. J., Mihos J. C., Morrison H. L., Rodney S. A., Harding P. **2002** ApJ, 575, 779F

Feldmeier J., Mihos C., Morrison H., Harding P. **2004** AAS, 20514601F

Feldmeier J., Ciadullo R., Jacoby G. H., Durrell P. R. **2004** ApJ, 615, 196F

Feldmeier J., Mihos C., Morrison H. L., Harding P., Kaib N., Dubinski J. **2004** ApJ, 609, 617F

Ferrarese L., Silbermann N., Mould J. R., Stetson P. B., Saha A., Freedman W. L., Kennicutt R. C. **2000** PASP, 112, 177F

Fukazawa Y. **1997** PhD Thesis

Gladders M. D., Lopez-Cruz O., Yee H. K. C. & Kodama T. **1998** ApJ, 501, 571G

Gladders M. D., Yee H. H. C. **2005** ApJS, 157, 1G

Gonzalez A. H., Zabludoff A. I., Zaritsky D. **2005** ApJ, 618, 195G

Goto T. **2005** MNRAS, 359, 1415G

Graham A., W., Driver S. P., Petrosian V., Conselice C. J., Bershady M. A., Crawford S. M., Goto T **2005** AJ, 130, 1535G

Harker J. J., Sciavon R. P., Weiner B. J., Faber S. M. **2006** ApJ, 647L.103H

Harris D. E., Nulsen P. E. J., Ponman T. J., Bautz M., Cameron R. A., David L. P., Donnelly R. H., Forman W. R., Grego L., Hardcastle M. J., Henry J. P., Jones C., Leahy J. P., Markevitch M., Martel A.R., McNamara B. R., Mazzotta P., Tucker W., Virani S. N. & Vrtilek J. **2000** ApJ, 530L, 81H

Hogg D. W. astro-ph/9905116

Horner D. **2001** PhD Thesis

Juneau S., Glazebrook K., Crampton D., McCarthy P. J., Savaglio S., Abraham R., Carlberg R. G., Chen H. W., Le Borgne D., Marzke R. O., Roth K., Jorgensen I., Hook I., Murowinski R. **2005** ApJ, 619L, 135J

Kaiser N. **1986** MNRAS, 222, 323K

Kay S. T., da Silva A. C., Aghanim N., Blanchard A., Liddle A., Puget J. L., Sadat R., Thomas P. A. **2007** MNRAS.tmp, 234K

Kormendy J., Bender R. **1996** ApJ, 464L, 119K

Kormendy J. **1977** ApJ, 218, 333K

Krick J. E., Bernstein R. A. **2005** AAS, 20717714K

Lin Y. T., Mohr J. **2004** ApJ, 617, 879L

Madau M., Ferguson H. C., Dickinson M. E., Giavalisco M., Steidel C. C. & Fruchter A. **1996** MNRAS, 283, 1388

Martin E., GALEX Science Team **2005** AAS, 207, 5201M

Moffat A. F. J. **1969** A&A, 3, 455M

Mushotzky R. F. **1984** PhST, 7, 157M

Navarro J. F., Frenk C. S. & White S. D. M. **1995** MNRAS, 275, 720N

Navarro J. F., Frenk C. S. & White S. D. M. **1996** ApJ, 462, 563N

Patel P., Maddox S., Pearce F. R., Aragon-Salamanca A., Conway E. **2006** MNRAS, 370, 851P

Poole G. B., Fardal M. A., Babul A., McCarthy I. G., Quinn T. & Wadsley J. **2006** MNRAS, 373, 881P

Poole G. B., Babul A., McCarthy I. G., Fardal M. A., Bildfell C. J., Quinn T. & Mahdavi A. **2007** astro-ph, 1586P

Postman M., Lauer T. **1995** ApJ, 440, 28p

Press W. H. & Schechter P. **1974** ApJ, 187, 425

Randall S. W., Sarazin C. L. & Ricker P. M. **2002** AAS, 201, 6706R

Ravindranath S., Ho L. C., Filippenko A. V. **2001** AAS, 198, 9302R

Ritchie B. W. & Thomas P. A. **2002**, MNRAS, 239, 675R

Rowley D. R., Thomas P. A. & Kay S. T. **2004**, MNRAS, 352, 508R

Schindler S., Guzzo L., Ebeling H., Boehringer H., Chincarini G., Collings C. A., de Grandi S., Neumann D. M., Briel U. G., Shaver P., Vettolani G. **1995** A&A, 299L, 9S

Searle L. & Zinn R.**1978** ApJ, 225, 334

Simard L. **1998** ASPC, 145, 108S

Simard L., Willmer C. N. A., Vogt N. P., Sarajedini V. L., Phillips A. C., Weiner B. J., Koo D. C., Im M., Illingworth G. D. & Faber S. M. **2002** ApJS, 142, 1

Stetson P. B., Davis L. E., Crabtree D. R. **1990** ASPC, 8, 289S

Thimm G. J., Roeser H. J., Hippelein H. & Meisenheimer K. **1994** A&A, 285, 785T

Trujillo I., Aguerri J. A. L., Cepa J. & Gutiérrez C. M. **2001**, MNRAS 328, 977

Von Der Linden A., Best P. N., Kauffmann G. & White S. D. **2006**, AAS, 20918305V

Wilman R. J., Edge A. C., Swinbank A. M. **2006** MNRAS, 371, 93W

Zaritsky D., Gonzalez A. H., Zabludoff A. I. **2006** ApJ, 638, 725Z

Zibetti S., White S. D. M., Schneider D. P., Brinkmann J. **2005** MNRAS, 258, 949Z

Zirm A. W., Overzier R. A., Miley G. K., Blakeslee J. P., Clampin M., De Breuck C., Demarco R., Ford H. C., Hartig G. F., Homeier N., Illingworth G. D., Martel A. R., Rttgering H. J. A., Venemans B., Ardila D. R., Bartko F., Bentez N., Bouwens R. J., Bradley L. D., Broadhurst T. J., Brown R. A., Burrows C. J., Cheng E. S., Cross N. J. G., Feldman P. D., Franx M., Golimowski D. A., Goto T., Gronwall C., Holden B., Infante L., Kimble R. A., Krist J. E., Lesser M. P., Mei S., Menanteau F., Meurer G. R., Motta V., Postman M., Rosati P., Sirianni M., Sparks W. B., Tran H. D., Tsvetanov Z. I., White R. L., Zheng W. **2005** ApJ, 630, 68Z

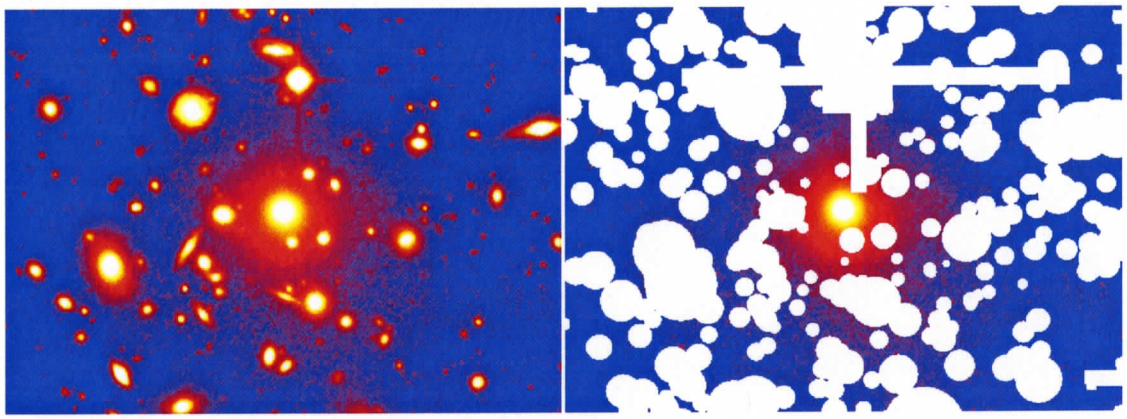

Figure 2.1: Image and masked image of ABELL 223b. The scale of each image shown is 114" × 82".

2.3 Background Subtraction

We wish to measure BCG surface brightness at a signal level below the rms variation in the image background (σ_{bgd}). At this low surface brightness level error in the background and large-scale flat-field are the dominant sources of systematics. It is therefore critical to determine the background map to a high degree of accuracy. The background maps in this case were determined during the stacking procedure using the SWarp software package (see section 2.2). The image is divided into a mesh of subsections and a σ-clipped median background level is determined in each image subsection. The spatial variation in the background is then determined across the entire image by fitting a simple function (eg. low order polynomial) to the set of medians in each region. Flux from extended cluster objects, as well as bright stars can mimic background variation. We take care to exclude from the fit the mesh sections that are near the cluster centre. Inclusion of some of the diffuse cluster light in the background map can lead to loss of the signal of scientific interest after background subtraction in the final stacked image. This source of systematic error is particularly problematic when attempting to measure the contribution to the cluster optical surface brightness from faint Intra-Cluster Stars (ICS). The effects

of background subtraction on measured BCG surface brightness level and BCG surface brightness fit parameters are discussed in section 3.3 and section 4.2 .

2.4 Source Detection

In order to accurately measure surface brightnesses of galaxies on the full range of scales accessible with our data we take great care when identifying the image pixels with their respective sources. This identification is done in an automated way and therefore the parameters that control the automation must be well chosen to minimize the effects of contaminating systematics. One of the main sources of contamination is the presence of unresolved or low surface brightness galaxies. These faint galaxies may be real cluster members or they may simply appear to be cluster members due to projection effects. Failure to identify these small, faint galaxies contributes to an excess in the measured surface brightness (μ) of the BCG. These undetected sources are particularly problematic in the the radial regime where the intrinsic surface brightness of the BCG is comparable to the detection limit. Faint galaxies can be very difficult to detect in the crowded fields common of galaxy cluster environments. Detection is especially difficult when they lie on the extended wings of nearby bright galaxies or within the more central regions of bright galaxies. The wings raise the effective background level used by the detection algorithm thereby forcing the effective detection limit to brighter levels. This problem is very similar to the notorious problem of conducting detailed photometry in crowded stellar fields and is well documented by other authors (Stetson et al. 1990; Ferrarese et al. 2000).

The automated source detection and extraction routine SExtractor (Bertin & Arnouts 1996) is used to conduct the initial source identification and mask generation. As previously mentioned, it is critical that we choose the extraction parameters carefully to ensure a minimum amount of contamination by undetected sources and

blended sources. We base our choice in extraction parameters on those used by Simard et al. 2002. They measure and fit detailed surface brightness profiles to galaxies spanning a wide variety of Hubble types. We find their parameters to be a good starting point. However, because we are focusing on galaxies at the centers of massive clusters, where crowding becomes a serious issue, we must decrease the deblending threshold parameter (DEBLEND_MINCONT) to 0.00001 in order to maximize the detection of galaxies of a large variety in magnitude and morphological type within these crowded fields (see Bertin & Arnouts 1996 for details).

We use SExtractor to generate a segmentation image which becomes the basis of our mask for measuring surface brightness profiles and calculating background intensities around individual objects. The SExtractor masking routine assigns an integer value to each pixel in the image. Each pixel containing flux from a detected object is assigned a value corresponding to that particular object and each background pixel is assigned the special value of zero. The final output is a segmentation image in which every pixel is either identified with a detected object or identified with the background. This initial mask is then improved by a series of extensions described in section 2.5 in order to account for a variety of systematic effects that lead to inadequacies in the segmentation image generation.

SExtractor is a powerful tool for automated detection and analysis of astronomical sources and works very well in the case of a pristine image, by which we mean an image containing only source flux and noise with no defects. Unfortunately the image stacks often show the typical signatures of detector limitations (bad pixels, saturations, charge-transfer errors, etc.). In addition the secondary support structure and corrector lens can also manifest undesirable affects on the data (rings, crosses, etc.). To complicate matters further, the stacking process can create unusual noise patterns unique to each image. It is very difficult for SExtractor to properly deal with these effects in a fully automated way. For these reasons, we find it necessary to carefully inspect each image stack by eye and make any neces-

sary additions to the image mask by hand. The following section describes in detail what was masked by hand from each image and where possible errors and masking incompleteness may have occurred. An example of one of our final masked images can be seen in figure 2.1.

2.5 Image Masking

The Megacam detector contains 36 charge-coupled devices (CCDs) and covers a square degree on the sky. The images from each chip must be patched together into a mosaic. Images from successive exposures are slightly dithered to ensure that any pixels-to-pixel variation in the detector sensitivity does not become a major source of systematics. In effect, this measure helps to minimize the impact of the large-scale flatfield uncertainty on our photometric results. After astrometric alignment, successive exposures are stacked together and all chips are combined to produce the mosaic. Because the CCDs on the detector do not sit flush against one another there are small gaps between chips. There are inevitably some small strips of the sky that do not get imaged due to the presence of these gaps. Small scale dithering helps to deal with the missing sky coverage but there are still sections of the image that contain fewer pixels in a stack than the total number of exposures. The $1/\sqrt{n}$ dependence of signal-to-noise for a stack containing n pixels leads to abrupt changes in signal-to-noise properties at the chip edges. For the detailed surface brightness fitting in this study, it is undesirable to have such sudden changes in noise quality. We therefore mask all strips where this effect is obvious in the final mosaics.

A variety charge transfer defects can occur on read-out or during the exposure itself. These defects often create bad pixels or bad columns of pixels that must also be masked out of the image. We also mask any pixels that have a negative flux greater than 10σ below the background. Saturation effects must also be considered especially when trying to determine the image PSF. All background pixels (ie. not

associated with any object) at greater than 95% of the saturation level are masked out. We select the 95% level to reflect departure from detector linearity.

Exposure times of several hundred seconds are required to observe our targets at the desired depth. For such long exposures, foreground stars contribute a considerable amount of contaminating flux. One of the sources of such contamination is reflected starlight from the corrector lens. This effect creates a "donut" of light that is often skewed in shape and offset from the star's center. The skewness and offset typically depend on telescope pointing direction and the star's location on the detector. This effect is very difficult to model accurately, so we choose to mask out all obviously visible stellar "donuts". This effect is most apparent around bright stars but is also present around fainter stars as well. For saturated stars it is easy to see this effect and mask it out by hand but for unsaturated stars the obvious characteristic signal of this effect is below the variation in the background level σ_{bgd} and it is not possible to mask it out. As a consequence, there is some small contribution of systematic contamination for very faint surface brightness measurements (ie. below the background variation σ_{bgd}) from faint stellar reflections. These faint stellar reflections however do not affect the results presented here.

Another familiar example of stellar contamination is the diffraction pattern of a bright star created by the secondary support structure. This effect creates images of "spikes" that extend from the center of the star along the X and Y axes of the detector. These are easily masked out by hand or by an automated masking routine. We employ both methods in order to be certain that we are free from image contamination.

Most elliptical galaxy surface brightness profiles are well described by a simple modified powerlaw of the form:

$$\mu(r) = \mu_e - \beta[(r/r_e)^{1/4} - 1] \tag{2.1}$$

where $\mu(r)$ is the surface brightness in magnitudes per square arcsecond, r_e is the

effective radius and μ_e is the surface brightness at the effective radius. The shallow $r^{1/4}$ dependence of this profile means that elliptical galaxy surface brightness profiles have very extended wings and often overlap in crowded galaxy clusters. This creates confusion when fitting a single galaxy's profile in a field of bright neighbors. Simple isophotal masking techniques perform poorly around sources with shallow profiles as non-negligible portion of the neighboring galaxies contributes flux to the source that we are interested in fitting. It is especially problematic when trying to determine the large radius behavior of the profile where the BGC flux is very faint and the contaminating wings of nearby galaxies are relatively bright. We have attempted to deal with this problem by fitting Sersic profiles to all of the detected cluster member galaxies and subtracting them from the image prior to fitting the BCG profile. We used the Gim2d software package of L. Simard (Simard 1998) to fit and subtract models for the non-BCG cluster members. We find that due to the high degree of crowding in most of our cluster fields, the uncertainty in the fits and resulting galaxy subtraction does not significantly improve our ability to measure BCG surface brightnesses. This finding is in agreement with similar work by Patel et al. (2006) who encounter the same difficulty with star subtraction techniques. They adopt a pure masking approach (no galaxy/star subtraction) which we also employ here.

Because isophotal masking can lead to major contamination of the BCG signal from neighboring cluster members we choose to mask the crowded region around the BCG by hand. We examine each image carefully and mask any visible sources out to a radius at which they are no longer obviously contributing to BCG contamination. The contrast level of the image is then adjusted slightly and the process is repeated. In this way we iterate out to fainter and fainter surface brightness levels at increasing distance from the BCG centre. We find that this process is superior to isophotal masking as it reduces mask incompleteness and leads to a robust determination of BCG surface brightness.

Finally, as an added precaution to reduce some of the systematic errors and obtain more reliable surface brightness fits, we choose to extend each masked region by a fixed size on all sides. This process is performed on the combined SExtractor + hand-made masks. Each group of masked pixels grows by $n_{pix} = 5$ which represents 0.93". We find that this helps to reduce the amount of contamination from nearby, bright galactic and stellar sources when fitting the large radius surface brightness profile of the BCG.

2.6 Object Classification and Cataloging

In order to accurately determine the PSF, a list of candidate stars must be compiled for each image. We sub-divide the SExtractor catalog into a catalog of stars and a catalog of galaxies. This task can be done to first order using solely the SExtractor stellarity index i_s of Bertin & Arnouts 1996. We experiment with various different threshold values for stellarity $0.85 \leq i_s \leq 0.99$, but independent of a chosen threshold, there is always a significant level of misidentification. Because of this we choose to select stars using a different method. By plotting the magnitudes versus half-light radii of all the detected objects, it is possible to identify a region that is only occupied by sufficiently bright, unsaturated stars (figure 2.2).

Because stars are point sources, the flux distribution from a star is determined only by the PSF. Any galaxy of the same magnitude will have a larger size owing to the fact that galaxies are extended objects on the sky. The situation becomes slightly more complicated near the faint end where low surface brightness galaxies in the image begin to mimic point sources. There are also notable problems at the very bright end where objects become saturated. As an object becomes saturated it grows in half-light radius without much increase in total flux. Such stars need to be avoided when trying to determine the PSF. Despite these difficulties, we are able to select a region in $m - r_{1/2}$ space that contains only unsaturated stars and create

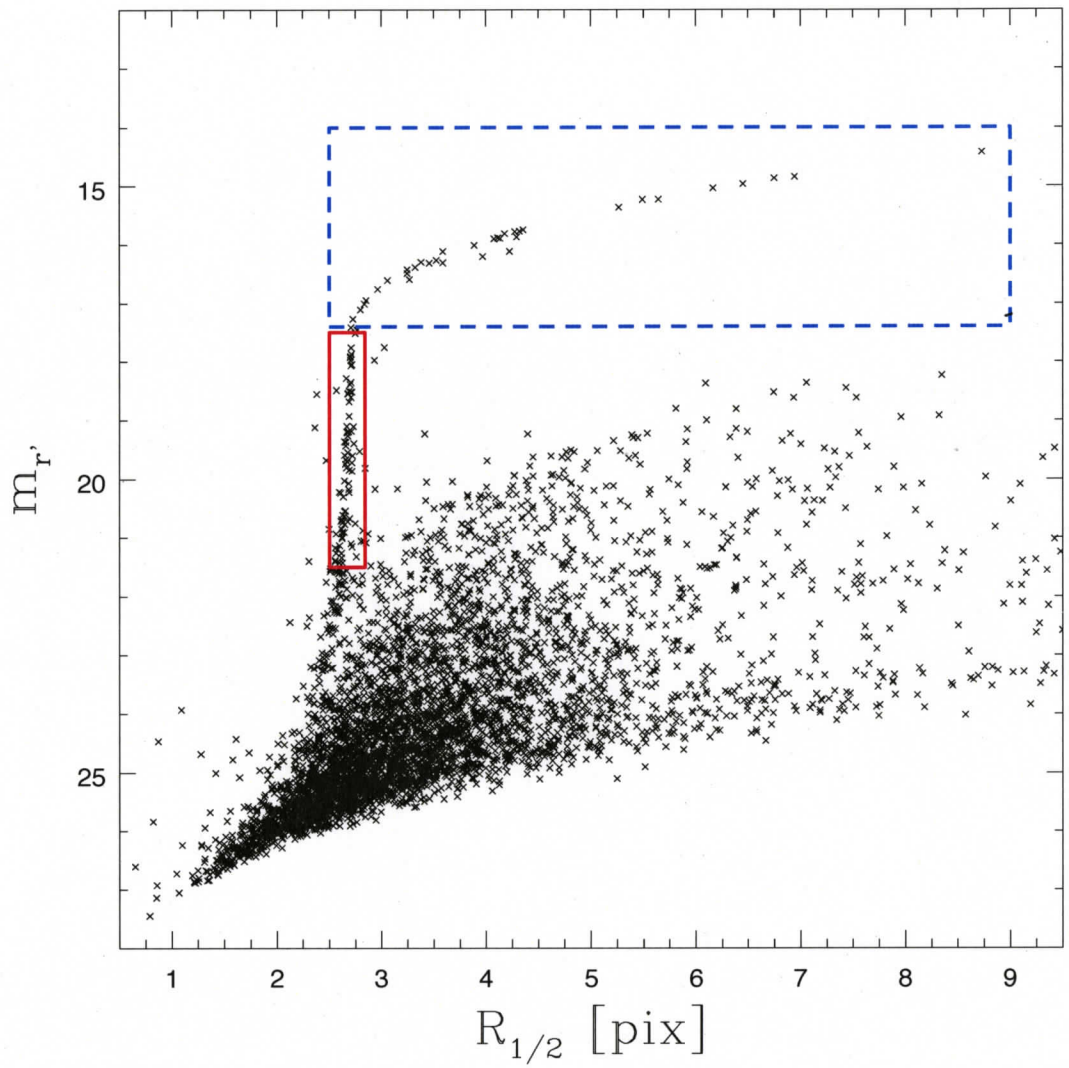

Figure 2.2: Magnitude-size relation for all detected objects in the r' image of ABELL 611. The solid red outline shows the selected unsaturated stars. The dashed blue outline shows the selected saturated stars.

a list of candidates from which to determine the PSF. We call objects selected by this means the unsaturated star catalog.

Similar to the previous selection, we can also select saturated stars based on their location in the $m - r_{1/2}$ plane. The thin column of points that make up the unsaturated star catalog begins to turn over towards large half light radii at the magnitude corresponding to the departure from linearity of the detector. These saturated objects are clearly separated from the galactic sources which occupy a fainter magnitude region of the graph (see figure 2.2). These stars make up the saturated star catalog.

Chapter 3 | *Analysis*

3.1 Surface Brightness Measurement

During the stacking process the pixel counts are combined and divided by the exposure time to create a stacked pixel value proportional to flux. We calculate surface brightness from the images by converting scaled value per pixel into magnitudes per square arcsecond. The analysis is conducted using a software package called ICICLE which was built using the FITSIO libraries in fortran. This software package is the main tool used for conducting surface brightness measurement and BCG model fitting.

Because we measure the surface brightness profile using a modified logarithmic binning we can resolve the variation on multiple scales. We modify the logarithmic binning by using a linear scale at small radius. The purpose of using linear bins on small scales is to suppress correlated noise and to prevent too much weight from going to the data at small radii when fitting model profiles to the surface brightness distribution (discussed further in BCG fitting section).

Because an individual pixel may land on the border between adjacent radial bins, it is necessary to resample and interpolate the data on small radial scales in order to smooth out the effects of discrete pixelation. Each pixel at small radii ($r_{pix} \lesssim 10pix$) is resampled by a factor of $\sim 50 \times 50$. The effect of which is that a given pixel is divided into many subpixels. The flux assigned to each subpixel is determined with a bilinear interpolation scheme. This procedure is robust except in the very central pixel where the intrinsic profile peaks. Circular apertures are

then placed over the image and the mean pixel value is determined in each annular bin. Statistical errors are assumed to be caused by poisson noise. Only pixels that are unambiguously identified with the source of interest or pixels identified as background pixels are allowed to contribute to the object count rate within an aperture bin. Once the count rate per pixel is measured, we convert to a surface brightness using the following relation:

$$\mu(r) = -2.5 \log \frac{\overline{v}(r)}{S_{pix}^2} + m_0 \tag{3.1}$$

where $\mu(r)$ is the annular surface brightness in $mag\ arcsec^{-2}$, $\overline{v}(r)$ is the mean pixel value, S_{pix} is the pixel scale in $arcsec\ pix^{-1}$ and m_0 is the detector zero point magnitude. Radii representative of each bin are chosen to be the area-weighted mean of bin minimum radius and bin maximum radius:

$$r = \frac{2}{3} \frac{r_{max}^3 - r_{min}^3}{r_{max}^2 - r_{min}^2} \tag{3.2}$$

where r_{min} and r_{max} are the minimum and maximum radius of the bin respectively.

3.2 PSF Determination

In order to fit a model surface brightness distribution to our BCG data, we must first know the point spread function (PSF). The PSF is affected by many different factors. It varies as a function of observing conditions telescope pointing and location of the image on the detector. We experiment with a selection of PSFs and find that for our data the PSF is best fit with a moffat profile (Moffat 1969) of the form:

$$I(r) = I_0[1 + (r/\alpha)^2]^{-\beta} \tag{3.3}$$

where I_0 is the central intensity, α is a width parameter and β is a parameter describing the large radius behavior. The assumed moffat profile for the PSF generates excellent fits to the stellar profiles in our data as seen in figure 3.1. The data

are shown as dotted lines while the model fits are shown as solid lines. Colors in figure 3.1 denote filter type, with r' in red and g' in blue. We show the PSFs of four clusters that have been chosen arbitrarily from our sample. The fits are of similar quality for all cluster images. The superiority of the moffat profile for our data is attributed to the large PSF wings seen in our data. The flexible β parameter in the moffat profile allows for a slow decline in flux at large radii that gaussian profiles are not able to reproduce.

The parameters that best describe the PSF often vary slightly across the image. In selecting a PSF candidate we choose a star from our unsaturated star catalog that is the close to the BCG center but outside $r = 35$". Stars that are too close to the cluster center are bad PSF candidates because the extended BCG light can masquerade as broad PSF wings. We assume that the resulting selection is representative of the best PSF to use for fitting the BCG profile. We first measure the surface brightness in $\overline{v}\ pix^{-2}$ as a function of radius as described in section 3.1 . We then renormalize the total counts to unity by integrating out to the truncation radius $r_t = 28$ pixels or about 5.18". Beyond this radius the contribution to the total counts from the broad wing component is negligible. The renormalization procedure is carried out mainly to conserve total flux when applying the PSF to a model convolution, but it has the added benefit of reducing the moffat parameter space required to search. A fit to the measured data are then obtained by minimizing χ^2 using a downhill simplex minimization routine with χ^2 computed as follows:

$$\chi^2 = \frac{1}{N}\sum \frac{(I(r) - I_m(I_0, \alpha, \beta))^2}{\sigma^2} \tag{3.4}$$

where N is the number of data points, $I(r)$ is the measured surface brightness and I_m is the moffat profile that is varied during minimization. The moffat parameters are I_0 a normalization, α a measure of the width and β which characterizes the large radius falloff. After fitting the profile is then renormalized again to unity to correct for any difference between the integrated flux of the model and that of the

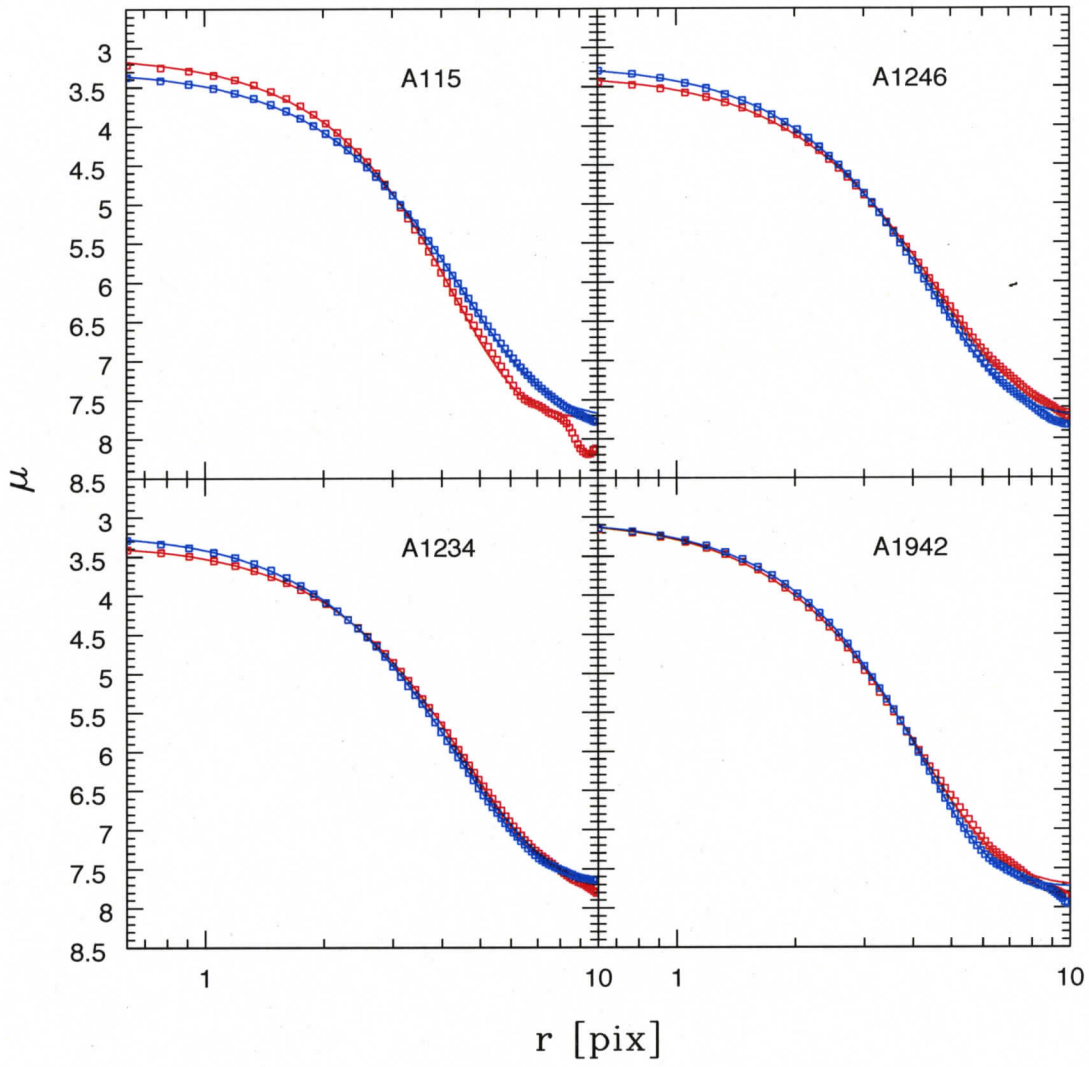

Figure 3.1: Moffat profile fits (solid lines) to selected PSF star flux (points) in four cluster images for g' (blue) and r' (red) data.

data. The resulting PSF is then used as a response function when fitting a PSF convolved model to the observed BCG profile.

3.3 Surface Brightness Fitting Procedure

A PSF-convolved, circularly-symmetric, single-$r^{1/4}$ deVaucouleurs profile is fit to the observed surface brightness of the BCGs. The model is fit directly to the source count distribution and has the following form:

$$I(r) = I_e \exp\left(-b((r/r_e)^{1/4} - 1)\right) + I_{bgd} \tag{3.5}$$

I_e and r_e are the effective intensity and effective radius respectively. The term I_{bgd} is a constant background intensity term which is also included as a fit parameter. The parameter b is set to -7.67 such that r_e corresponds to the radius enclosing exactly half the light of the galaxy. We determine the parameters I_e and r_e by performing a downhill simplex χ^2 minimization routine with χ^2 measured in the following way:

$$\chi^2 = \sum \frac{(I_{j,mod}(r) - I_{j,obs}(r))^2}{\sigma^2(r)} \tag{3.6}$$

Error estimates used for σ are obtained by boot-strapping the pixel values in each data bin. We randomly sample the pixels in an individual bin, allowing a given pixel to be selected multiple times. The total number of pixels randomly sampled from a single bin is kept equal to the total number of unmasked pixels available for selection in that bin; thus keeping fixed the total number of pixels per measurement. This last step is crucial to maintaining the poisson noise characteristics of each bin. The randomly selected pixels from each bin are then used to a measure a BCG surface brightness profile. This procedure is repeated $N_{pro} = 100$ times and the value of $\sigma_{rms}(r) = \sqrt{\sum (I_j(r) - < I(r) >)^2}$ within this set of 100 measurements is adopted as the error in the profile for the corresponding radial bin. The choice of

using $N_{pro} = 100$ random profiles in error estimation is based on resolution-type tests of the effect of varying N_{pro} and observing the resulting change in σ. There are some major benefits to using this method of error estimation. It is not required that we make any assumption of the functional form of σ (ie. poisson noise), nor are we required to know the precise values of exposure times, gain or read-noise. In fact, this technique is quite nice because not only can it account for the random noise in our data, it also incorporates some of the contribution to σ from non-uniform, systematic variations (bright stars, variability in galactic dust absorption, crowding effects of nearby galaxy/group light, etc.) across the image of the cluster. Unfortunately because nothing in life is free, there are some shortcomings of the boot-strapping method. Boot-strapping estimates of σ fail to represent the true error in any radial bin that has only a few pixels available to randomly sample. This results in the 100 surface brightness measurements becoming highly correlated and causes the estimated σ at that radius to be small while the true σ is actually large. By careful choice of the radial range over which we fit our model we can circumvent some of this complication however.

We restrict the BCG fitting procedure to data points at radii larger than twice the fwhm of the derived moffat profile PSF ($r_{fit} > 2r_{fwhm}$). This avoids using the central bins where we know the small number of pixels per bin has led to an underestimate in σ which in turn gives too much weight to those bins when fitting χ^2. Ignoring the central bins also helps to ensure that any error in the PSF fit or convolution process will not seriously affect the surface brightness fitting procedure. In addition we apply an upper radial cutoff to the fitting region. The fit is initially restricted to those data points that lie at radii less than $500h_{70}^{-1}kpc$ from the BCG center. This radius is chosen somewhat arbitrarily but it reflects our effort to isolate the BCG/ICL component within the overall cluster potential. The PSF-convolved deVaucouleurs + background model is then fit to the data lying within these two limits. A second iteration of the fit is then performed with the maximum fit radius

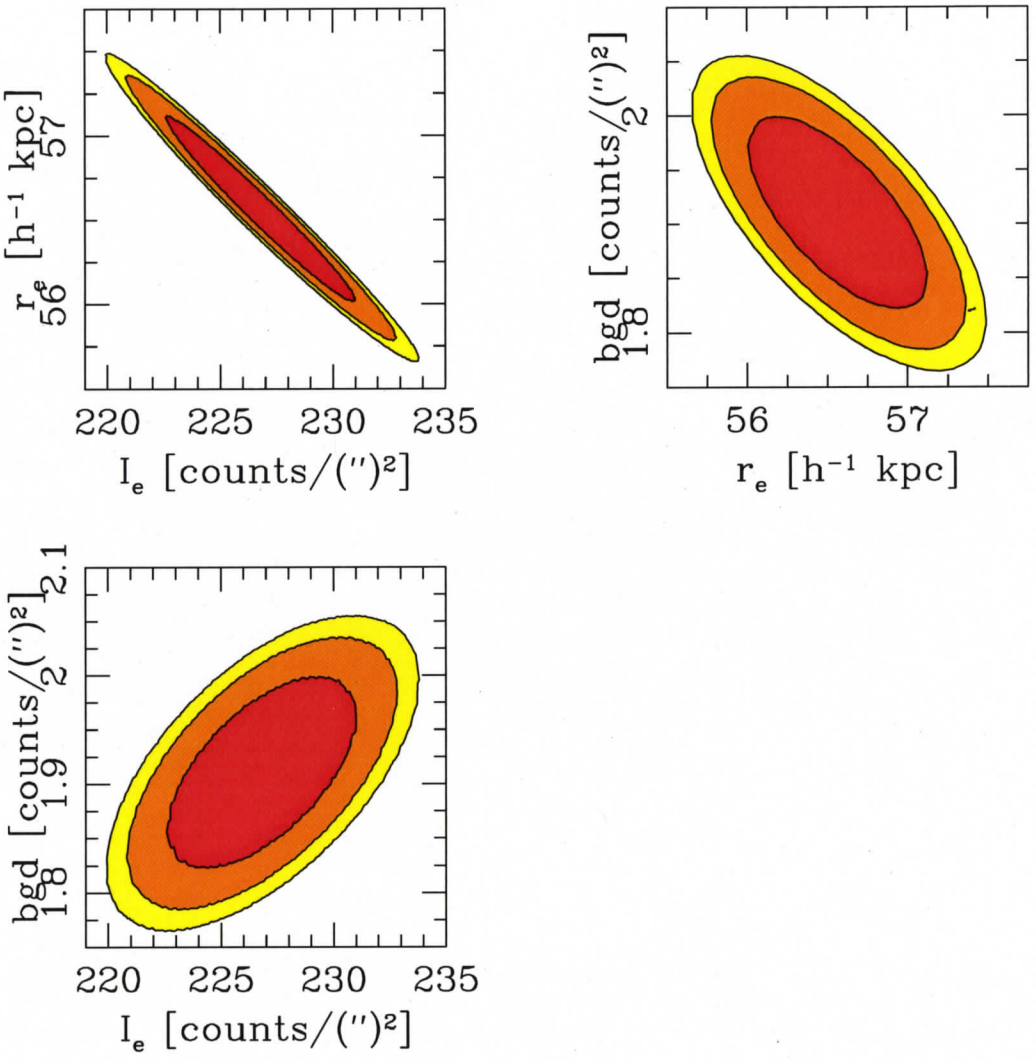

Figure 3.2: marginalized χ^2 contours of r' surface brightness fit parameters for Abell 2259. The contours are shaded according to confidence level: 1σ in red, 2σ in orange and 3σ in yellow. The most notable degeneracy is between r_e and I_e

set to $1.5r_{e,initial}$ and an extra term added to χ^2 as calculated by equation 3.6. The second fit iteration uses a χ^2 calculated by the following:

$$\chi^2_{new} = \chi^2_{initial} + \left(\frac{I_{bgd,new} - I_{bgd,initial}}{\sigma_{bgd,initial}}\right)^2 \tag{3.7}$$

where the subscripts *initial* and *new* refer to the first and second fit iteration parameters respectively. The extra background term in χ^2_{new} acts as a penalty term to any major change in the background parameter and ensures that the background is primarily determined/constrained by the larger radius fit range. The reduction in the fit range of the second fit iteration helps to further isolate the BCG signal and give a more robust result in terms of r_e and I_e.

Values for the fit parameters effective intensity I_e, effective radius r_e and background intensity I_{bgd} are found by locating the minimum in χ^2 space, but the uncertainties and degree of degeneracy between parameters are still not known. We map out the local $(\chi^2, I_e, r_e, I_{bgd})$ space in a small region around the best fit values in order to estimate the formal uncertainty in the fit parameters. For each possible combination of 2 parameters we marginalize over the third parameter and compute the 1 to 3 σ confidence limits in the resulting 2 parameter χ^2 subspace. The 1σ, 2σ and 3σ contours are defined as the locus where $\Delta\chi^2 = \chi^2(I_e, r_e, I_{bgd}) - \chi^2_{best} = 2.30, 4.61$ and 6.17 respectively. Examples of the resulting parameter contours are shown in figures 3.2 and 3.3. From this analysis it is easily seen that I_e and r_e are the most degenerate parameter pair, highlighting a general trend that persists for all of the BCG fits in the CCCP cluster sample. By examining the shape of the χ^2 surface we can easily see how a change in one parameter can effect the resulting determination of another. It is important to examine these diagrams in order to evaluate the effect of background subtraction on the resulting model fit parameters. By inspection of the χ^2 contours, it is easy to see that an error in the background map is likely to bias the fit parameters in a systematic way. A 3σ error in the background can affect the derived r' effective radius r_e at the 3-4 % level for Abell 2259. BCGs with

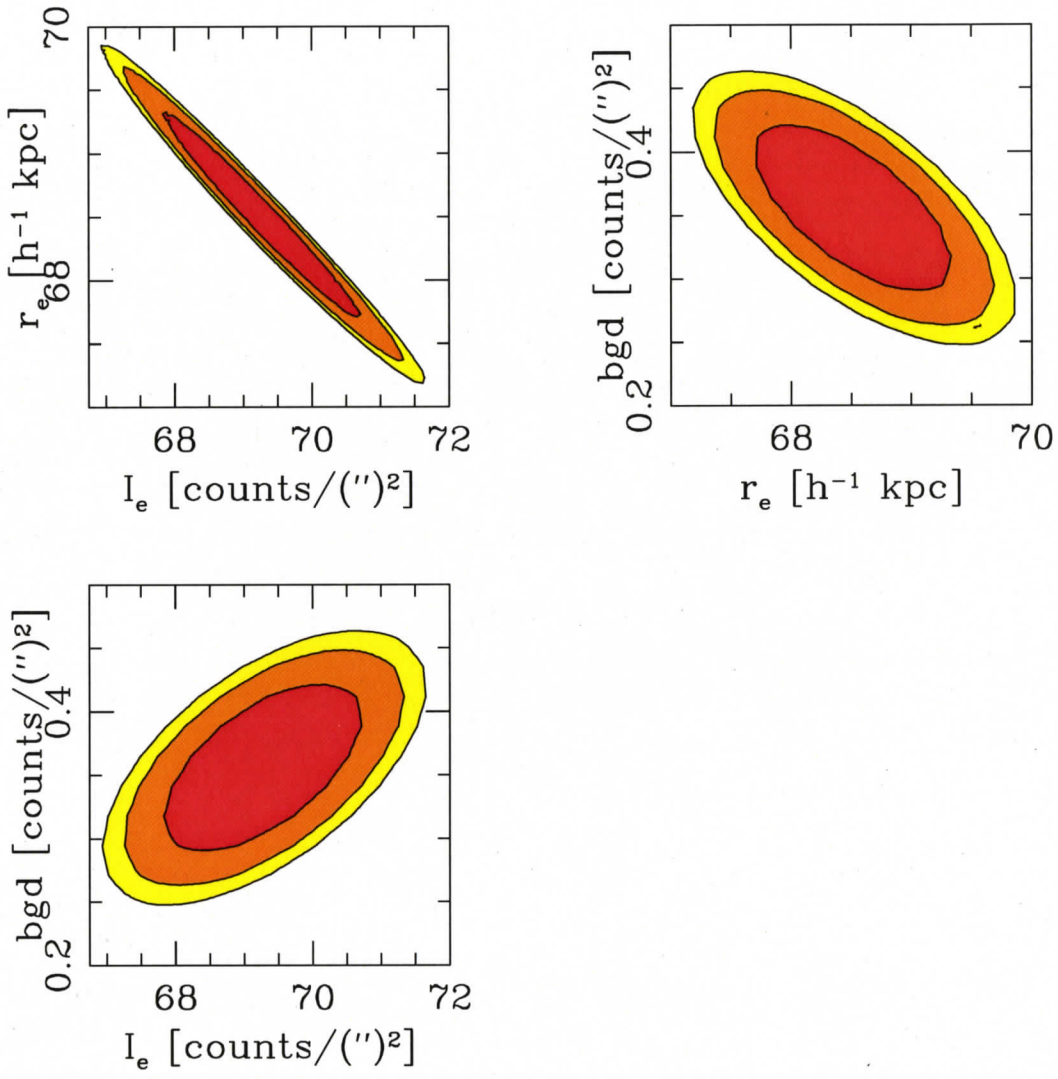

Figure 3.3: marginalized χ^2 contours of g' surface brightness fit parameters for Abell 2259. The contours are shaded according to confidence level: 1σ in red, 2σ in orange and 3σ in yellow. The most notable degeneracy is between r_e and I_e

smaller effective radii will be more vulnerable to this effect because they have less data points well above the background level to help constrain the fit.

Chapter 4

Quantifying Systematics

We wish to measure the surface brightness profiles of BCGs down to less than the 1σ background fluctuation limit. At these extremely low surface brightness levels there are a variety of systematic effects that can either mimic the signal that we wish to detect or hide it. In previous BCG and ICL studies there have been great efforts to understand and quantify these systematics in order to find ways of mitigating their effects and improving surface brightness measurements. In the following subsections we describe our efforts to quantify relevant systematics affecting the precision measurement of BCG surface brightness profiles within the CCCP sample.

4.1 Mask Incompleteness

A major source of systematic error present in BCG and ICL studies is the effect of mask incompleteness. Because BCGs are found in clusters, on top of large peaks in the field of relative density fluctuations, they tend to be surrounded by many other bright cluster galaxies which act as sources of contamination to our signal of interest. There are several approaches that are commonly used to deal with this contamination effect. One possible approach is to mask everything brighter than some surface brightness limit μ_{lim}. This approach is adopted by Lin and Mohr 2004, Feldmeier et al. 2004, Zibetti et al. 2005, Krick et al. 2005 and others. While isophotal masking has the advantage that the methodology is clearly defined

and reproducible. The problem is that it is unclear what the measured signal corresponds to physically. In particular, it cannot easily be determined if the signal that is observed is due to the BCG, ICL or low surface-brightness wings that are not fully masked around galaxies (galaxy bleeding).

A second method that one might try is to remove the contamination prior to BCG profile measurement. This can be done by fitting surface-brightness models to all the galaxies in the field except the BCG, subtracting their model profiles from the original image and then measuring a BCG surface brightness profile with the contaminating sources removed. While this method seems very attractive in theory, there are many practical problems that prevent its proper execution. To investigate the validity of this method in more detail, we first run the iraf task ELLIPSE, centered on the BCG position, in order to generate an isophotal contour map of the BCG. When running ELLIPSE we use the mask generated by the procedure outlined in section 2.5. The resulting surface brightness map is then subtracted from the original image to allow for a more accurate determination of the non-BCG galaxy models. We use the GIM2D galaxy modeling package (Simard et al. 1998) in order to model all remaining galaxies in the cluster field and subtract them from the original image. Although this method may seem ideal, we find that the extended residuals resulting from the subtraction of many galaxies in a crowded field actually introduces an amount of uncertainty to the BCG surface-brightness profile that is comparable to that introduced by masking incompleteness. Since the systematic effects of masking incompleteness are actually easier to understand and quantify and the masking-only method is much faster, we find that there is no significant advantage to galaxy-subtraction method. These findings are similar to those discussed in Patel et al. 2006 and we direct the reader to this work for further discussion on this topic.

As a way of quantifying the effect of mask incompleteness we measure the BCG profile in four different quadrants. The profiles should be symmetric in all four

quadrant for a pure BCG with no contamination. Any dispersion between the four profiles for a given BCG is therefore indicative of some systematic deviation for that galaxy. We place the divisions along semi-major and semi-minor axes such that the four quadrants represent the following intervals:

Q1. $\phi < \theta < \phi + \pi/2$

Q2. $\phi + \pi/2 < \theta < \phi + \pi$

Q3. $\phi + \pi < \theta < \phi + 3\pi/2$

Q4. $\phi + 3\pi/2 < \theta < \phi + 2\pi$

where ϕ denotes a constant average position angle of the BCG. We show the resulting profiles in figures for two of the BCGs in the CCCP sample in figure 4.1 and figure 4.2.

The lower two panels of figures 4.1 and 4.2 show surface brightness profiles as measured in the four quadrants Q1 through Q4 for Abell 2261 and Abell 2537. We expect that some of the systematic deviation seen in these profiles is due to mask incompleteness. The galaxies within a given cluster field are not uniformly distributed in azimuth and any masking incompleteness should contribute to the dispersion in surface brightness profiles as measured in Q1 through Q4. There is some cause for concern if the positional distribution of cluster member galaxies is aligned with the major axis of the BCG. In such case we would expect this test to fail as a check of mask incompleteness because the mask would be symmetrically incomplete in all four quadrants. However, this alignment would need to be near perfect and galaxies of equal magnitude would need to balance each other on opposite sides of the BCG in order to hide all the dispersion signal due to mask incompleteness. Such perfect alignments are not seen when visually inspecting the images (see figure 2.1). There are other possible systematic effects that can create surface brightness dispersion in the four quadrants. A gradient in the background or a position angle twist may also create some degree of dispersion in the profiles. Although the effect of the latter is symmetric in two quadrants and anti-symmetric

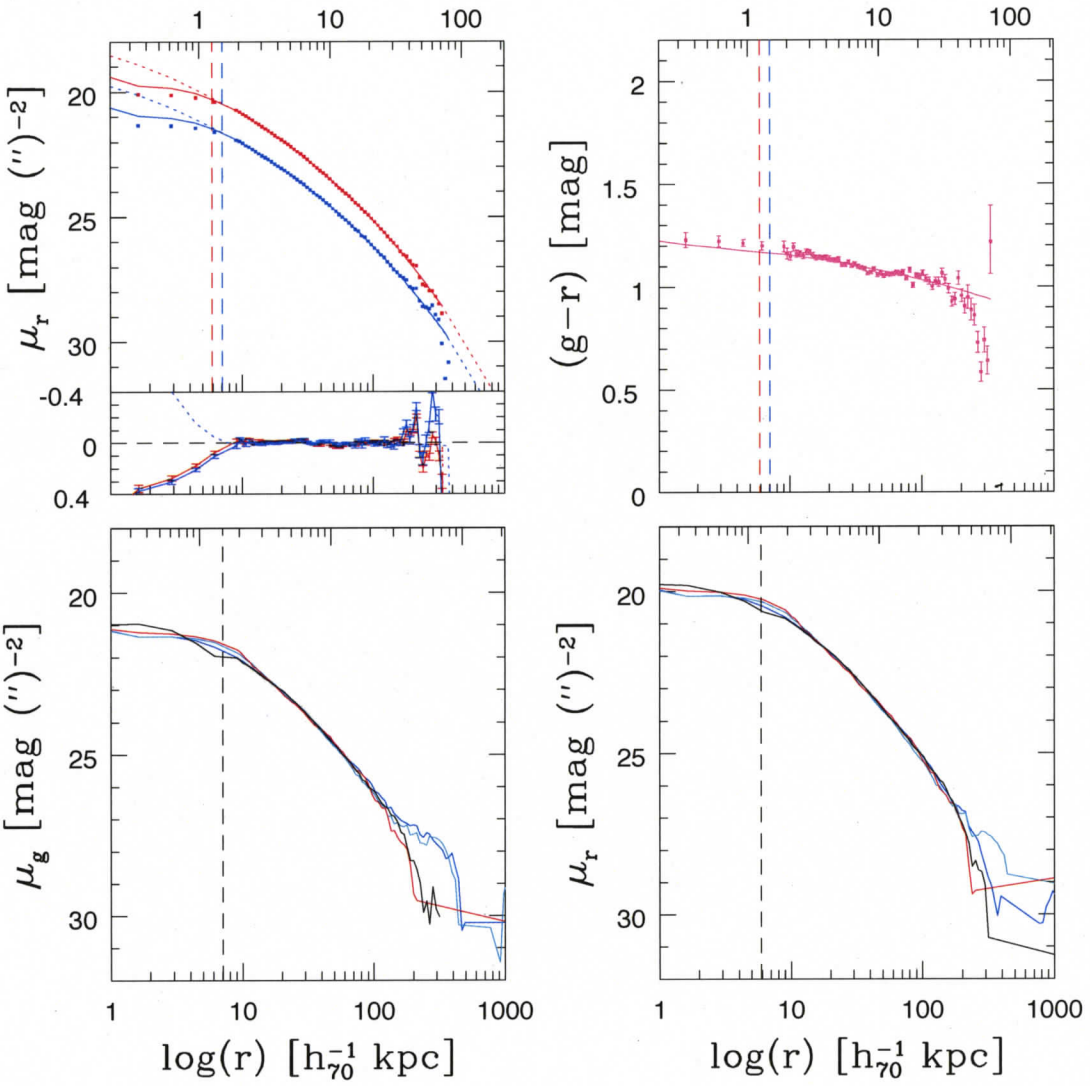

Figure 4.1: Tests for systematics in the radial profiles of the BCG in Abell 2261. The upper left panel shows the surface brightness in g' (blue) and r' (red). Points correspond to measured data while solid and dotted lines correspond to surface-brightness fits with and without psf convolution respectively. In all panels the horizontal dashed lines represent 2α seeing limit of the moffat psf. The residuals sub-panel shows the difference between psf convolved model and the data (solid line) and the difference between psf convolved and non-psf convolved models (dotted line). Error are calculated by the bootstrap method outlined in section 3.3. The upper right panel displays (g'-r') color profiles. Points represent the measured data while solid lines show the difference between g' and r' surface brightness model fits. The two lower panels correspond to g' (left) and r' (right) surface brightness as measured in the four quadrants, Q1 through Q4, as defined above. Each color corresponds to the profile measured in a different image quadrant.

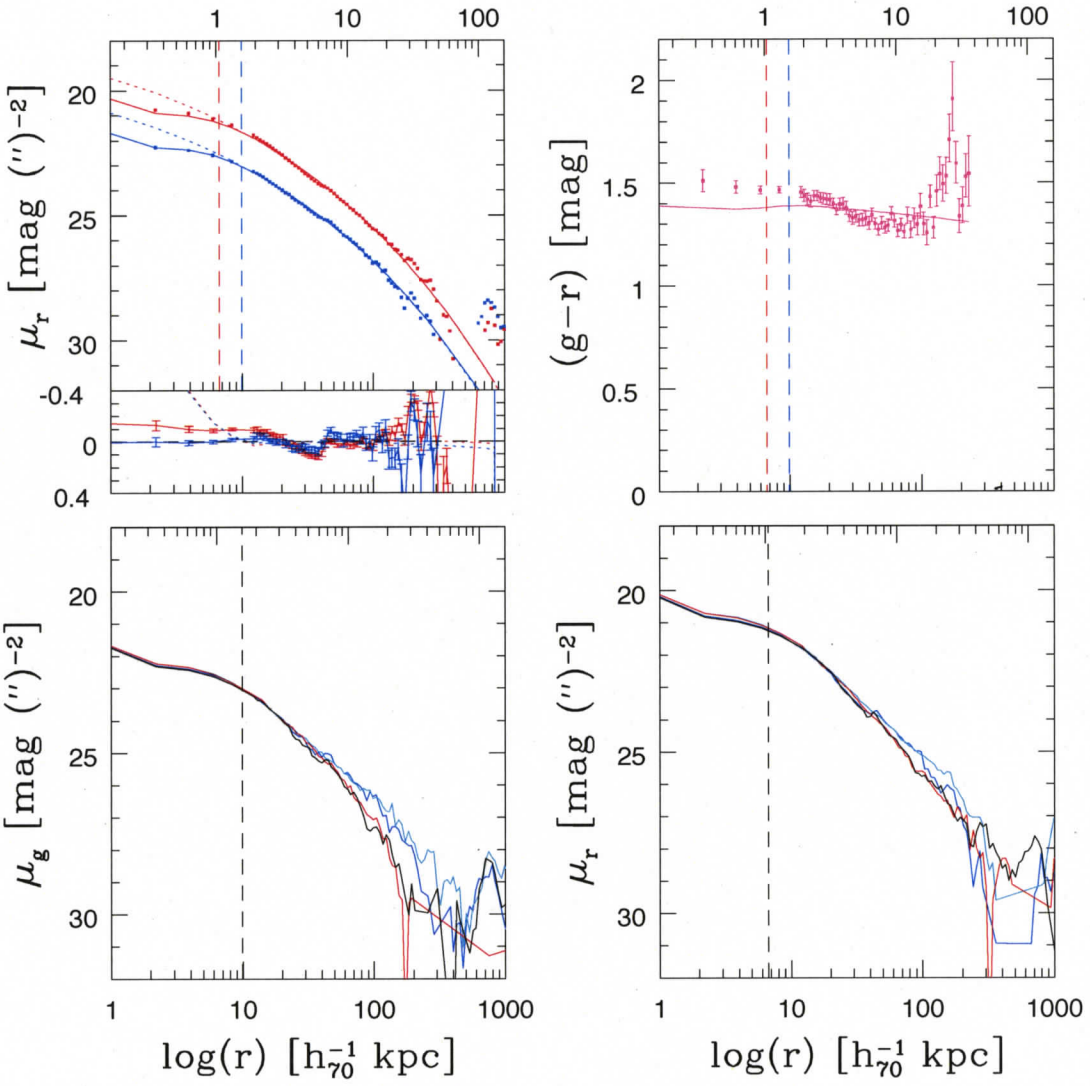

Figure 4.2: Tests for systematics in the radial profiles of the BCG in Abell 2537. The upper left panel shows the surface brightness in g' (blue) and r' (red). Points correspond to measured data while solid and dotted lines correspond to surface-brightness fits with and without psf convolution respectively. In all panels the horizontal dashed lines represent 2α seeing limit of the moffat psf. The residuals sub-panel shows the difference between psf convolved model and the data (solid line) and the difference between psf convolved and non-psf convolved models (dotted line). Error are calculated by the bootstrap method outlined in section 3.3. The upper right panel displays (g'-r') color profiles. Points represent the measured data while solid lines show the difference between g' and r' surface brightness model fits. The two lower panels correspond to g' (left) and r' (right) surface brightness as measured in the four quadrants, Q1 through Q4, as defined above. Each color corresponds to the profile measured in a different image quadrant.

in the other two. Because of the assumption of a constant position angle in this analysis, a significant position angle twist would cause the four profiles to deviate from the mean profile in opposing-quadrant pairs. The resulting pairs are more representative of the surface brightness profiles along the major and minor axes. The effects of position angle twisting is seen in figure 4.1 of Abell 2261 at small radius ($r \lesssim 15 h_{70}^{-1} kpc$) where the profiles seem to diverge in pairs. The large radius pairwise divergence of the profiles in A2537 is due to the presence of a group of bright galaxies on one side of the BCG and an absence of bright galaxies on the opposing side. We therefore attribute this divergence in the profiles of the four quadrants of Abell 2537 to be a genuine signal of mask incompleteness. The fact that most of the BCG profiles in the CCCP sample have dispersions in their four quadrants more representative of Abell 2261 is encouraging. Although this is not a perfect test of mask incompleteness, based on this procedure we are able to reject any BCG that shows a large dispersion between profiles at radii smaller than the effective radius r_e from further analysis of our sample.

4.2 Background Variation and Large Scale Error

Another major source of systematic error in BCG/ICL studies comes about from large scale flat fielding error and higher order spatial variation in the background. Feldmeier et al. 2002 and Patel et al. 2006 present methods that may be used in order to quantify some of the properties of background variation on a variety of scales. We use similar methods here in order to quantify the image background variation and determine the surface brightness level to which we believe our measurements are accurate. We divide each image into a regular rectangular grid. The background signal is then determined within each grid square using the same mask that is used to measure BCG surface brightness. Within each grid square the pixel

values are then binned and the median, mode, mean and σ are determined. This process is repeated with variety of grid sizes in order to examine background variation on different scales. Figure 4.3 shows a summary of the results for the r' image of Abell 611. The lower left panel displays the median background measurements for the smallest grid scale of 47x47 with the side length measured in pixels. These median values are plotted versus the radial distance away from the BCG centroid. These data are then binned in radius and the mean of all median background values $< median > (r)$ as well as the variation in the median background values $\sigma(r)$ within each radial bin are computed. These results are shown in the lower and upper right panels respectively of figure 4.3. The upper left panel displays the large scale error converted to a surface brightness in $mag\ (")^{-2}$. This large scale error represents the σ_{rms} of the median background values from grid square to grid square. The large scale error is shown as a function of the grid square side length d. For comparison the 1σ limiting surface brightness μ_σ is also shown as a dashed horizontal line.

From the background properties of the r' image of Abell 611 shown in figure 4.3 it is easy to see that there exists some degree of structure in the background that varies with scale. Upon examination of the rest of the CCCP cluster images we detect similar signatures of background structure on a variety of scales. By using the techniques of Felmeier et al. 2002 and Patel et al. 2006 we have shown that there is a significant amount of large-scale variation resolvable in our images. We would like to go one step further however and quantify the effect of this large-scale variation on our measured surface brightness profiles and in particular to what surface brightness can we accurately measure the BCG light.

The following test has been devised in order to determine the reliability of the measurement of BCG light at large radius and faint surface brightness in the presence of large-scale variation of the image background. We begin by selecting 10 random locations on the image with the condition that they lie far from the BCG.

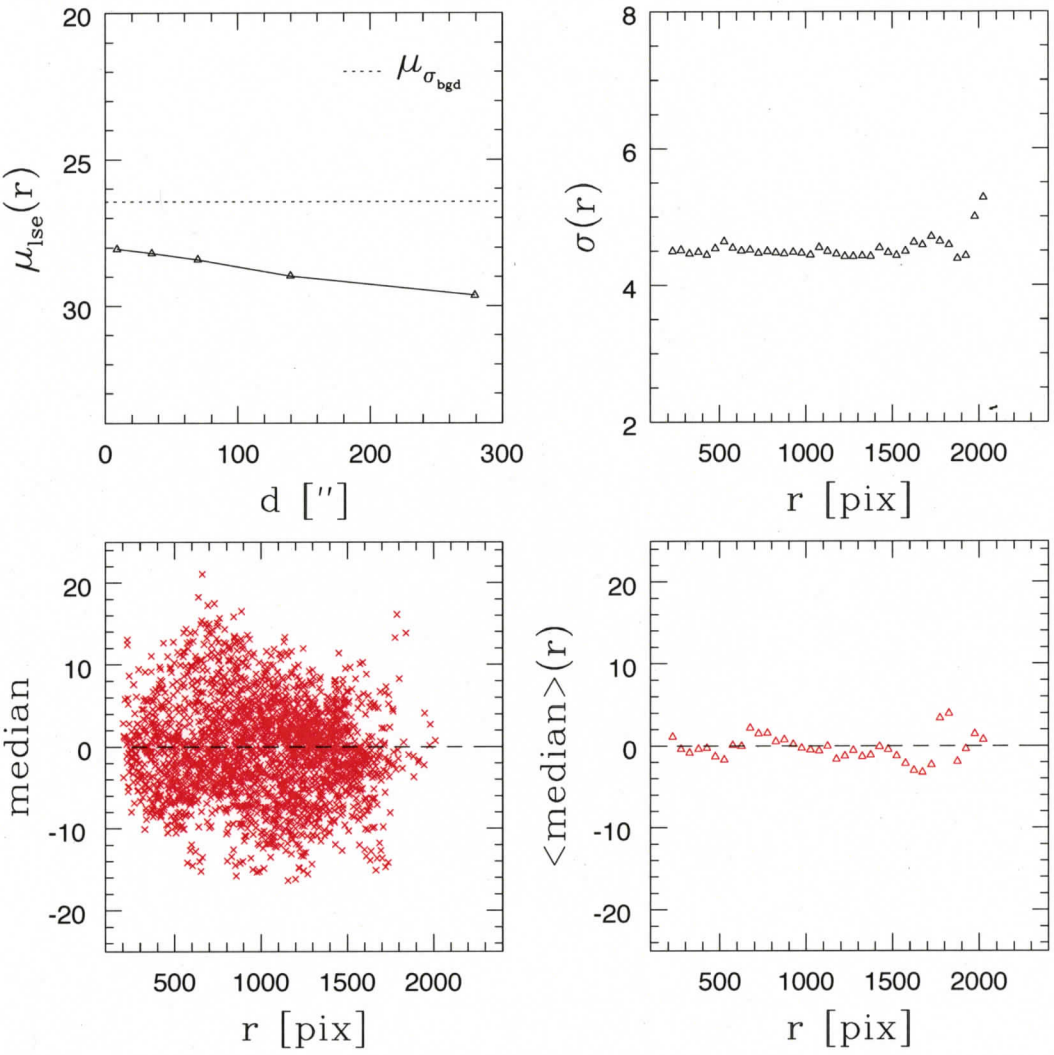

Figure 4.3: Background statistics for the r' image of Abell 611. The upper left panel shows the large scale error as a function of grid size. The 1σ limiting surface brightness μ_σ is shown as a horizontal dashed line. The lower left panel shows the median background values within each 47x47 pixel grid square plotted against radial distance from the BCG centroid. The upper right and lower right panels show $\sigma(r)$ and $< median > (r)$ respectively in each radial bin.

The procedure of masking and measuring the surface brightness is then carried out at each random location in the exact same manner as when the image is centered on the BCG. The key to this analysis is the large field of view of MegaCam ($\sim$ sq. degree). Since the BCGs typically only occupy the central few arc minutes, we are able to select random image sections that are both far from the BCG and represent independent measurements of the background across the field. This type of analysis takes full advantage of the large scale information provided by MegaCam and is not possible with small imaging cameras. We present here the results for three different sets of blank fields, separated at large distances from the clusters, in both g' and r' as examples of the background variation seen in the CCCP sample. Figures 4.4 through 4.9 represent the range in background variation that is seen in the sample.

The upper left panels in figures 4.4 through 4.9 show the mean and median intensity levels in units of integrated pixel value per $(")^2$ for the 10 randomly selected profiles. The corresponding BCG surface brightness is overplotted for reference. The intensity of the 10 randomly selected profiles are individually shown in the lower right panels of the figures. The lower left panels of figures 4.4 through 4.9 are the most interesting. The blue line corresponds to the observed rms scatter in the 10 profiles. This scatter reflects the total effect of all background variations on a variety of scales and is essentially the power spectrum of the observed noise. We also plot in red the best case scenario where the only noise is the expected poisson noise contribution σ_{best}:

$$\sigma_{best} = \frac{\sigma_{(")^2}}{\sqrt{n}} \tag{4.1}$$

where $\sigma_{(")^2}$ is the rms variation in a square arcsecond patch of sky and n is the number of square arcsecond patches in a single image. We have to plot $10\sigma_{best}$ in order to view it on a comparable scale to the observed noise. The number of pixels in each surface brightness bin are plotted in black. From the difference between the observed noise (σ_{obs}) and the pure photon noise curves we are able to identify when

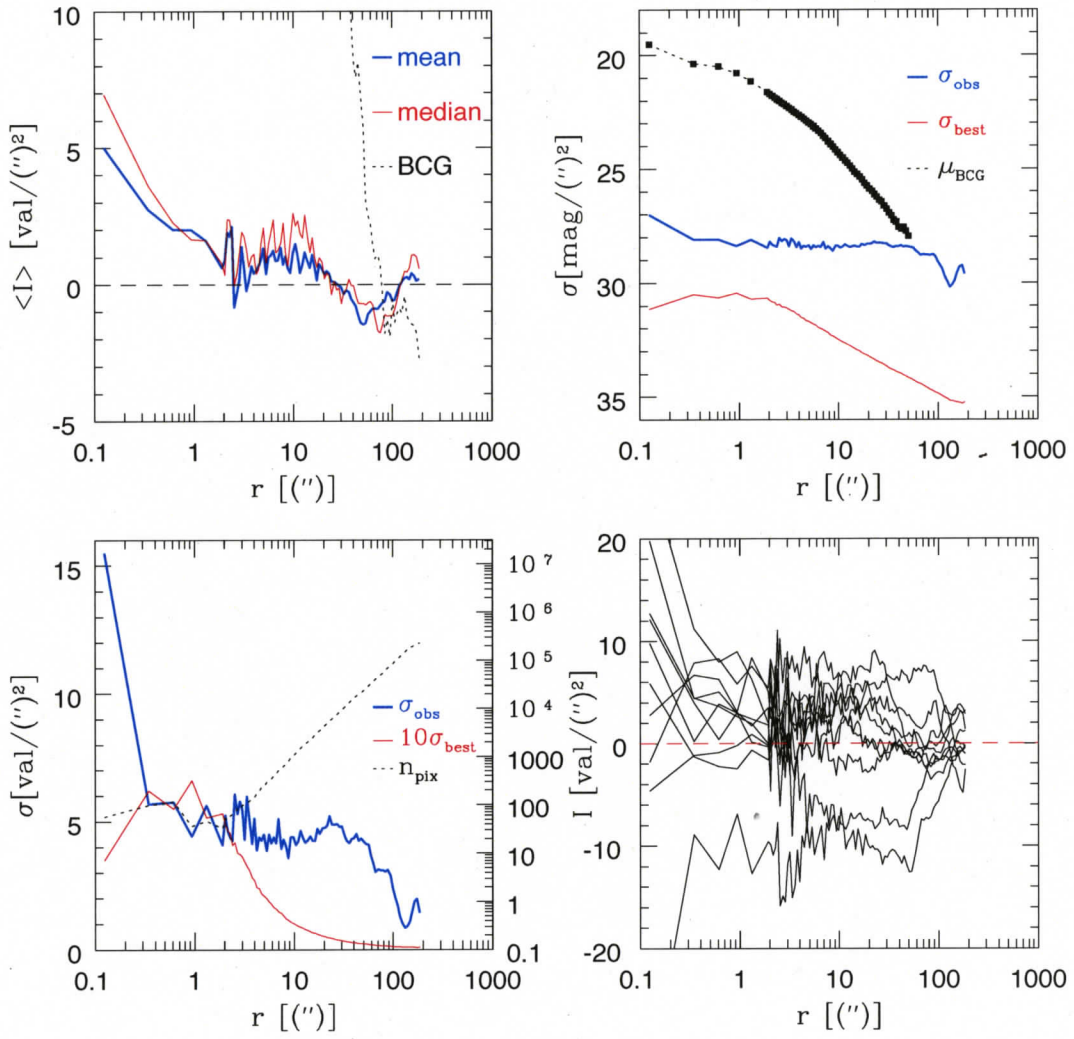

Figure 4.4: SB fluctuations: Abell 115 in r' - Upper Left: mean and median intensity of 10 randomly selected background profiles in blue (thick) and red (thin) respectively. The black (dotted) line shows the observed BCG signal level. Lower Left: observed noise σ_{obs} is plotted in blue (thick) and 10 times the best case poisson noise only σ_{best} is plotted in red (thin). The black (dotted) line denotes the log number of pixels in each radial bin. Upper Right: σ_{obs} and σ_{best} converted into mag $(")^{-2}$ in blue (thick) and red (thin) respectively. BCG surface brightness in shown in black (dotted) for comparison. Lower Right: individual measured intensities of 10 randomly selected background profiles.

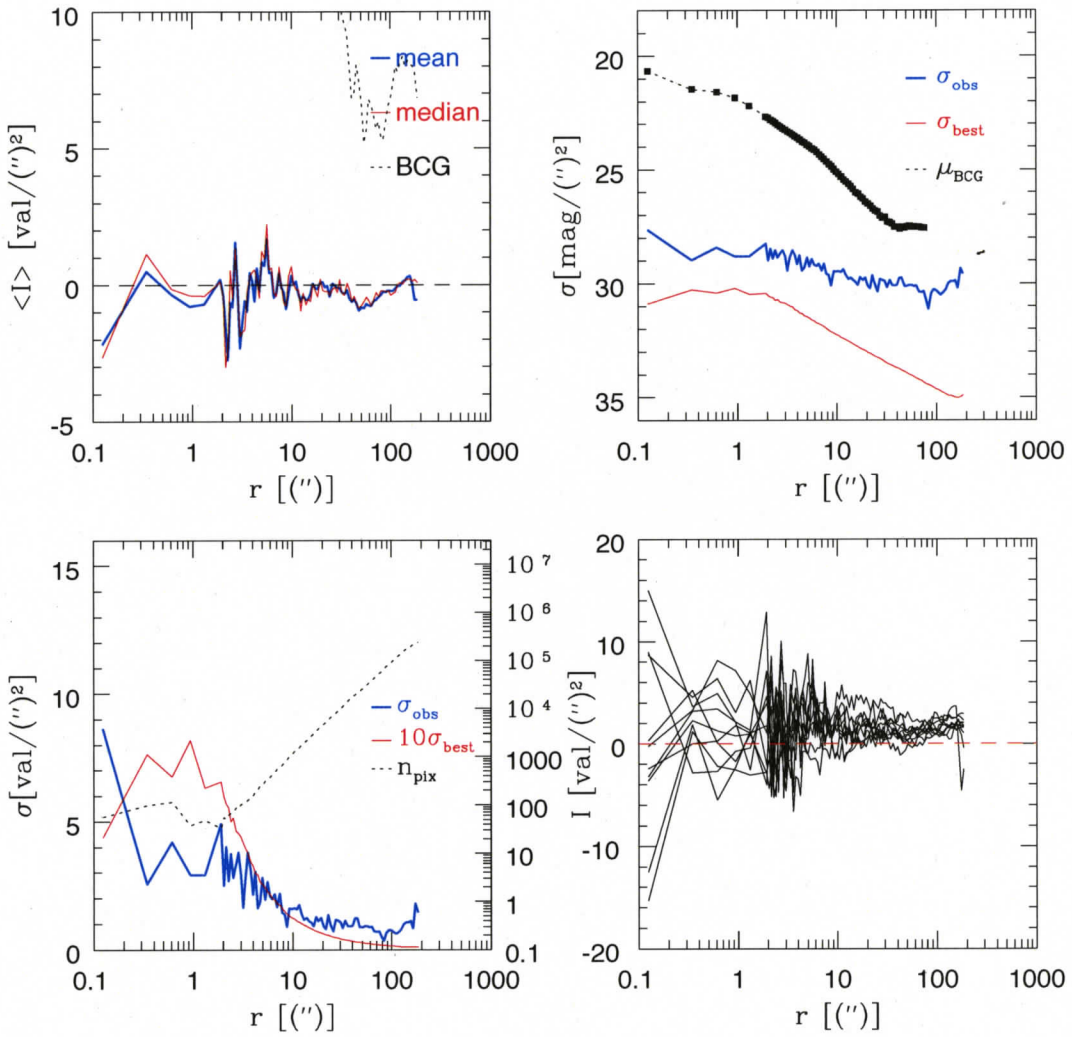

Figure 4.5: SB fluctuations: Abell 115 in g' - see figure 4.4 for description

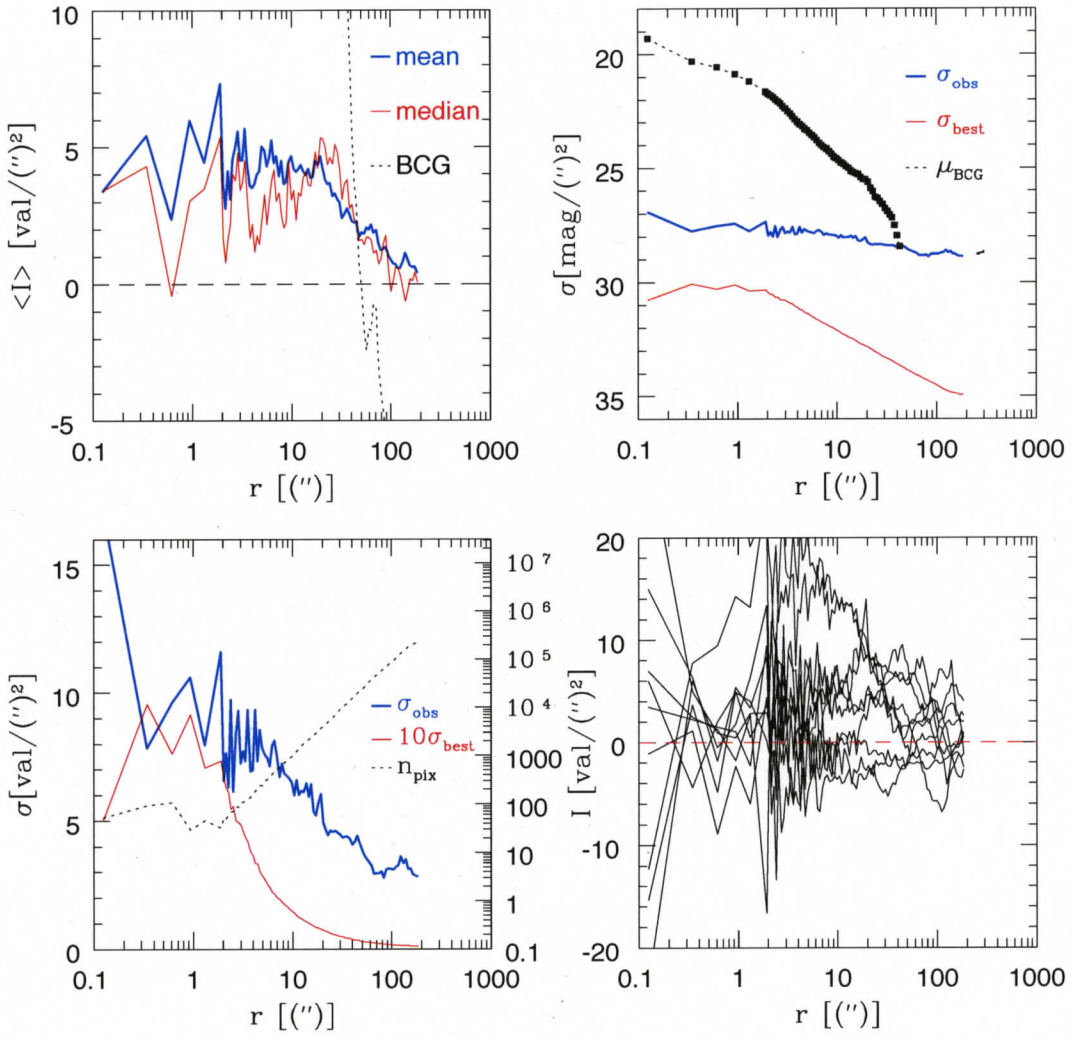

Figure 4.6: SB fluctuations: Abell 520 in r' - see figure 4.4 for description

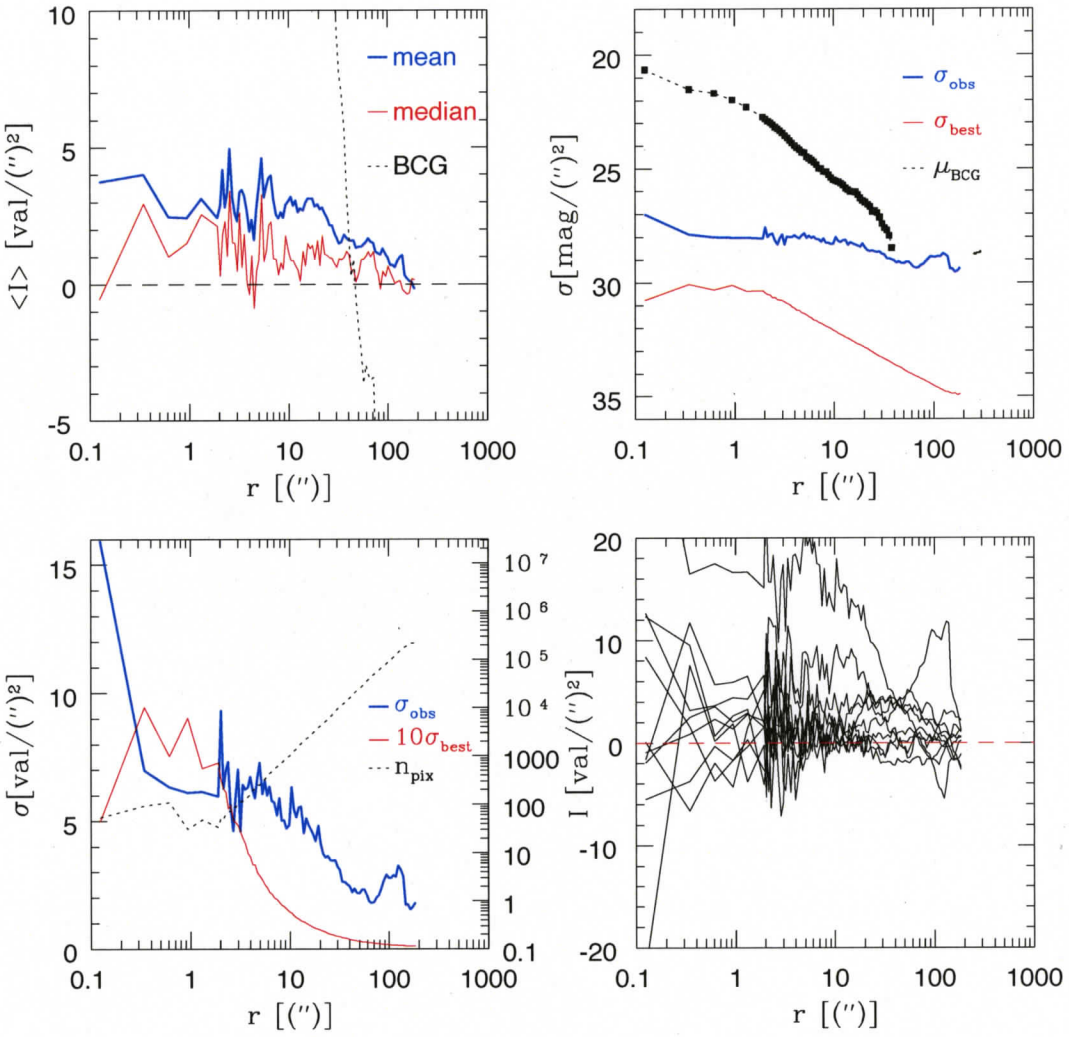

Figure 4.7: SB fluctuations: Abell 520 in g' - see figure 4.4 for description

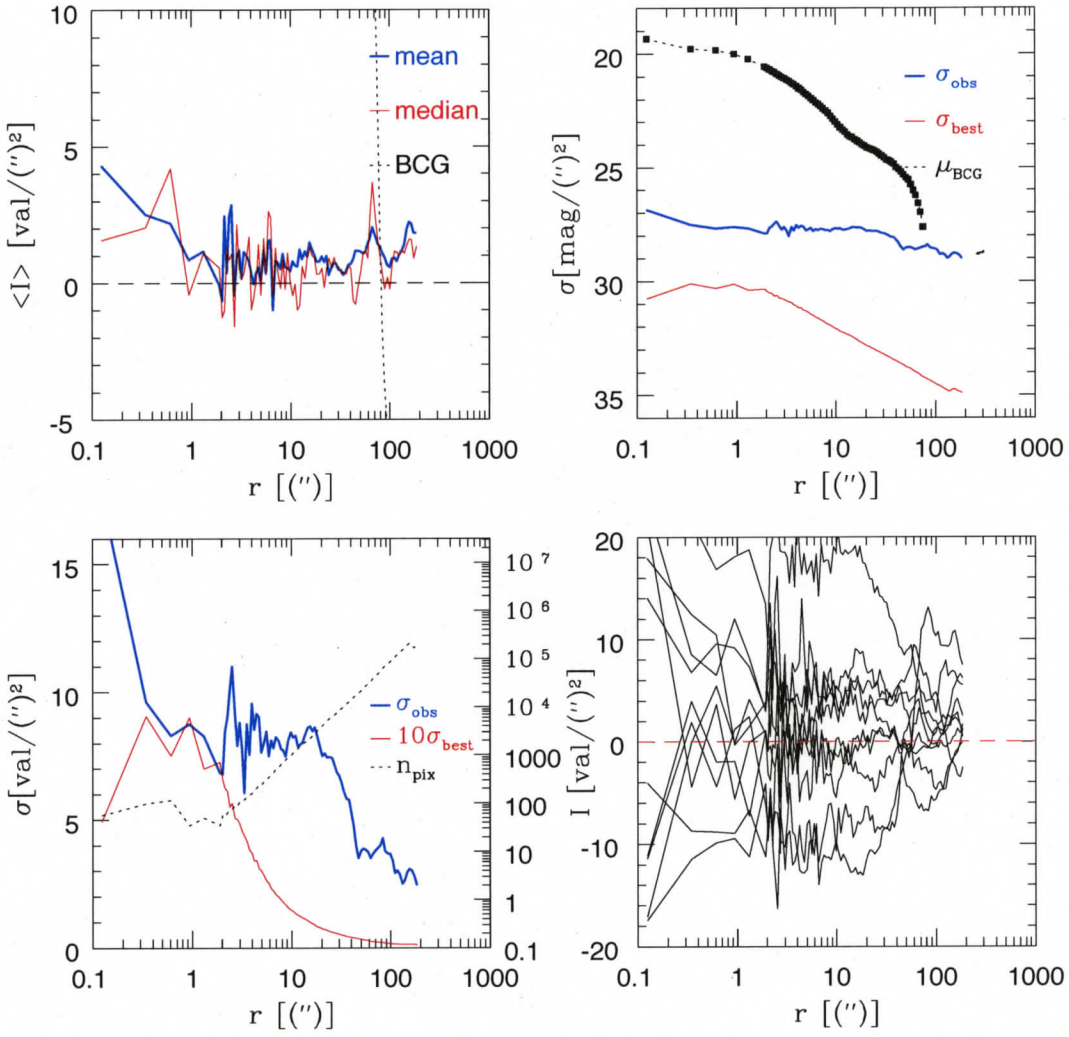

Figure 4.8: SB fluctuations: Abell 2204 in r' - see figure 4.4 for description

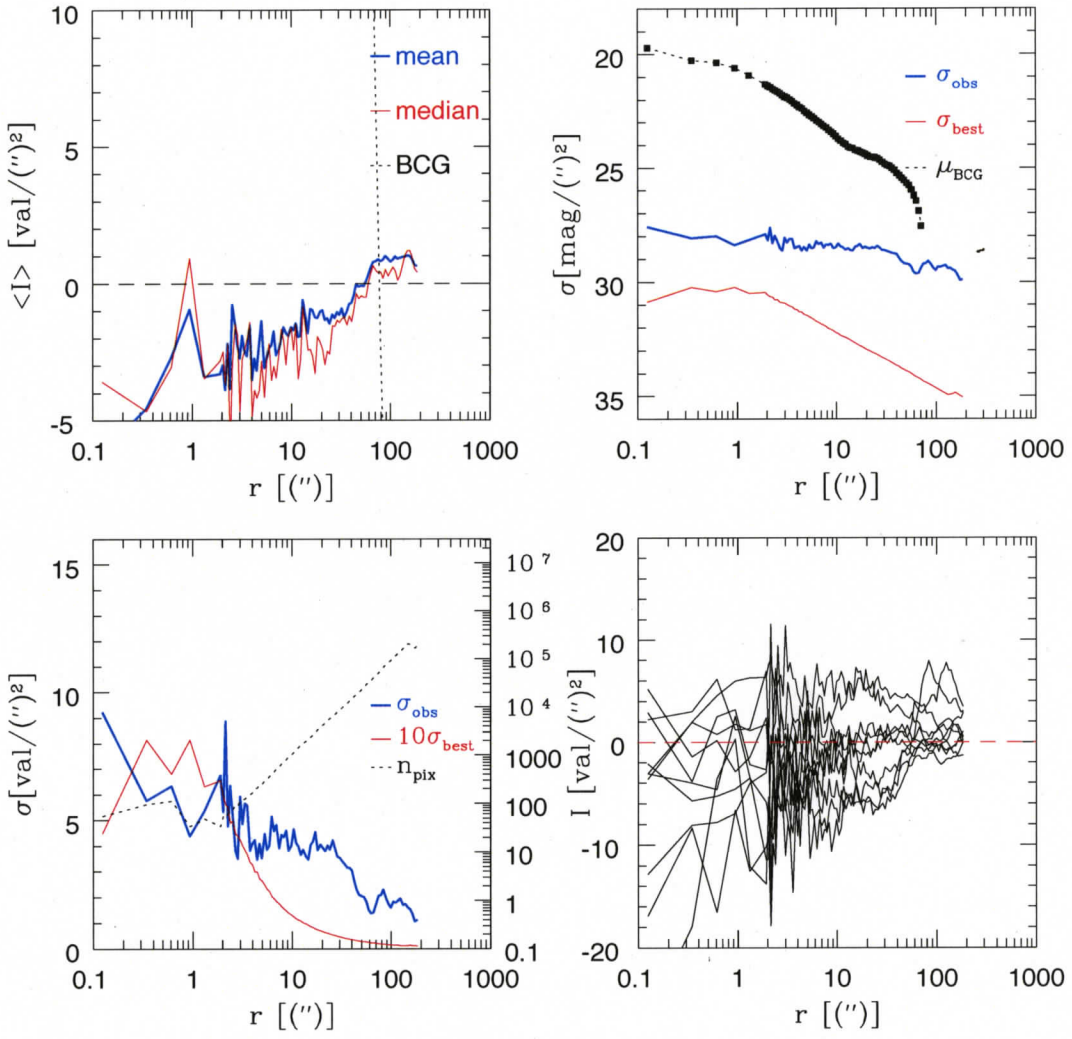

Figure 4.9: SB fluctuations: Abell 2204 in g' - see figure 4.4 for description

the systematic background variation becomes most important. The upper right panels figures 4.4 through 4.9 show the observed variation and poisson contribution converted into a surface brightness limit in $mag\ (")^{-2}$ as well as the BCG profile for comparison. These figures show that it is possible to accurately measure down to very faint surface brightness levels ($\sim 28\ mag\ (")^{-2}$) at large radius ($\sim$ 50-100") from the BCG before the effect of background variability begins to confuse the signal.

We mention here that there is some concern that in the process of stacking and background subtraction there may have been some inadvertent pre-subtraction of the BCG signal that we are trying to measure. The tests presented in this section are not capable of detecting any pre-subtraction signature. The problem lies in the fact that we wish to determine the background structure as close to the source of interest as possible. But at the same time we are trying to measure the source itself to the largest radius and faintest surface brightness as possible. There is a natural confusion zone where the signal level and background level are quite similar and hard to separate. In order to verify that this pre-subtraction effect is not seriously limiting our ability to determine the BCG parameters we repeat our analysis on three different versions of the Abell 115 stack. In each of the three cases we have used a different value of the SWarp parameter BACK_SIZE that sets the scale in pixels of the mesh used in determining the background map. We create three separate stacks using a value of BACK_SIZE=(257,513,1025) for Abell 115. The process of surface brightness measurement and BCG model fitting is repeated as outlined in the previous sections. The resulting BCG parameters (r_e,μ_e) are within $1-\sigma$ of each other for the 257 and 513 cases and grow to the 5% level for the 1025 case. We conclude that the background mesh size is not limiting our ability to measure the BCG parameters although it may be removing some of the signal from ICL. The primary focus of this work is to measure BCG light profiles and we are satisfied that we can do this to a high degree of accuracy without being seriously affected

by systematics. Due to the difference between the observed image fluctuation and the best case scenario poisson contribution, we point out that with an even more sophisticated stacking and background determination algorithm one should be able to go even deeper with this data and perhaps place tight constraints on the levels of ICL present within these clusters.

Chapter 5 | *Optical Properties*

BCGs represent the most extreme cases of giant elliptical galaxies and populate the high mass end of the galaxy mass distribution. As rare and massive galaxies they provide useful tests for galaxy formation models. There is increasing evidence however, that BCGs differ in their global and structural properties as well as in their spectra when compared to non-BCG ellipticals of equal stellar mass (Blakeslee 1997, Bernstein et al. 2001, von der Linden et al. 2006). These differences are mainly thought to be a direct result of the extreme environments in which BCGs are constructed. A good way to probe these differences is to examine the spatially resolved optical structure of BCGs as well as their integrated properties. In this chapter we examine the surface brightness profiles, colors, positions on the red sequence and Kormendy relation for BCGs in the CCCP sample.

5.1 Surface Brightness Profiles

A galaxy may be given a hubble type classification from early type ellipticals and lenticulars (E/S0) to late type spirals (S/SB) simply by qualitatively examining its optical morphology. A more quantitative measure of galaxy type can be made by a detailed examination of a galaxy's surface brightness profile. Early type galaxies tend to have surface brightness profiles that are proportional to $e^{(r/r_e)^{1/4}-1}$ (often referred to as a de Vaucouleurs or $r^{1/4}$ profile) where r_e is the effective radius while late type disky galaxies typically have surface brightness profiles that are proportional to (e^{-r/r_d}) where r_d is the scale radius. A more continuous range in morphology is made possible by fitting a profile that is proportional to $e^{(r/r_e)^{1/n}-1}$ (Sersic or $r^{1/n}$

profile) with n left as a free parameter or by doing a bulge/disk decomposition in which one allows for a superposition of exponential and $r^{1/4}$ profiles. Because BCGs have elliptical morphologies we examine in this section the results of fitting simple, circularly symmetric, psf-convolved $r^{1/4}$ surface brightness models (see equation 2.1).

Figures 5.1 through 5.4 show the surface brightness profiles in the g' and r' bands for all BCGs in our sample. The measured data are shown by the points, solid lines correspond to best fit PSF-convolved $r^{1/4}$ models as described in the above section and dotted lines show similar fits without PSF convolution. Surface brightness data is color coded by wavelength band with r' data shown in red and g' data shown in blue. In all cases the BCGs are brighter in r' than g' with a typical offset on the order of one magnitude at all radii. Vertical dashed lines show the moffat PSF fwhm radius (r_{fwhm}). Residuals are shown along the bottom of each plot. In each sub-panel the dotted line corresponds to the difference between the PSF-convolved and non-PSF-convolved fits, and the solid lines with error bars show the difference between the PSF-convolved models and the measured data.

The model fits are of varying quality among the sample of CCCP BCGs. Some of the BCGs are well fit by an $r^{1/4}$ profile but for the most part we see a deviation from a pure deVaucouleurs profile at either small or large radii. It is noted that there are various models that one can choose to fit to the BCG surface brightness (single-$r^{1/4}$, Sersic $r^{1/n}$, double-$r^{1/4}$) and that some perform better than others. We stress that this work concentrates on what can be inferred from simple, circularly symmetric, single-$r^{1/4}$ profiles but we redirect the reader to the work of Gonzalez et al. (2005) and references therein for further discussion on the validity of various choices of surface brightness models.

For some of the observed profiles there appear to be sudden drops and subsequent sharp rises in the surface brightness (eg. Abell 223a, Abell 521, Abell 697, CL1938+54). These sudden changes in brightness are the effect of imposing a cir-

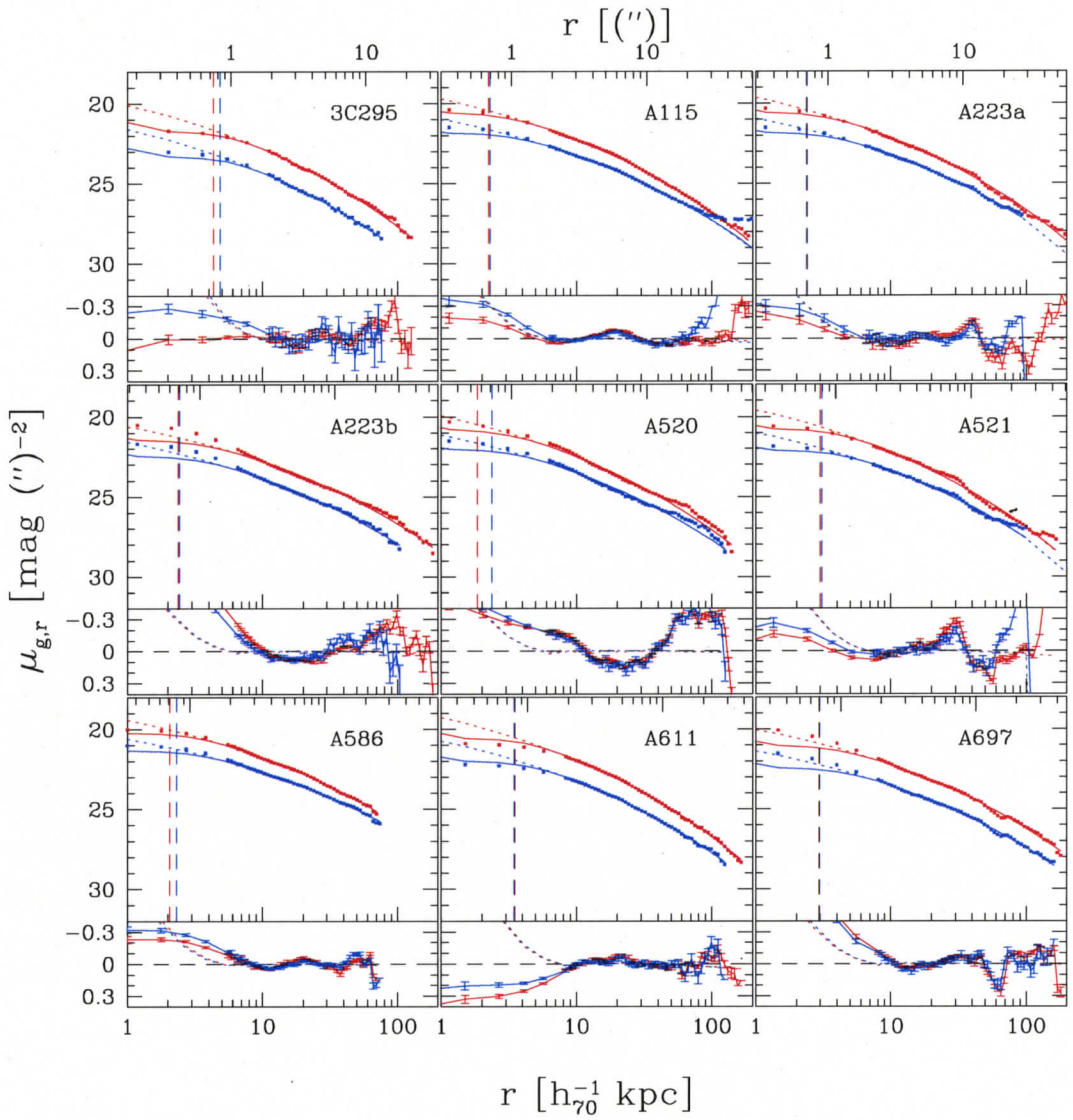

Figure 5.1: Surface brightnesses in g' (blue) and r' (red) for BCGs in the sample. Points correspond to measured data while solid and dotted lines correspond to fitted $r^{1/4}$ models with and without PSF-convolution respectively. Vertical dashed lines denote the r_{fwhm} seeing limit of the derived moffat PSF. Residuals are shown along the bottom with dotted lines showing the difference between fits with and without PSF-convolution and solid lines with error bars showing the difference between PSF-convolved models and the data. The top axis shows the corresponding radii in arcseconds

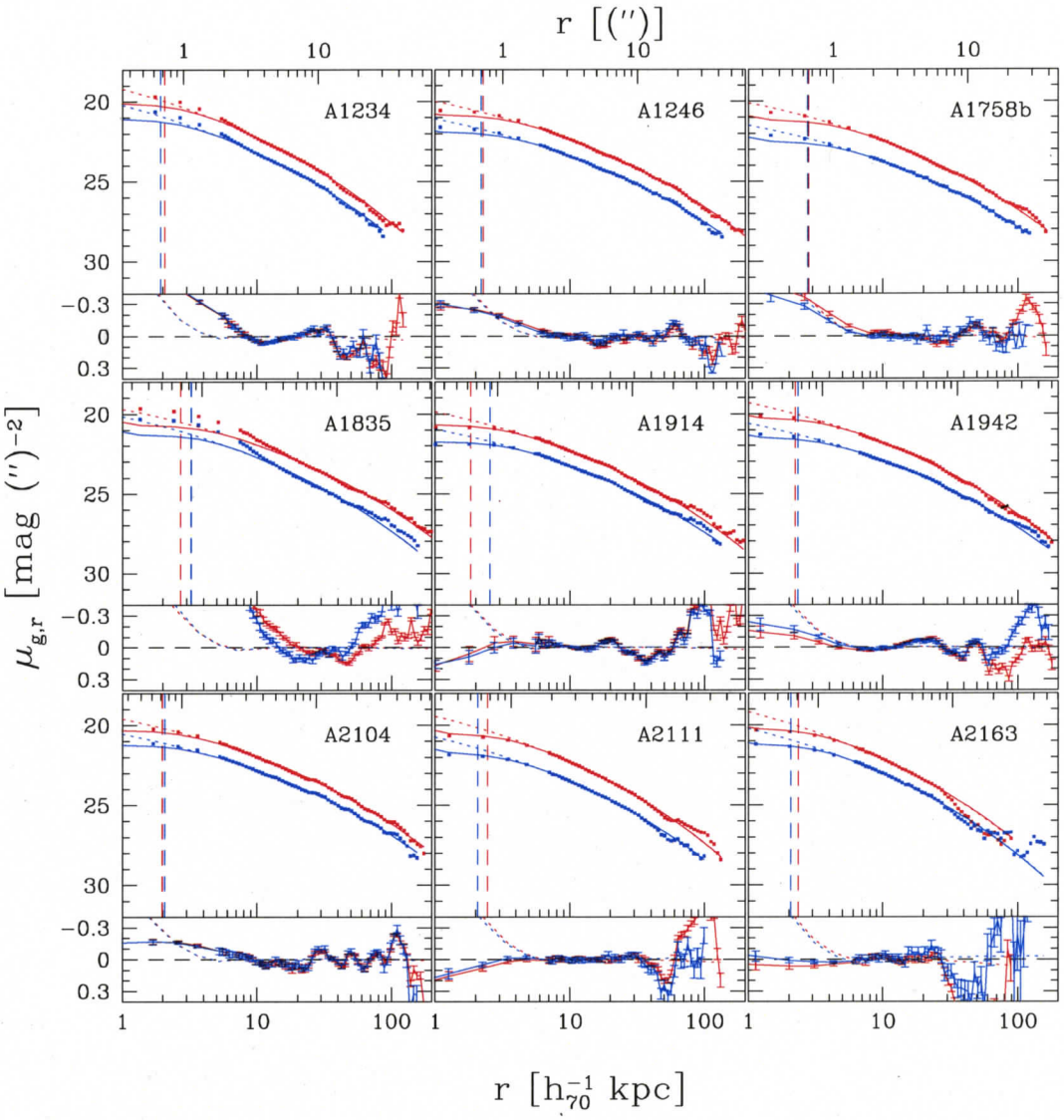

Figure 5.2: Surface brightnesses in g' (blue) and r' (red) for BCGs in the sample. Points correspond to measured data while solid and dotted lines correspond to fitted $r^{1/4}$ models with and without PSF-convolution respectively. Vertical dashed lines denote the r_{fwhm} seeing limit of the derived moffat PSF. Residuals are shown along the bottom with dotted lines showing the difference between fits with and without PSF-convolution and solid lines with error bars showing the difference between PSF-convolved models and the data. The top axis shows the corresponding radii in arcseconds

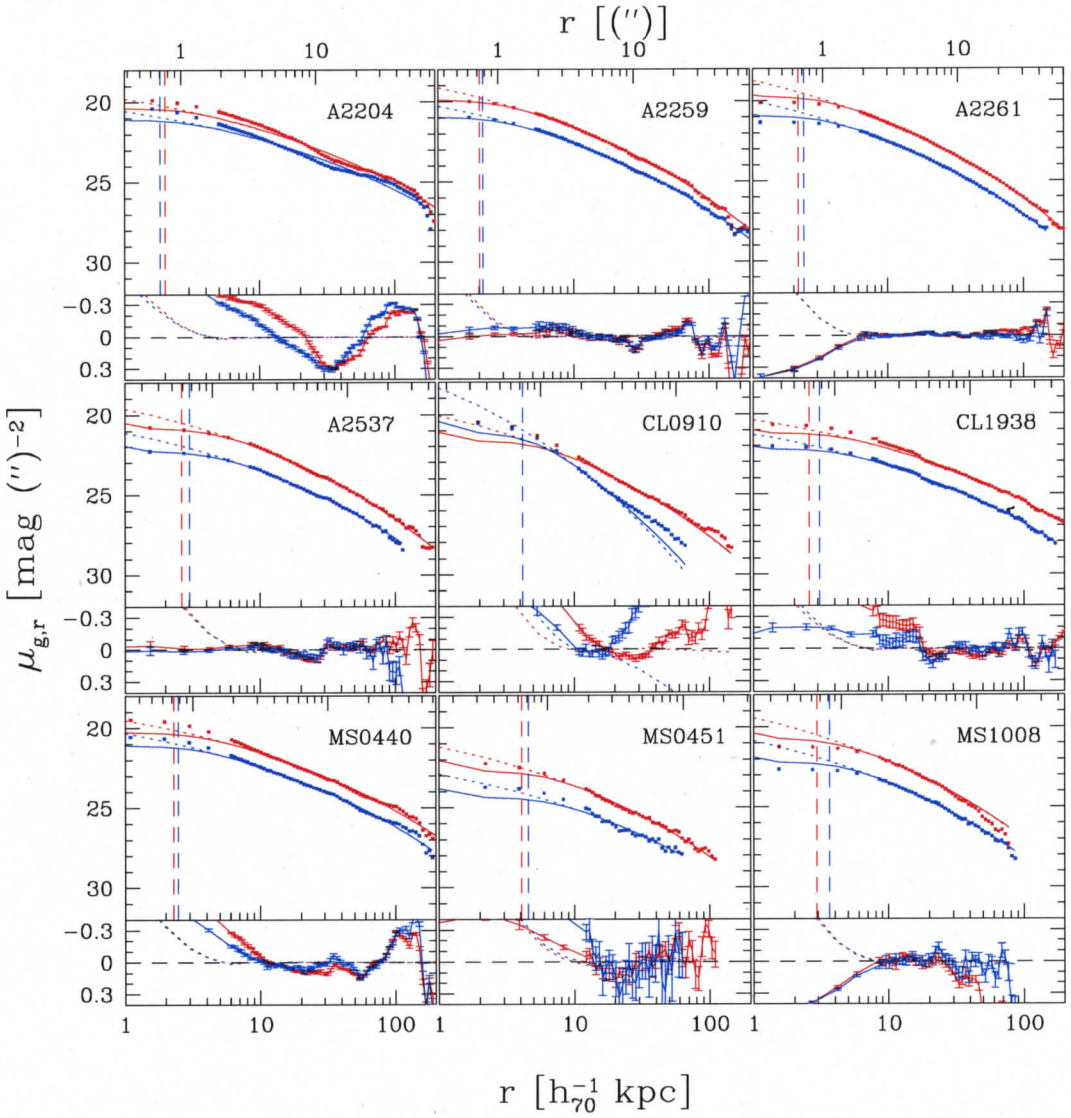

Figure 5.3: Surface brightnesses in g' (blue) and r' (red) for BCGs in the sample. Points correspond to measured data while solid and dotted lines correspond to fitted $r^{1/4}$ models with and without PSF-convolution respectively. Vertical dashed lines denote the r_{fwhm} seeing limit of the derived moffat PSF. Residuals are shown along the bottom with dotted lines showing the difference between fits with and without PSF-convolution and solid lines with error bars showing the difference between PSF-convolved models and the data. The top axis shows the corresponding radii in arcseconds

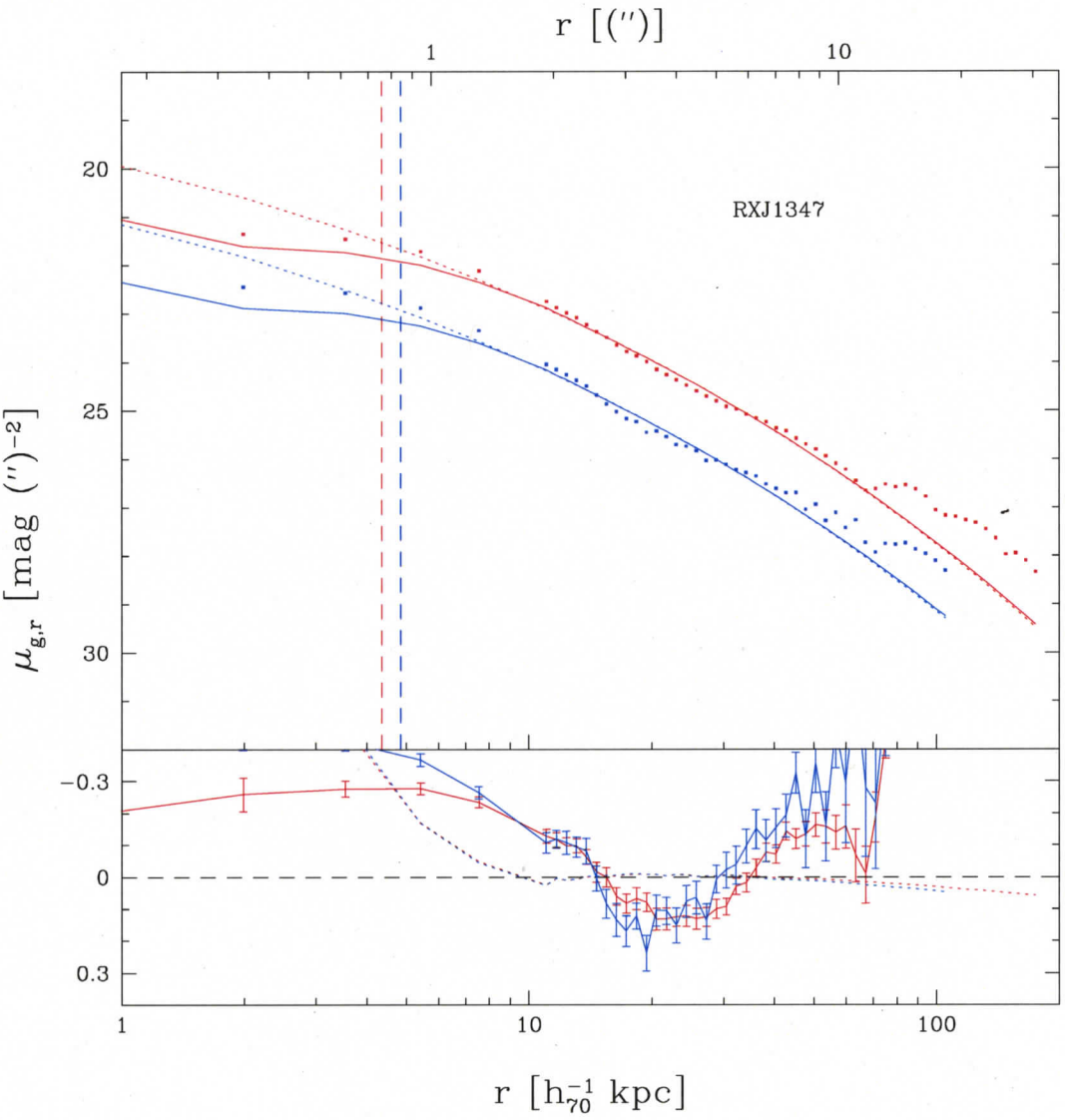

Figure 5.4: Surface brightnesses in g' (blue) and r' (red) for BCGs in the sample. Points correspond to measured data while solid and dotted lines correspond to fitted $r^{1/4}$ models with and without PSF-convolution respectively. Vertical dashed lines denote the r_{fwhm} seeing limit of the derived moffat PSF. Residuals are shown along the bottom with dotted lines showing the difference between fits with and without PSF-convolution and solid lines with error bars showing the difference between PSF-convolved models and the data. The top axis shows the corresponding radii in arcseconds

cularly symmetric profile on an object which is intrinsically elliptical. This problem occurs wherever large portions of the BCG major axis is be masked out. The flux along the major axis is then no longer able to contribute to that particular radial bin and the surface brightness is driven towards the value more representative of surface brightness along the minor axis. The impact of this effect is most noticeable for those objects which are highly elliptical (CL1938+54) and also in the case where both sides along the major axis are masked at the same distance from the object center.

For many objects we observe an excess over the assumed $r^{1/4}$ surface brightness profiles. Excess flux at large radii in BCG surface brightness profiles has been observed by several studies (Schombert 1987, Gonzalez et al. 2005, Zibetti et al. 2005, Patel et al. 2006). The large radius excess is generally understood to be a combination of the cD galaxy envelope, light from intracluster stars (ICS) which are unbound from any one particular galaxy, some light from the faint wings of other cluster member galaxies that have not been fully excluded by the masking or subtraction procedure plus any error in the background subtraction routine during the reduction procedure. In the most extreme examples of deviation from $r^{1/4}$ at large radius there is an obvious kink in the profile and a significant increase in the residual (eg. Abell 2204). In such cases the need for using an $r^{1/n}$ Sersic profile or including a second $r^{1/4}$ component in modeling surface brightness is obvious. For those BCGs in our sample which do display a strong signature of ICS the derived BCG model parameters are expected to be in error. In such cases however, the best fit parameters still allow for a useful characterization of the BCG/ICS system but one should be careful when trying to interpret their physical meaning.

In some BCGs we also see an excess from our simple $r^{1/4}$ model at small radii. These deviations tend to begin at 20 to 40 $h_{70}^{-1}kpc$, continuing inward and are easy to see by looking at the residual profiles (eg. Abell 1234, Abell 1835, CL0910). In the case of CL0910 this deviation is so strong that despite our attempts to avoid giving

too much weight the inner component the g' fit is still drawn to the small radius excess. We highlight here five systems that share this property (3C295, Abell 1835, Abell 2204, CL0910, MS0451 and RXJ1347). Another common feature of these five systems is that they host BCGs with particularly blue cores. We do not believe that this difference is due to an error in the PSF modeling because the deviation can often be seen well beyond the seeing-disk limit where the effect of the PSF on the profile is expected to be negligible. In addition, from the residuals we can see that the deviation from $r^{1/4}$ typically continues well beyond the radius at which the PSF-convolved model differs from the non-PSF-convolved version. One possible explanation for the deviation from $r^{1/4}$ is that BCGs may actually have more general Sersic profiles ($r^{1/n}$). In this case the variation in the parameter n may cause the observed surface brightness profile to rise flatter or sharper than a simple $r^{1/4}$ dependence. This would not explain however the abnormally blue central regions seen in the color gradients of many of these deviant systems (see section 5.2). A more probable explanation is that in some BCGs there exists an inner population of stars that have a separate origin and formation history than the remaining majority of the BCGs' stellar constituents. In this scenario, a difference in the inner profiles of BCGs could reflect a wide range in the influence of non-gravitational feedback processes (eg. AGN output, gas cooling, entropy distribution mechanisms) present during the formation of these rare galaxies. If this is indeed the case, we should expect that the some of the global and structural properties of BCGs are directly dependent upon those of their host clusters (eg. cluster temperature and entropy profiles, X-ray luminosity, etc.).

5.2 Color Profiles

The variation of galaxy color across the range in hubble classification reflects a change in the spectral types of their constituent stars. Early type galaxies are pre-

sumed to have had little recent star formation and so most of their stars at the high mass end have long since perished and the color of these galaxies is correspondingly red. In contrast, late type galaxies such as spirals and irregulars continue to form stars and are dominated by the light from massive, blue O and B type stars. If we consider only early type galaxies we may assume that the stellar populations are constant. Most of the change in color is then attributed to either varying age or metallicity representative of the stars in these galaxies. In this section we examine the colors of BCGs in the CCCP sample with the effects of spectral type, age and metallicity in consideration.

The figures 5.5 through 5.8 show the color profiles (g'-r') for the sample BCGs. As before, the vertical dashed lines denote the r_{fwhm} seeing limits of the derived r' (red) and g' (blue) moffat PSFs. Points with error bars indicate the measured data and solid lines show the difference (g'-r') for the $r^{1/4}$ model fits to the surface brightness distribution. Note that even though this is not a direct fit to the color profile the difference between the individual fits to the r' and g' data frames thread the color data quite well in most cases.

A few of the color profiles are observed to have remarkably steep color gradients at large radius (Abell 223a, Abell 521, MS1008-12). In most cases this effect is caused by sharp fluctuation of the background that results from patching images from adjacent chips into a single mosaic. By examining the surface brightness profiles and their fit residuals for the objects that exhibit this behavior it is easy to see the where the background error begins to dominate. A more detailed background subtraction routine may help to alleviate this complication but overall it does not seriously affect the results presented here nor the conclusions that we draw from them. The background error in g' is typically larger than that seen in r' owing primarily to the better relative depth of the r' data as well as the fact that the BCG flux is inherently red in color which leads to higher relative contribution from BCG signal to the total signal (including background) in the r' data. Thus

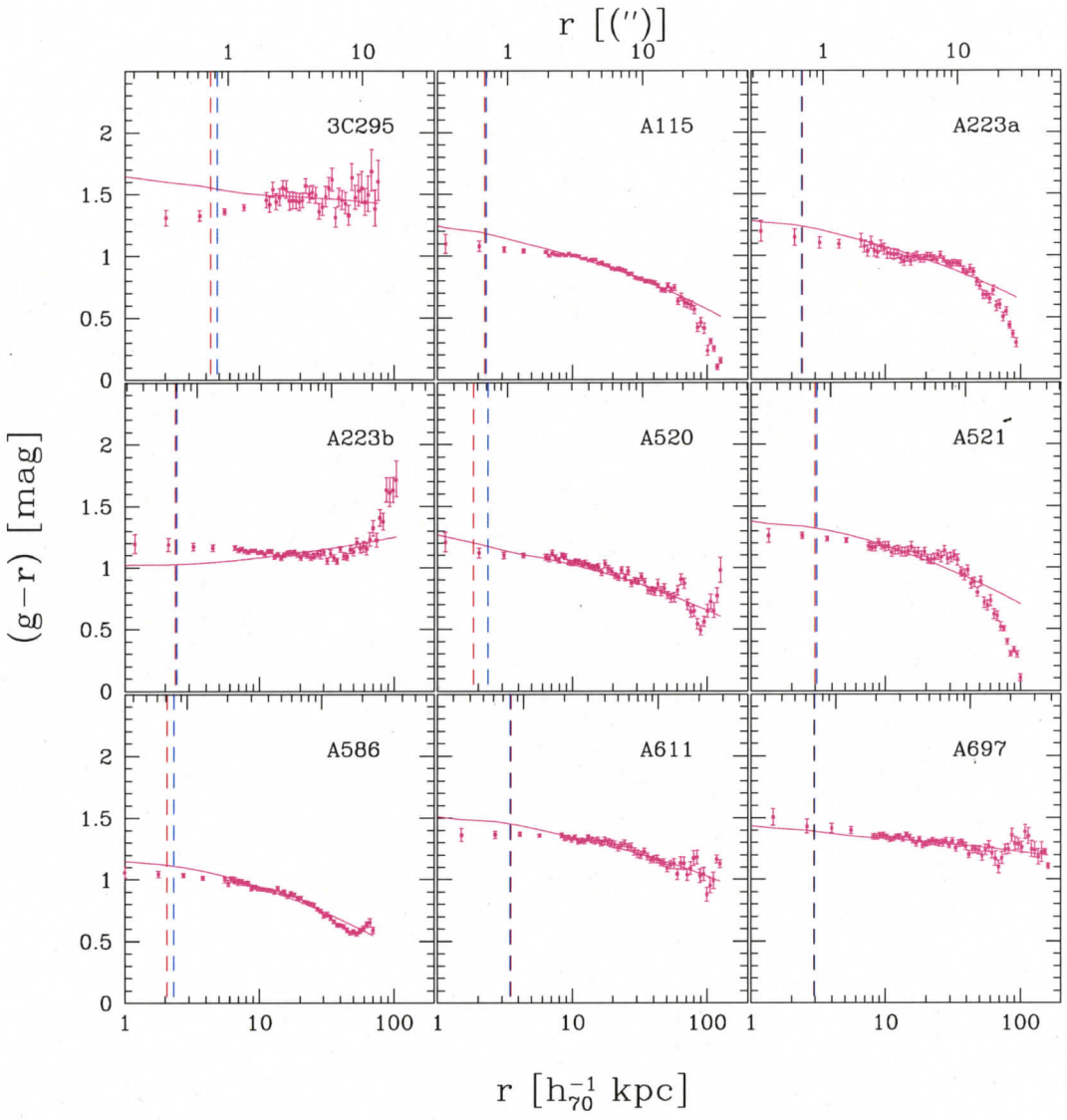

Figure 5.5: Color profiles in (g'-r') for BCGs in the CCCP sample. Points with error bars indicate measurements. Solid lines show the difference between best fit g' and r' $r^{1/4}$ models. Vertical dashed lines show the seeing limits r_{fwhm} for the g' data (blue) and r' data (red). The top axis shows the corresponding radii in arcseconds

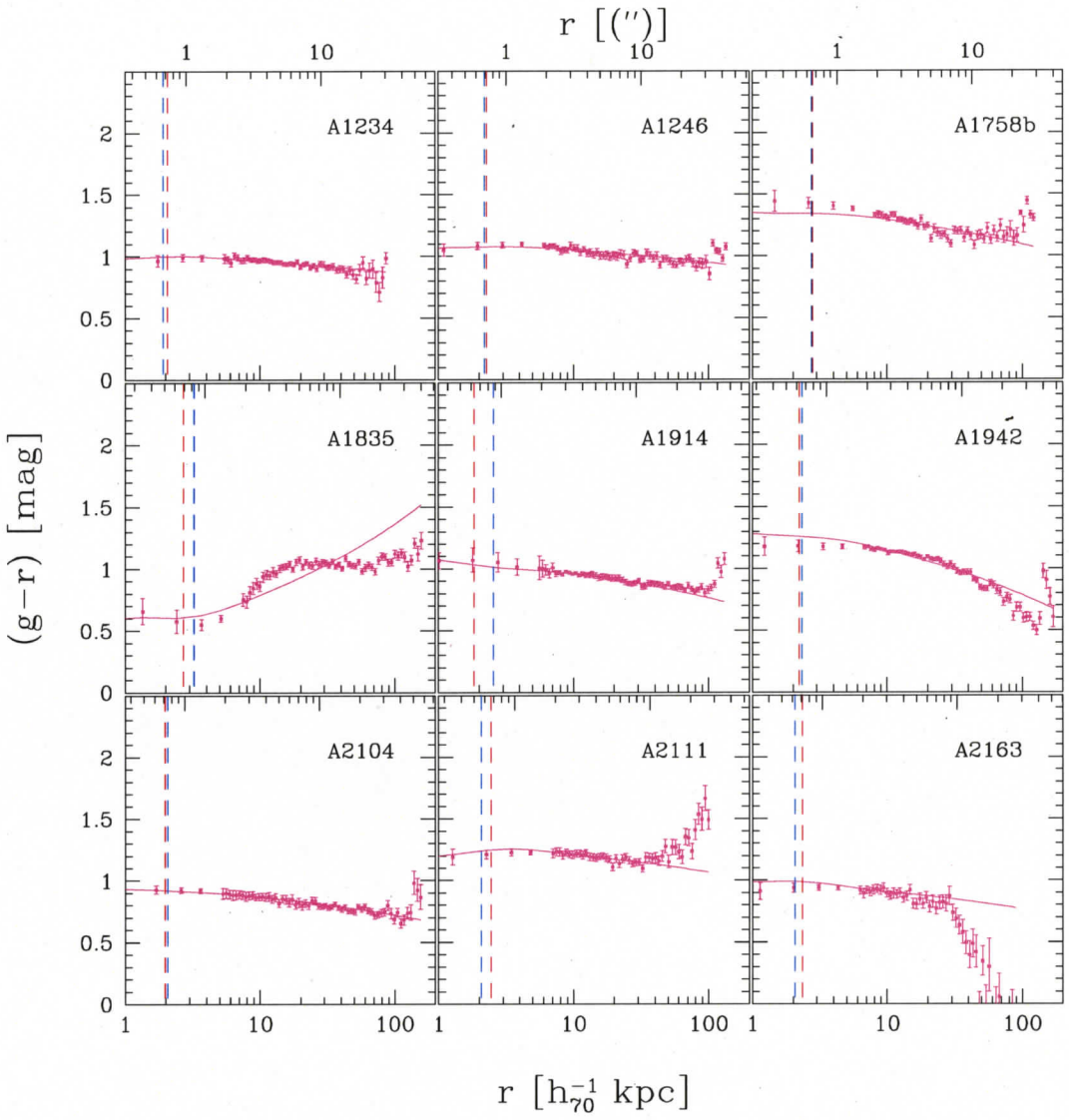

Figure 5.6: Color profiles in (g'-r') for BCGs in the CCCP sample. Points with error bars indicate measurements. Solid lines show the difference between best fit g' and r' $r^{1/4}$ models. Vertical dashed lines show the seeing limits r_{fwhm} for the g' data (blue) and r' data (red). The top axis shows the corresponding radii in arcseconds

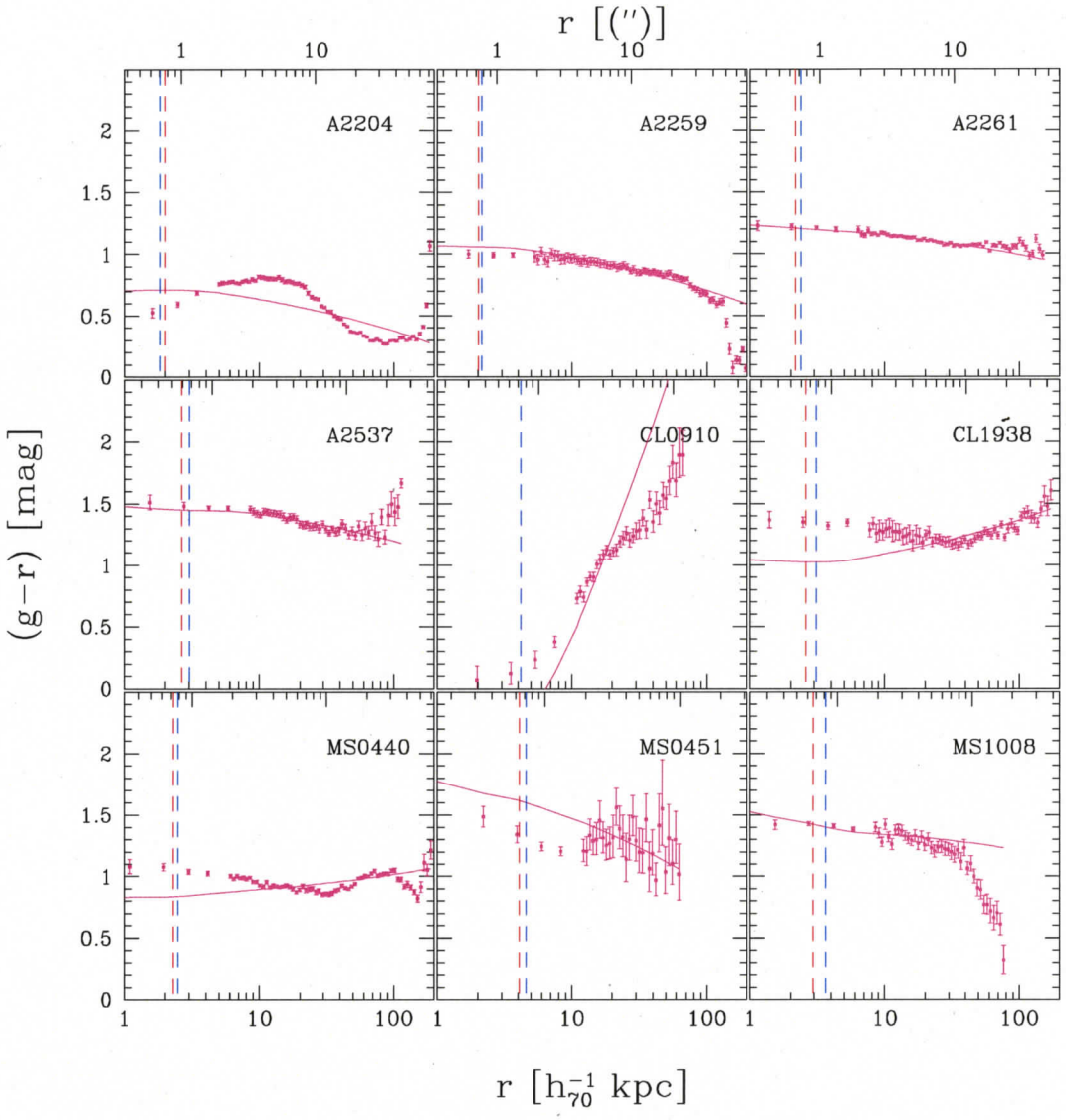

Figure 5.7: Color profiles in (g'-r') for BCGs in the CCCP sample. Points with error bars indicate measurements. Solid lines show the difference between best fit g' and r' $r^{1/4}$ models. Vertical dashed lines show the seeing limits r_{fwhm} for the g' data (blue) and r' data (red). The top axis shows the corresponding radii in arcseconds

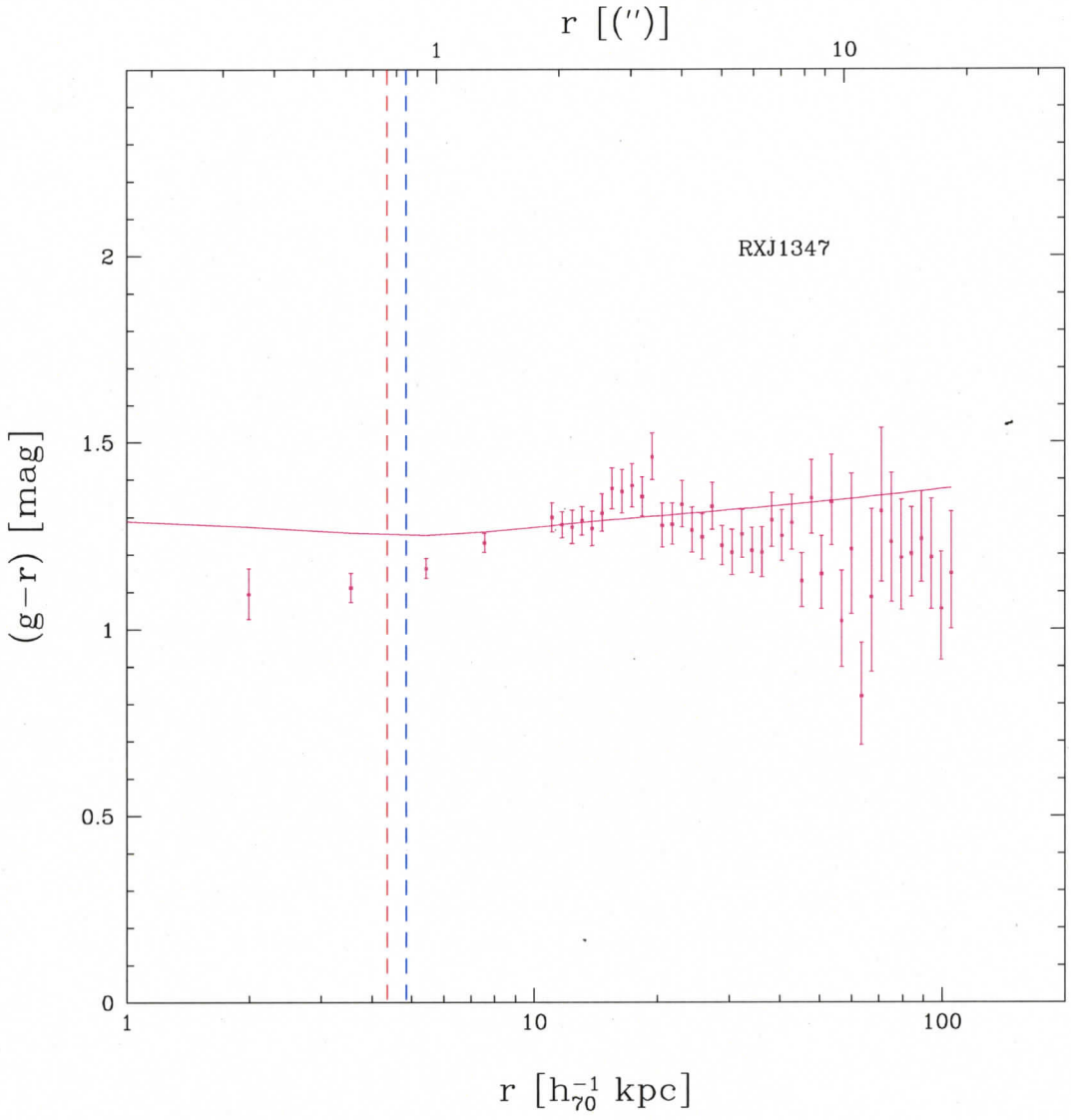

Figure 5.8: Color profiles in (g'-r') for BCGs in the CCCP sample. Points with error bars indicate measurements. Solid lines show the difference between best fit g' and r' $r^{1/4}$ models. Vertical dashed lines show the seeing limits r_{fwhm} for the g' data (blue) and r' data (red). The top axis shows the corresponding radii in arcseconds

anywhere that the error in the background may influence our overall conclusions (eg. Kormendy relation) we are careful to use the r' data only.

The basic trend in (g'-r') color of the BCGs in our sample is that they are all quite flat but become gradually bluer as we look outward from the center. This behavior is exactly what we should expect for an age/metallicity increase toward the BCG/cluster center. For some BCGs however, we see a turnover in (g'-r') color in their innermost regions. This turnover in color profile is such that color becomes increasingly blue with decreasing radius. Some of the BCGs in our sample exhibit quite blue cores. For these objects the turnover is fairly abrupt. The most extreme cases seem to be found in the more exotic host clusters. Abell 1835 and Abell 2204 both have large positive values of d(g'-r')/dlog(r) in their BCG's central regions. The ICM of each of these systems has a central temperature gradient characteristic of a cool-core clusters as derived from X-ray surface brightness modeling (Bonamente et al. 2005). We find evidence from previous work that both of these systems are hosts of line emission in their central regions and from various emission line diagnostics both are also confirmed host of recent star formation (Crawford et al. 1999, Wilman et al. 2006). Three other BCGs that show similar trends in their color profiles are: the BCG in RXJ1347 (ie., the brightest known cluster in X-ray (Schindler et al. 1995)), the BCG of 3C295 which shows visible signs of strong AGN activity in X-ray and radio as well as signs of massive amounts of star formation (Harris et al. 2000, Thimm et al. 1994), and that of CL0910 which is identified as a hyper-luminous Infrared galaxy (HLIRG; $L_{ir} > 10^{13} L_{\odot}$) and the brightest infrared source in a large sky-coverage, position matched sample of IRAS and SDSS DR3 catalogues containing 4248 infrared luminous galaxies (Goto et al. 2005).

5.3 Red Sequences

Galaxy color-magnitude diagrams provide useful diagnostics of galaxy formation and evolution in clusters. Red and blue galaxies segregate themselves from each other in these diagrams and form highly recognizable features that corresponding to evolutionary trends. These features are so recognizable that they can be employed as powerful tools for identifying clusters and major cluster surveys are carried out using exploiting this technique (Gladders and Yee 2005). Despite its obvious successes in leading to a general picture of galaxy evolution in clusters, the galaxy color-magnitude diagram still leaves us with important unanswered questions. Exact details of the physical processes that carry individual galaxies from one region of the diagram to another, as well as the stage in cluster evolution that its features become established are not fully understood. The following examines the color magnitude diagrams of the CCCP clusters and the position of the BCGs within these diagrams.

In figures 5.9 and 5.10 we show the observed color magnitude diagrams in (g'-r') versus r' for eight of the clusters in our sample (uncorrected for galactic extinction and redshift effects). The circles highlight the positions of the BCGs in each of the color-magnitude diagrams. These eight clusters illustrate the differences that can exist in red sequences and respective BCG positions from cluster to cluster. In each of the diagrams it is possible to identify both the red sequence and blue cloud cluster components. The majority of the CCCP clusters display red sequence BCG positions quite similar to those in figure 5.9 and these object fit well within the standard picture of BCGs construction through purely dissipationless merger events. It is also possible to see the redshift and metallicity effects on the and ($g' - r'$) intercept and slope of the red sequence (Gladders et al. 1998). In figure 5.10 we show some major exceptions (Abell 1835, Abell 2204, CL0910 and RXJ1347) which all contain BCGs that lie away from the tip of the red sequence. The BCGs in these clusters are also those that show strong central color enhancements toward the blue

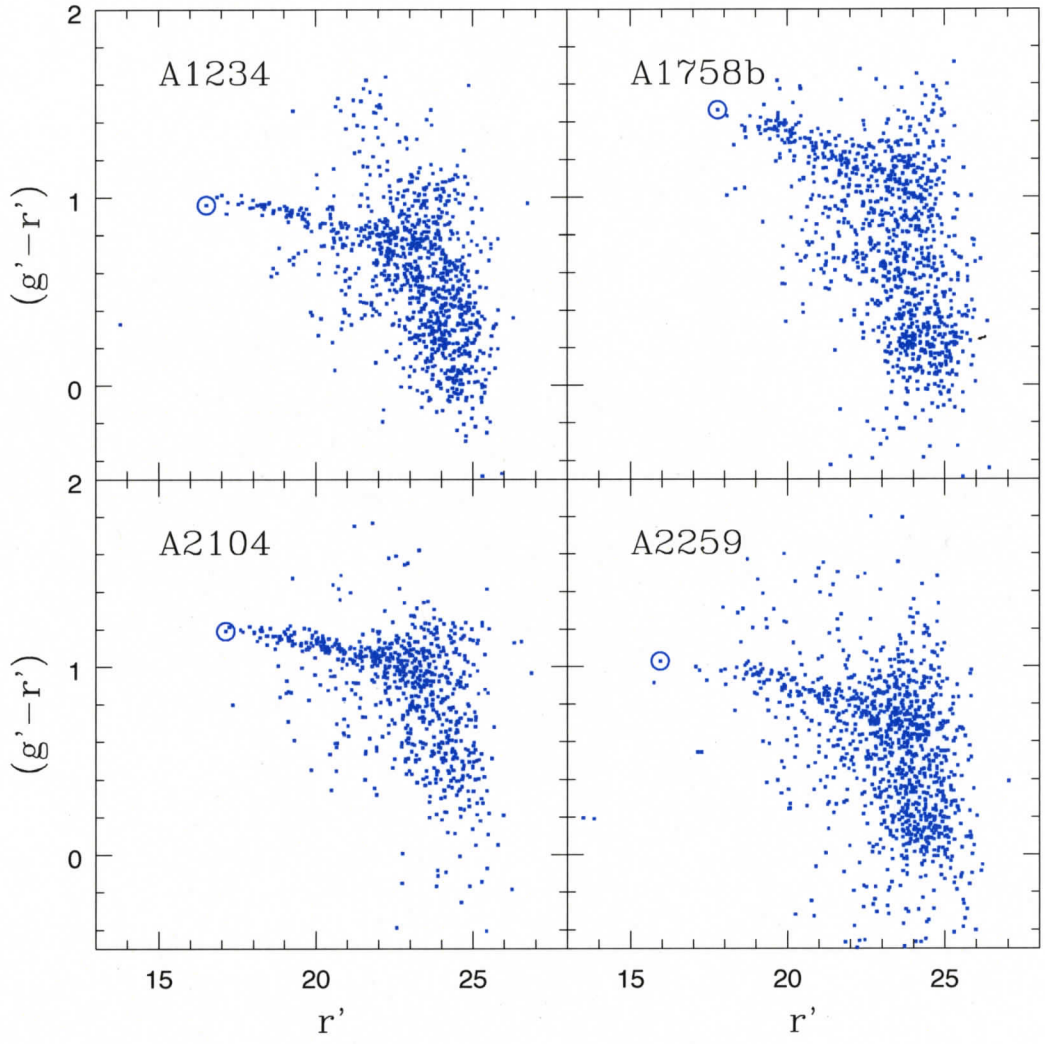

Figure 5.9: Four examples of typical color-magnitude diagrams in (g'-r') versus r' for clusters in the CCCP. Red sequences are clearly visible in all of the diagrams. In each diagram the location of the BCG is circled for emphasis. Note the BCG lies at the tip of the host cluster's red sequence in these systems.

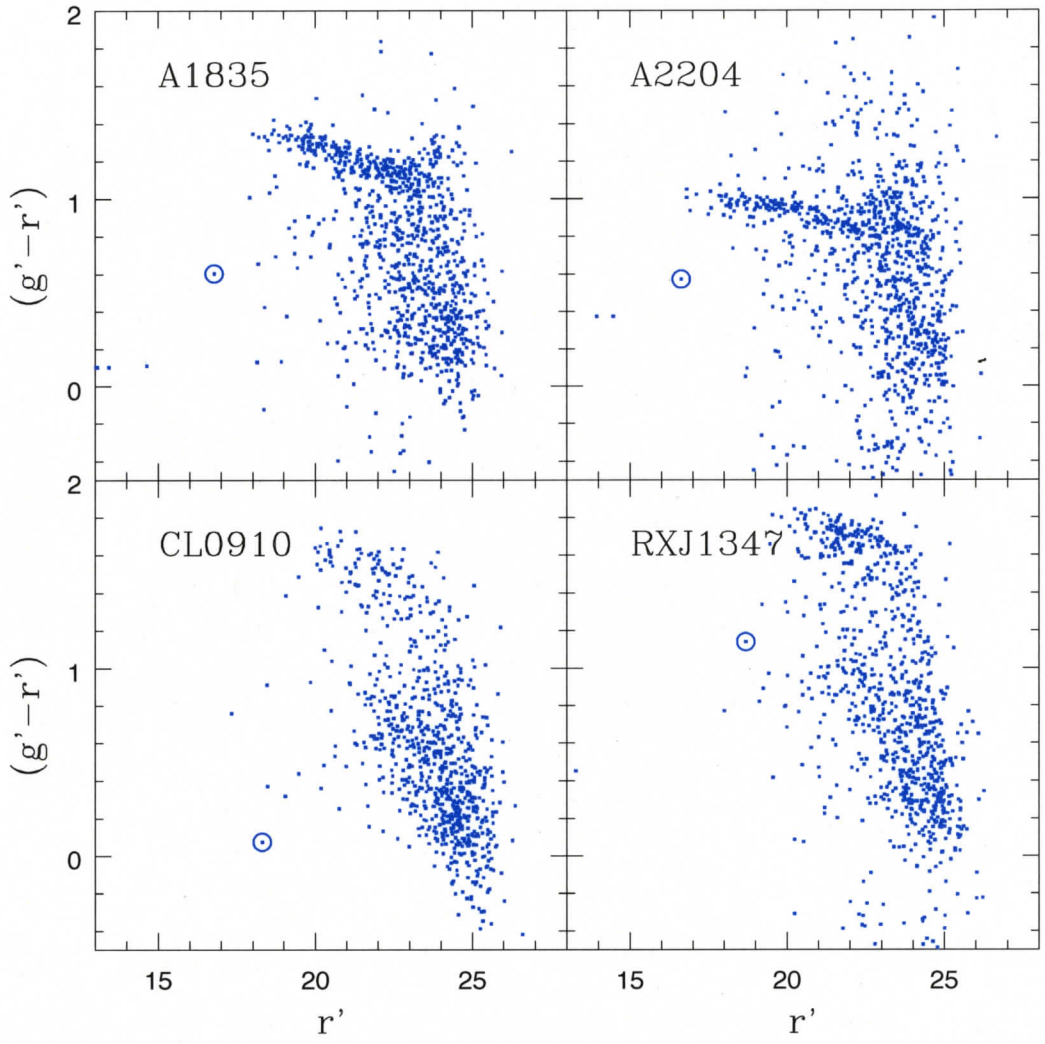

Figure 5.10: Four examples of color-magnitude diagrams in (g'-r') versus r' for clusters in the CCCP that contain blue core BCGs. Red sequences are clearly visible in all of the diagrams. In each diagram the location of the BCG is circled for emphasis. Note the BCG lies away from the host cluster red sequence in three cases.

in their (g'-r') profiles (see section 5.2). We interpret the blueward offset of the BCGs as evidence of concentrated star formation in the cores of these systems. The red sequence color offset for these BCGs is not too surprising given the sensitivity to the inner profiles of the aperture-colors used in constructing the color-magnitude diagrams. It is nonetheless interesting however, as this observation must be explained in the context of BCG and cluster formation/evolution models and may be used to identify potential star-forming systems with simple photometric techniques that do not require detailed resolution of the color profile.

The formation of both a red sequence and blue cloud can be understood in the context of a quenching model of galaxy formation (Martin et al. 2005, Harker et al. 2006, Cimatti et al. 2006, Bower et al. 2006, Cooper et al. 2006). In the quenching model it is the total reservoir of cold gas in a merger that determines the position of the resulting galaxy on the color magnitude diagram. Wet mergers, associated with a large supply of cold gas, create merger-induced starbursting systems. Wet mergers are believed to produce the galaxies with young stellar populations that occupy the blue cloud region of the galaxy color-magnitude diagram. Dry mergers occur when two or more galaxies merge and there is a lack of cold gas. No new stars are formed in this scenario and the merger results in a luminous, red galaxy that lies on the red sequence in the galaxy color-magnitude diagram. Galaxies are believed to transit from the blue cloud to the red sequence by the repeated process of merging and the resulting depletion of the available cold gas supply either by the formation of new stars or mass accretion onto the central super-massive black hole. Once on the red sequence a galaxy should only ever experience dry mergers unless its cold gas reservoir is somehow replenished. The BCGs that lie off the red sequence in the CCCP sample must contain some amount of cold gas. Because BCGs predominantly form from mergers of galaxies that are already on the red sequence there must be some mechanism that is replenishing the cold gas supplies within these systems. A possible mechanism for cold gas replenishment in these systems is the cooling of the

Intra-Cluster/Galactic Medium (ICM/IGM). Due to the high X-ray luminosities of the clusters in the CCCP sample and the ρ^2 dependence of the gas cooling rate:

$$\Lambda \propto \rho^2/T^n \tag{5.1}$$

where $-1/2 \leq n \leq 1/2$, we might expect to find systems which show some signature of cold gas replenishment taking place in some of the clusters examined (see sections 6.3 and 6.4).

5.4 Kormendy Relation

The Kormendy relation (Kormendy 1977) describes a tight correlation between μ_e and r_e for elliptical galaxies. This empirical relation was first observed to hold for local ellipticals and has since been applied to a large range of spheroid galaxy types. The Kormendy relation has since been shown to be a projection of the more general Fundamental Plane (FP) (Djorgovski and Davis 1987, Dressler et al. 1987) which describes a 2-dimensional manifold in $(\sigma_0,\langle\mu\rangle_e,r_e)$ space. The FP and its various projections are well defined scaling relations for the observable properties of elliptical galaxies that provide highly useful tests of galaxy formation models. Previous studies have sought to construct the Kormendy relation for BCGs/ICS. Gonzalez et al. 2005 and Zaritsky et al. 2006 both find some evidence for a departure from the Kormendy relation for local ellipticals ($\mu_e = 3.02 log r_e + 19.74\mu$) at the high r_e end equating to a tilt of the Fundamental Plane.

The Kormendy relation for the CCCP BCGs is shown in figure 5.11. Surface brightness μ_e is corrected for the effects of cosmological dimming, and galactic extinction. We then convert to rest-frame Johnson V magnitude using an elliptical galaxy template spectrum (Wu & Weedman). In this analysis we consider only the model parameters from the fits to the r' data as their V magnitude conversions are less affected by the assumption of a particular spectral template. The CCCP

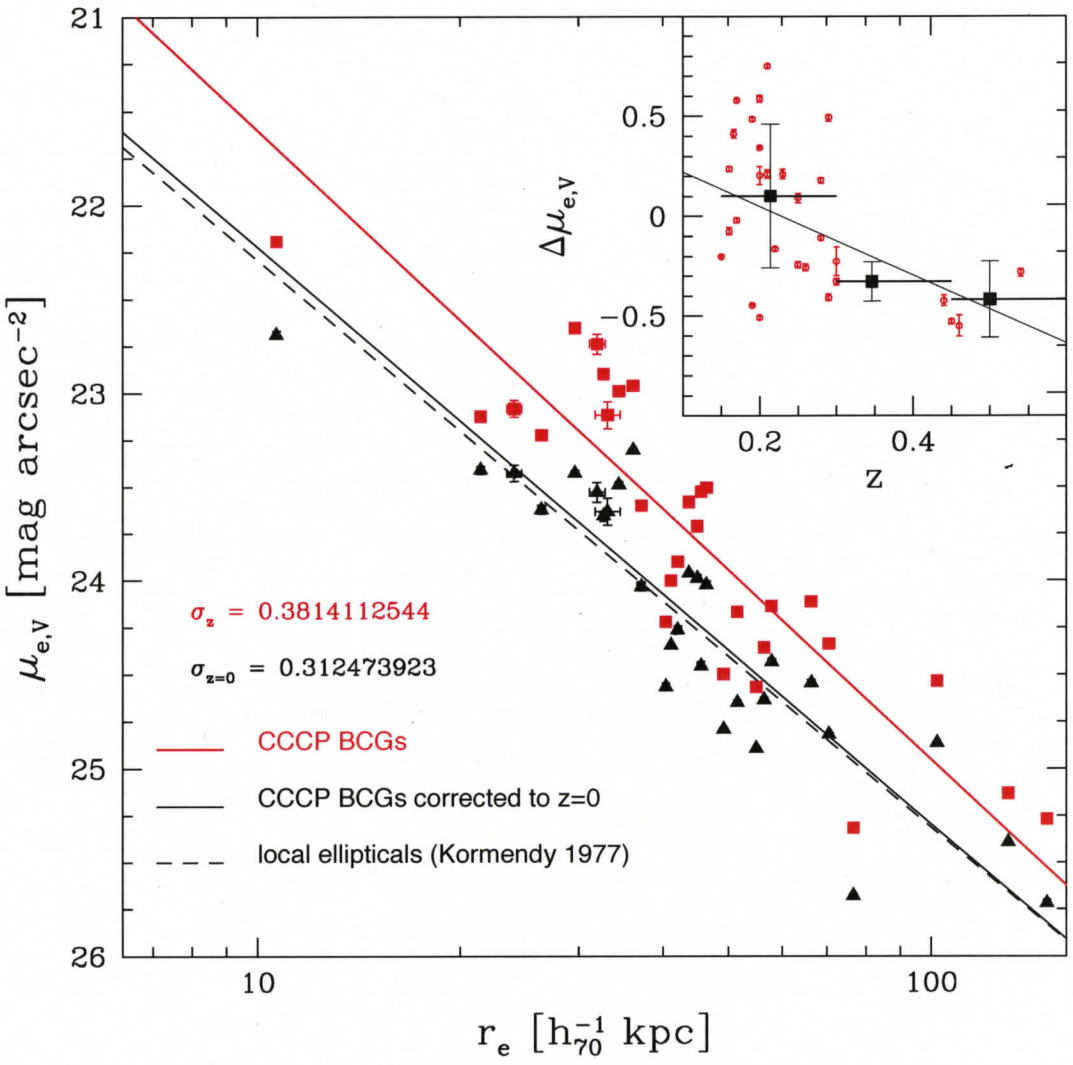

Figure 5.11: Kormendy Relation for the CCCP BCGs. The data has been corrected for cosmological dimming and converted to rest-frame V magnitude. Red squares denote the best fit $r^{1/4}$ model parameters and black triangles show their corresponding values after correcting for surface brightness evolution. Error bars show the 1 σ fitting uncertainties but are typically smaller than the symbol size. The thin, dashed, black line shows the extrapolated Kormendy relation for local elllipticals (Kormendy 1977). The thick red line shows the mean relation for the CCCP BCGs and the thin, solid black line shows the mean relation for CCCP BCGs after correction for surface brightness evolution. The upper right panel shows the residual in effective surface brightness as a function of redshift. RMS scatter for BCGs before and after correction for surface brightness evolution are shown as σ_z and $\sigma_{z=0}$ respectively, notice the reduced scatter in the corrected data.

BCGs are plotted in red squares and the thick, red line shows the mean relation of the sample as determined by a simple least-squares fitting procedure. We also plot the difference in μ_e from the mean as $\Delta\mu_{e,V}$ against redshift in the inset of figure 5.11. The data is then binned in redshift (horizontal bars) and the variance is determined in each bin (vertical error bars). A least squares fit to the binned data yields a variation in surface brightness from the sample mean of:

$$\Delta\mu_{e,V} = -1.72 \pm 0.70z + 0.39 \pm 0.35 \tag{5.2}$$

This relation is shown in the inset as a solid line. The qualitative trend is that of an increase in BCG brightness with redshift. This passive evolutionary behavior is expected for massive systems that formed the majority of their stellar content at early cosmic times. If we further make the assumption that BCGs are homologous one can attribute the trend in surface brightness evolution to a an increase in the mass-to-light ratio M/L with time. Equation 5.2 then equates to an evolution in M/L of:

$$\Delta logM/L_V = -0.69 \pm 0.28\Delta z \tag{5.3}$$

van Dokkum and Franx (1998) obtain an M/L evolution of $\Delta logM/L_B \cong -0.55 \pm 0.05\Delta z$ for a ΛCDM cosmology which they show is well fit by a simple stellar populations model with a realistic Salpeter IMF ($x = 2.35$) and formation epoch of $1 \leq z \leq 2$ for cluster ellipticals.

Using the slope of the relation 5.2 we apply an evolution correction to the CCCP BCGs in order to compare their redshift zero counterparts on equal footing; the corrected data are shown in black triangles. While there is still a large amount of scatter in the evolution-corrected data, the σ (rms) is reduced by about 20% to a value of $\sigma_{(z=0)} = 0.31$ and is consistent with the scatter the local elliptical Kormendy relation of $\sigma_{local} = 0.28$ (Kormendy 1977). We show the change in σ values in the upper left corner of figure 5.11 and note that much of the remaining

scatter is intrinsically due to variation in velocity dispersion from one BCG to another that is not accounted for in the Kormendy relation. The thin, solid, black line shows the mean relation of the evolution-corrected BCGs and the thin, dashed, black line shows the extrapolated Kormendy relation for local ellipticals. There is no significant evidence for a difference in the Kormendy relation for the evolution-corrected BCGs and that of the local elliptical population.

5.5 Color Evolution

BCGs and other massive elliptical galaxies are thought be composed primarily of old stellar populations. These galaxies are constructed hierarchically from mergers of smaller systems. These small systems that are the progenitors of massive ellipticals must form their stars very early on and so by the time they are accreted onto the BCG they contribute large quantities of old stars and very little cold gas. The result is that massive stellar systems appear to have peaked in star-formation at early times. In contrast with massive ellipticals, less massive ellipticals and disk galaxies appear to have peaked in star-formation much later (Juneau et al. 2005). This top-down picture of the early formation of the stellar component in massive galaxies is often referred to as "downsizing" and sometimes termed "anti-hierarchical", although it has been shown to be compatible with ΛCDM galaxy formation models that incorporate AGN feedback (Bower et al. 2006).

The implication of a star-formation rate that peaked at early times for BCGs in the CCCP sample is that we should observe the slow passive evolution of an aging stellar populations in these systems. We expect to see an overall dimming of the surface brightness as the brightest stars are extinguished (see section 5.4) and a mostly constant color with a possible slight trend towards bluer color at increasing redshift.

Figure 5.12 shows the observed raw colors of the CCCP BCGs prior to k-

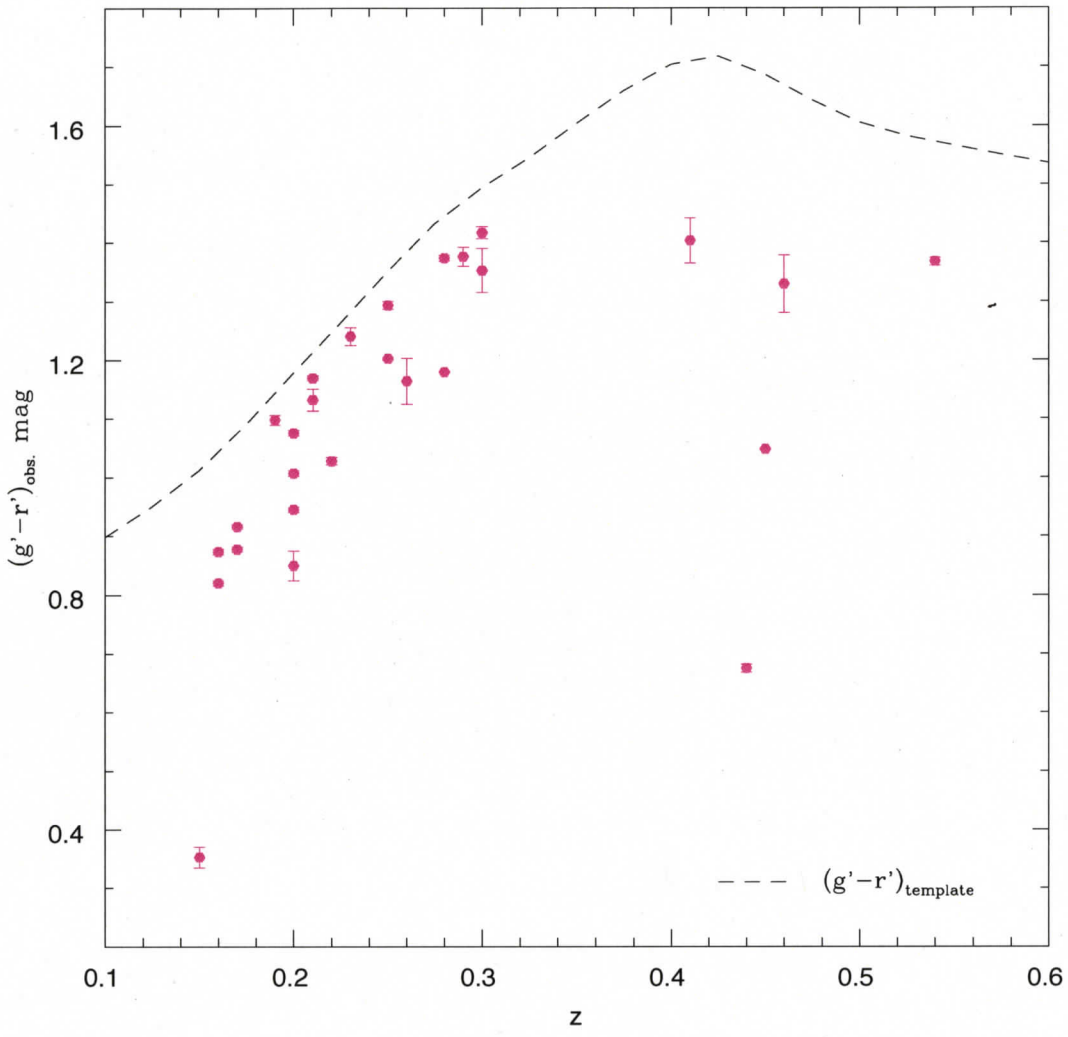

Figure 5.12: BCG integrated $(g'-r')$ color (raw) vs. redshift. Colors are integrated out to the effective radius in r'. The dashed line shows the color of the assumed spectral template.

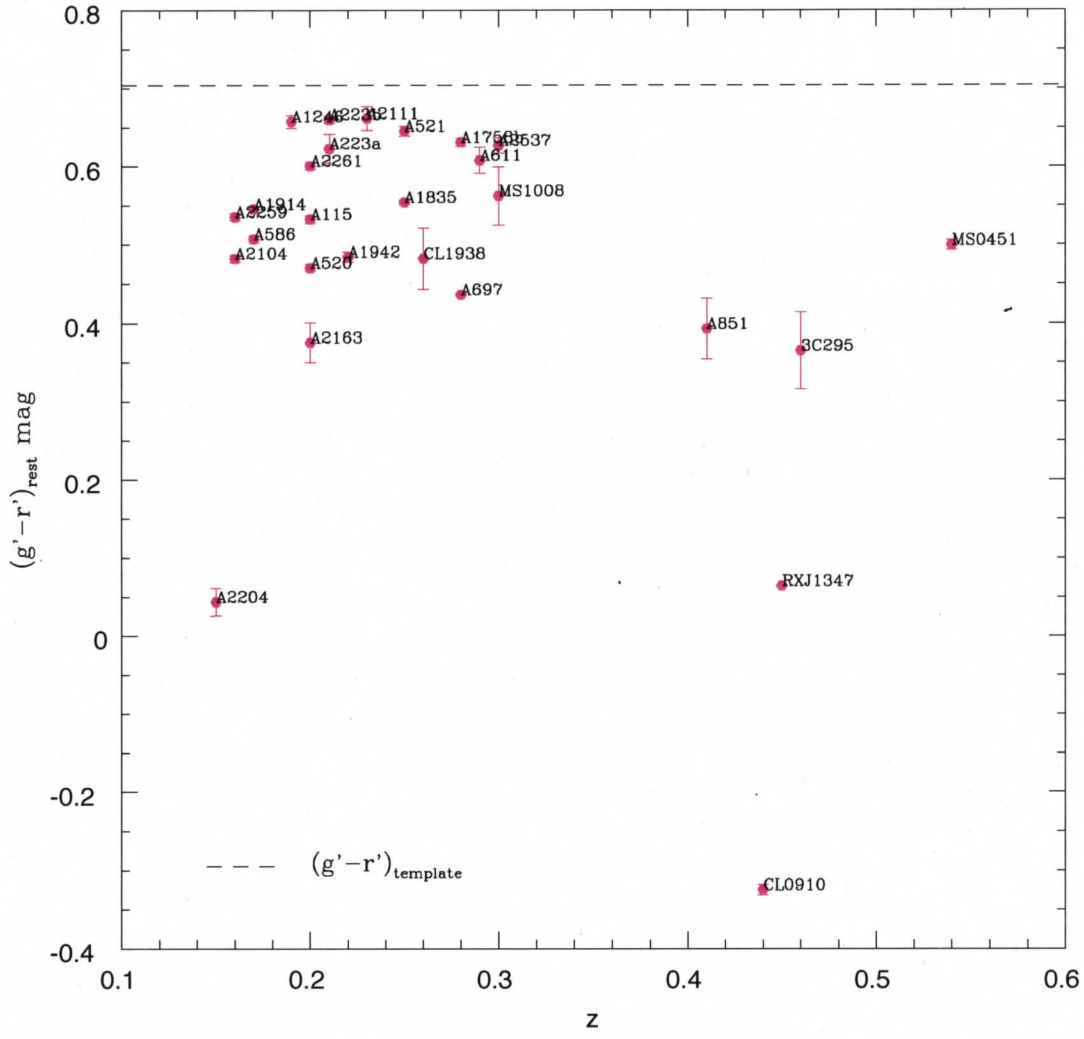

Figure 5.13: BCG integrated $(g' - r')$ color (k-corrected) vs. redshift. Colors are integrated out to the effective radius in r'. The dashed line shows the color of the assumed spectral template.

correction. The color shown here is the integrated color out to the effective radius measured in r' ($r_{e,r'}$). The dashed line in this figure represents the expected color obtained by redshifting the assumed template. The effect on $(g'-r')$ color of early-type galaxies with redshift is a steep reddening out to $z \sim 0.4$ as the g' and r' filters are shifted across the 4000 $\AA$ break, which then approaches a constant color at higher redshift where g' and r' fall shortward of the break. This property makes the $(g'-r')$ red-sequence a powerful redshift indicator in the range $0 \lesssim z \lesssim 0.4$ but not very good past $z \gtrsim 0.4$.

Figure 5.13 shows the evolution of CCCP BCG $(g'-r')$ color as a after applying the appropriate k-correction. The dashed horizontal line shows the rest-frame color of the assumed template. In both figure 5.12 and 5.13 there is an slight offset between the template color and the sample color such that the sample appears to be slightly more blue. This is not too surprising considering that the template represents a simple stellar population while it is obvious from variation seen in the color profiles in figures 5.5 through 5.8 that this is strictly not the case. The other notable feature of the sample colors in figures 5.12 and 5.13 is that for a particular redshift there is a range of observed color: $0.45 \lesssim (g'-r') \lesssim 0.65$. There are some outliers in color which those galaxies that contain blue cores. The most extreme outlier is CL0910+41 which has a remarkably blue k-corrected $(g'-r') \sim -0.3$. There may be a shallow decline towards bluer colors with increasing redshift, although small sample numbers at high redshift and uncertainty in the selection function make it difficult to comment on this conclusively. This effect could also be caused by assigning an incorrect template spectrum.

Chapter 6

Correlation with Host Cluster X-ray Properties

In hierarchical ΛCDM structure formation models, the growth of dense structures like clusters of galaxies proceeds by the accretion and merging of smaller structures such as groups and individual galaxies. These smaller structures fall into the cluster at velocities greater than the sound speed of the local medium, causing the gas in the infalling galaxies to become shock heated and stripped by the resulting ram pressure. Through the process of repeated merger events the cluster accumulates large amounts of hot gas with temperatures on the order of $T \sim 1-10$ keV. The gas, which is primarily Hydrogen, becomes an ionized plasma at these temperatures and cools mainly through free-free bremsstrahlung emission. As the ions scatter off one another in these interactions they emit X-ray photons causing galaxy clusters to appear as bright, extended X-ray sources on the sky. This convenient property of galaxy clusters allows astronomers to detect distant clusters, and with the help of some modeling, determine estimates of the cluster density, temperature and entropy structures as well as masses, sizes and dynamical states. The X-ray emission can tell a lot about the formation and evolution of galaxy clusters and can also be used to study cosmology.

The cluster X-ray emission has proved to be a wonderful tool for understanding the most massive structures in the universe but it has also unearthed a new complication. Detailed study of cluster X-ray properties reveals that our current

understanding of cluster physics is inadequate to describe the full range in observed X-ray properties. For example, the X-ray scaling relations for galaxy clusters like the $L_x - T_x$ and $M_x - T_x$ are known to exhibit intrinsic scatter that is not attributable to observational errors and is not accounted for in current semi-analytic or numerical models of cluster formation. In addition, self-similar models of cluster formation assuming no segregation of dark and gaseous matter yield a power law relation between L_x and T_x ($L_x = \beta T_x^{\alpha}$) with $\alpha = 2$ (Kaiser 1986; Navarro et al. 1995) while the observations indicate an $\alpha \sim 3$ (Mushotzky 1984; Edge & Stewart 1991; David et al. 1993; Fukazawa 1997). These differences between model predictions and observations suggest that non-gravitational feedback processes such as radiative cooling, AGN heating, stellar winds, conduction and convection are highly important are required to understand cluster formation and evolution. Investigation into the details of how these processes modify the structural properties of galaxy clusters is currently a booming branch of research in astronomy. One good way of searching for clues to the relative importance and behavior of these feedback processes is to look for the characteristic signatures of their effects in other observable wavelength bands. Because radiative cooling is most effective in the central regions of clusters where the ICM is densest, the cluster central galaxies that form in these unique environments may provide a powerful window on both cluster physics and galaxy formation.

In this chapter we seek to compare the optical properties of the BCGs in our sample with the X-ray properties of their host clusters. All of the systems in the CCCP sample have been observed with ASCA and table 6.1 outlines the X-ray data for the subset of clusters chosen from the CCCP for BCG analysis. Note that these systems span a range in redshift ($0.15 \lesssim z \lesssim 0.55$) and have X-ray temperatures $T_x \geq 5.0$ keV.

Table 6.1: Selected Clusters from the CCCP sample

Name	Redshift (z)	T_x (keV)	δT_x^+	δT_x^-
3C295	0.46	6.51	1.37	.99
Abell 115	0.20	6.45	.33	.31
Abell 223a	0.21	5.12	.63	.52
Abell 223b	0.21	5.44	1.16	.85
Abell 520	0.20	7.81	.74	.64
Abell 521	0.25	6.74	.50	.45
Abell 586	0.17	6.39	.72	.60
Abell 611	0.29	6.69	.51	.44
Abell 697	0.28	9.14	.60	.54
Abell 851	0.41	8.99	1.34	1.01
Abell 959	0.29	6.26	.93	.81
Abell 1246	0.19	6.04	.42	.37
Abell 1758b	0.279	7.95	.74	.62
Abell 1835	0.25	7.65	.33	.31
Abell 1914	0.171	9.48	.49	.45
Abell 1942	0.22	5.12	.71	.56
Abell 2104	0.16	9.31	.50	.47
Abell 2111	0.23	8.02	.95	.77
Abell 2163	0.20	12.12	.62	.57
Abell 2204	0.15	6.97	.18	.18
Abell 2259	0.16	5.32	.29	.27
Abell 2261	0.20	6.88	.47	.41
Abell 2537	0.30	6.08	.59	.49
CL0910+41	0.44	6.61	.63	.60
CL1938+54	0.26	7.52	.38	.37
MS0440+02	0.19	5.02	.61	.50
MS0451-03	0.54	8.62	1.54	1.21
MS1008-12	0.30	7.47	1.56	1.21
RXJ1347.5-1145	0.45	10.88	.73	.66

X-ray temperatures are taken from the ASCA cluster catalog of D. Horner 2001. Note: Abell 1234 is not part of the Horner 2001 sample and so it has been excluded from the following analysis.

6.1 Cooling and the L_x-T_x Relation

The correlation of X-ray luminosity (L_x) and temperature (T_x) for groups and clusters of galaxies has attracted much interest over the past decade. The scatter in this relation is substantial and cannot be reconciled purely by observational error. There is increasing evidence that this scatter is physical in origin and that the processes that give rise to this scatter are also responsible for the deviation in M-T_x as well as SZ correlations (Babul et al. 2002, McCarthy et al. 2003, Balogh et al. 2004, McCarthy et al. 2004). We are interested to know if the same processes that are believed to cause the scatter might also alter the observable properties of BCGs. One advantage of the CCCP sample is that it spans the full observed range of scatter in L_x-T_x and M-T_x which is a very useful property of any sample that aims to understand the physical differences between clusters and how these differences affect the cluster scaling relations.

McCarthy et al. 2004 demonstrated that models of cluster evolution that simultaneously incorporate radiative cooling along with a source of pre-heating are able to reproduce a significant amount of the observed scatter in the cluster L_x-T_x relation. The main observable effect of preheating in these models is to drive a cluster of a given mass towards lower X-ray luminosities by introducing an entropy floor to the cluster core which limits the central density and therefore L_x through the cooling function (see equation 5.1). The effect of radiative cooling in these models is to erase the entropy floor and produce dense, bright L_x cluster cores. These models have been compared to the data of Horner 2001 to show that known cool-core clusters lie on the high luminosity side of the L_x-T_x relation. In the following figures we compare the deviation of cluster L_x from the best fit L_x-T_x to various properties of BCG. The quantity $\Delta log(L_x/E(z)h_{70}^{-2}ergs^{-1})$ represents this deviation corrected for the change in cosmology and the evolution of the mean background density. We use this metric as a first-order proxy for the cooling state of a cluster.

6.2 The L_x-T_x relation for the CCCP clusters

Several previous studies have shown that the power-law index governing the scaling between L_x and T_x varies with the particular range of temperatures and luminosities of the observed sample. Horner (2001) finds $L_{bol} \propto T_x^{3.49}$ when fitting to all clusters and groups in the range $10^{42}h_{50}^{-2}ergs^{-1} \leq L_{bol} \leq 2 \times 10^{46}h_{50}^{-2}ergs^{-1}$. When the fit is restricted to those objects with $L_{bol} > 2 \times 10^{44}h_{50}^{-2}ergs^{-1}$ Horner (2001) finds the relationship flattens to $L_{bol} \propto T_x^{2.84}$. There also appears to be some variation in the power-law index α within different sub-samples of the cluster population. Arnaud & Evrard (1999) find $\alpha = 2.88 \pm 0.15$ for "weak" cooling flows ($\dot{M} \leq 100M\odot$). Markevitch (1998) notes that excluding the inner $50h^{-1}kpc$ when calculating the luminosities and temperatures of clusters (drawn mainly from the Ebeling et al. 1996) sample leads to a steeper power-law index ($\alpha = 2.64 \pm 0.27$) and a decrease in the overall scatter of $\Delta\sigma_{logL} = 0.077$ which corresponds to a 43% reduction. These various works demonstrate the possible variation in the L_x-T_x relation within different sub-samples of the cluster/group population. Keeping these differences in mind, we wish to compare the BCG optical properties with the residual from the L_x-T_x relation ($\Delta log(L_x/E(z))$) and so we must be careful when selecting the relation that is used for this comparison.

A linear least squares fit in $log(L_x/E(z))$ and $log(T_x)$ is performed on the Horner (2001) ASCA cluster catalogue data from which the CCCP sample is drawn.

$$log(L_x/E(z)) = \alpha log(T_x) + \beta \tag{6.1}$$

We restrict this fit to only those clusters that pass the selection criteria of the full CCCP sample; $T_x \geq 5$ keV and $0.15 \leq z \leq 0.55$. We assume that a given cluster's deviation from the mean L_x-T_x relation is representative of its deviation from a "typical" cluster in terms of the dynamical state of its ICM. In an attempt to characterize the "typical" cluster we use a sigma-rejection procedure that prevents

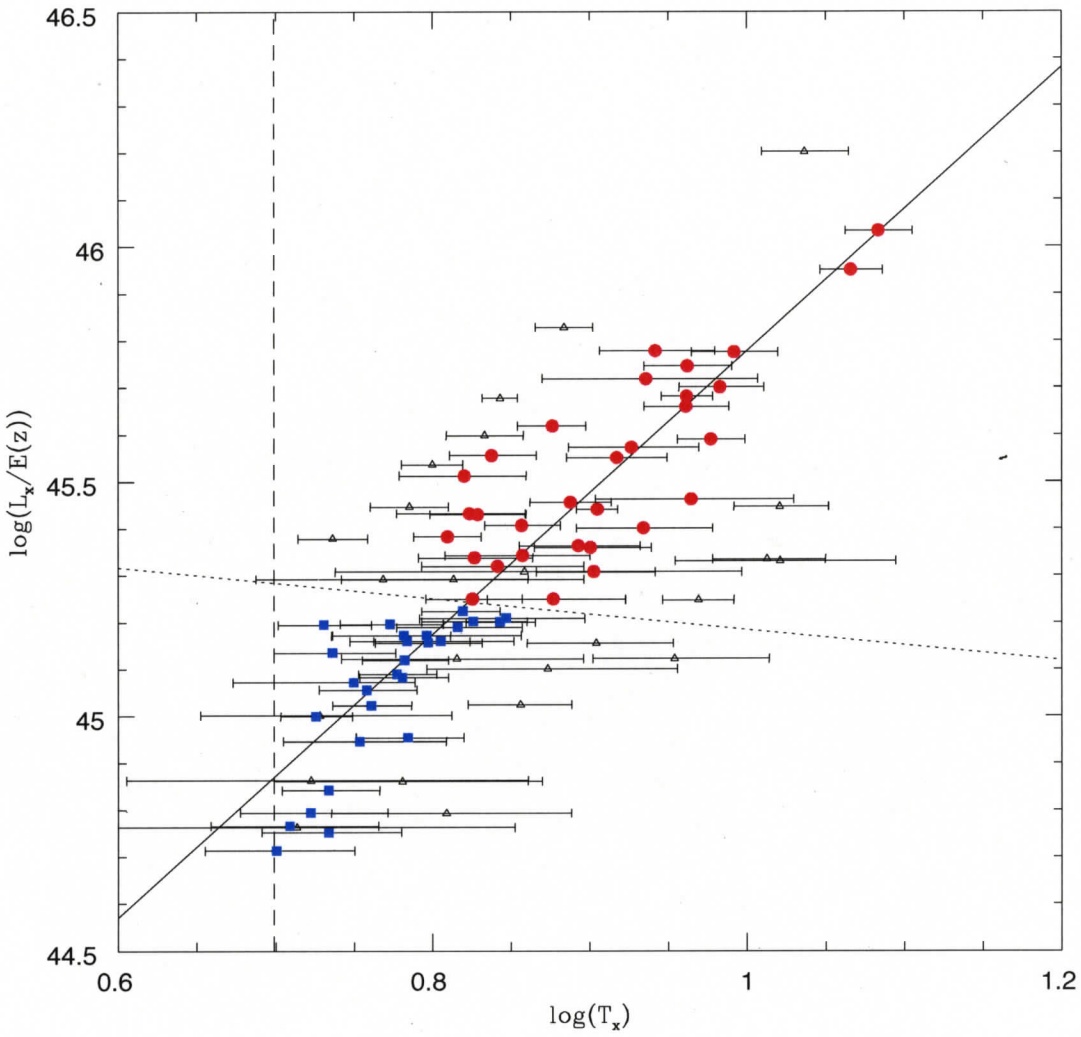

Figure 6.1: L_x-T_x relation for CCCP clusters. Data is taken from the ASCA cluster catalogue of Horner (2001) for all clusters satisfying the CCCP selection criteria. A sigma-rejection method has been employed to obtain a fit that is representative of a "typical" cluster's properties. The vertical dashed line shows the sample selection cut in temperature. The dotted line show the limit of the potential 2σ bias (see discussion above). Open black triangles show the data that was rejected in the final fit. Solid red circles and blue squares show the data used in the final fit above and below the 2σ bias respectively.

the fit from being influenced by the most extreme systems. Throughout the fitting procedure we exclude all obvious outliers. We also impose a data quality cut, keeping only the clusters for which the $2\sigma_{logT}$ temperatures errors are relatively small ($2\sigma_{logT} < 0.075$). The remaining data is fit and the σ rms in $log(L_x/E(z))$ is determined. Any points at greater than $n_{rej} \times \sigma$ from the current iteration's mean relation are omitted from the following iteration. The fit is iterated to convergence. A large portion of the scatter is expected to be intrinsic and not due to measurement errors. To account for this intrinsic scatter in the fit we calculate the total scatter by the following:

$$\sigma = \sqrt{\sigma_{rms}^2 + \sigma_{int}^2} \tag{6.2}$$

The value of σ_{rms} is calculated by including only those points which are not rejected in the current iteration and σ_{int} is a constant chosen to be 0.168 such that the final reduced $\chi^2 \approx 1$ for all data. We experiment with a range in n_{rej} and initial values of the fit parameters. The algorithm is stable for $0.7 \leq n_{rej} \leq 1.8$. The fraction of data used in the final fit within this range is 55.6% for $n_{rej} = 0.7$ and 94.4% for $n_{rej} = 1.8$. If n_{rej} is any smaller than this range the algorithm rejects too much of the data and the fit is poorly constrained. If n_{rej} is any larger than this range all of the data is accepted and the fit is strongly biased by the outliers. The fitting routine is insensitive to the choice of initial α and β, converging on the same α and β for a wide range in reasonable initial values. The overall best values for the fit parameters in equation 6.1 are $\alpha = 3.01 \pm 0.19$ and $\beta = 42.76 \pm 0.17$. These values and their errors are taken respectively as the mean and the rms variation of the distribution of best fit values across the stable range of n_{rej}. The value of α found here is somewhat steeper than that found in previous studies of clusters at the high luminosity end of the cluster distribution. It should be noted however that Markevitch (1998) finds a steepening in alpha after correcting for cooling flows. Our result is qualitatively consistent with the idea that the outliers in the distribution,

predominantly those clusters thought to contain dense cool cores, tend to bias the L_x-T_x relation towards lower values of α. We note that our value of α is in agreement with the consistent the Arnaud & Evrard (1999) value of $\alpha = 2.88 \pm 0.15$ within 1σ and the Markevitch (1998) value of $\alpha = 2.64 \pm 0.27$ at the 2σ level.

Figure 6.1 shows the resulting fit for $n_{rej} = 1.5$ and corresponds to 85.6% of the available data being included in the final iteration. The solid line represents the best fit to the data. The open black triangles show the data that was rejected while filled symbols show the data that was used in the final iteration. The 5 keV temperature selection criterion is shown as a vertical dashed line. Assuming that scatter in the diagram drives systems in a direction perpendicular to the mean relation, we calculate the limit at which a cluster at 2σ from the mean drops out of the sample. This limit is shown as a dotted line and reveals where the sample may begin to be biased. Although the data below this limit are used in the fitting procedure, we find that the do not significantly influence the result if left out. This is perhaps owing to the fact that the data do not seem to be drawn from a gaussian distribution as can be seen by the fact that 94.4% of the data lies inside 1.8σ as opposed to 90.0% inside 2.0σ for a gaussian. Note that the bias line does not appear perpendicular to the mean relation in figure 6.1 simply because of the scale used (ie., a range of 2 in $logL_x/E(z)$ and 0.6 in $logT_x$).

6.3 Central color gradient

The L_x-T_x relation for the selected CCCP clusters is shown in the upper panel of figure 6.2. The data has been corrected to our cosmology and scaled by E(z) to compensate for the evolution in the cosmic background density. The mean relation for the subset of high T_x clusters from the ASCA cluster catalogue of Horner (2001) is shown as a dotted line (see section 6.2). The open triangles (blue) show those clusters that contain BCGs with positive central color gradients; $\frac{d(g'-r')}{dlog(r)}(3 \leq r \leq$

$15h_{70}^{-1}kpc) \geq 0$. Cool core clusters are known to be located on the high L_x side of the scatter in the L_x-T_x diagram. It is therefore highly suggestive that since the BCGs with blue cores are hosted by clusters that also lie in this region of L_x-T_x space, that these galaxies owe their anomalous color to the cooling of the ICM and subsequent formation of a young stellar population in these systems.

In the lower part of figure 6.2 we show the relationship between $\Delta log(L_x/E(z))$ of the host cluster and the central color gradient of the BCG ($3 \leq r \leq 15h^{-1}kpc$). Triangles represent those BCGs with positive central color gradients. There are two features of this diagram that are important to note. Firstly, most BCGs have identical central color gradients (within the errors) indicative of a slow trend toward bluer colors with radius. This picture is qualitatively compatible with the presence of age/metallicity gradients in BCGs. The second interesting feature of this diagram is that those BCGs that do not show this behavior, instead having a strong trend towards bluer colors with decreasing radius, all have very high values of $\Delta log(L_x/E(z))$. The clusters that contain blue core BCGs in this diagram are easily picked out by examination of the color gradients in figures 5.5, 5.6 and 5.7. They are 3C395, Abell 1835, Abell 2204, RXJ1347 and CL0910. It is interesting that there is such a striking difference in color gradient between the clusters with blue cores and those without. These features cannot be fully explained however by a simple model of BCG central star-formation scaling directly with the strength of the cooling of the ICM. Although the blue core BCGs tend to be associated with the high $\Delta log(L_x/E(z))$ of their hosts, there are still some high $\Delta log(L_x/E(z))$ clusters with red BCGs. Any model that tries to explain the enhanced star formation in BCGs by invoking mass deposition from the cooling ICM must also be able to explain why there are red BCGs in some cool core clusters. It is possible that some of these differences may be explained by requiring that central star formation in cool core clusters must be triggered by a dynamical interaction with a passing substructure. It is also possible that some of the red BCGs in cool core cluster

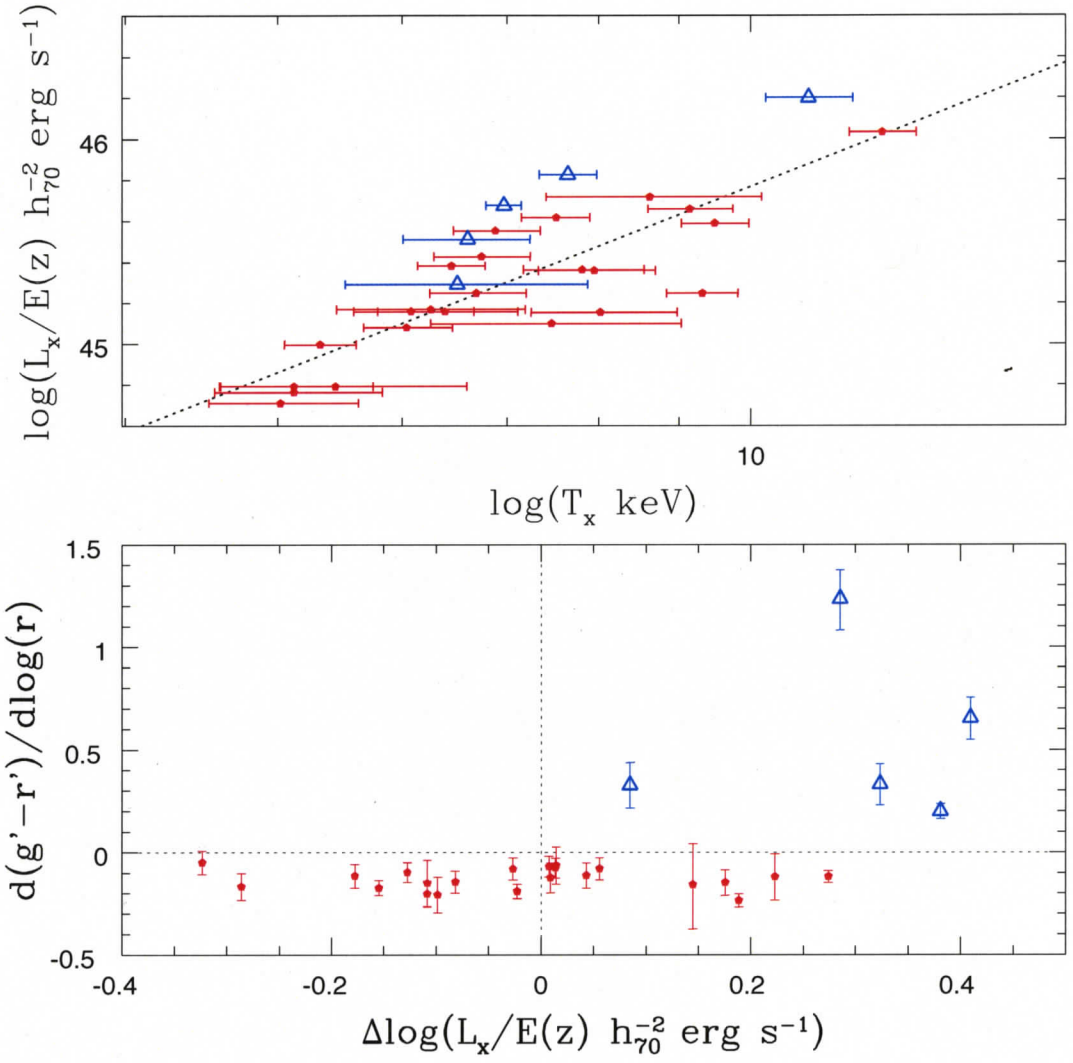

Figure 6.2: The L_x-T_x relation and BCG inner color gradient. Top: L_x-T_x for cluster in the CCCP sample. Blue triangles indicate cluster that contain BCGs with steep central color gradient (blue cores). Bottom: Color gradient vs. offset in L_x from the mean L_x-T_x relation at a given T_x (cooling parameter). Note the blue core BCGs lie at the far end of the offset in L_x.

systems may be due to the BCG lying outside of the cluster cooling region.

6.4 BCG Luminosities

The cooling flow model for galaxy clusters has been a subject of great debate in X-ray astronomy. Early models predicted too much cooling and star formation that was simply not observed. The lack of observed wide-spread star formation in cool core clusters created a need to incorporate non-gravitational heating mechanisms into cluster formation models in order to balance the cooling. There is evidence however, from recent observations (Crawford et al. 1999, Wilman et al. 2006) indicating that indeed some cool core clusters are hosts of high visible star formation rates (eg., Abell 1835: $SFR \sim 100 M_{\odot} yr^{-1}$; Abell 2204: $SFR \sim 1 M_{\odot} yr^{-1}$). In these systems the radiative cooling losses do not fully balance the heating. The resulting view of the cluster cooling problem is one in which radiative cooling is in equilibrium with the heating from various sources and star formation proceeds in those clusters that have the shortest cooling times. The chance of observing star formation in cluster cores is likely to be determined by AGN duty cycles, replenishment rates of the cold gas reservoirs as well as the elapsed time intervals between successive interactions of passing satellites with the core and the overall dynamical state of the cluster. In order to try and understand and quantify the importance of the cooling state of a cluster in contributing to the building of the central galaxy, we plot the total B-band magnitude of the BCG versus $\Delta log(L_x/E(z)h_{70}^{-2} ergs^{-1})$. The total r'-band flux of the BCG is calculated by:

$$F_{r',tot} = 2 \int_0^{2\pi} \int_0^{r_e} I_{r',mod} r dr d\theta \tag{6.3}$$

where $I_{r',mod}$ is the $r^{1/4}$ model intensity defined by equation 3.5 with the background term excluded. This flux is then converted into a total B magnitude using:

$$M_{B,tot} = -2.5logF_{r',tot} - E(r'_z - B_0) - 5logD_L - 25 \quad (6.4)$$

with D_L luminosity distance and $E(r'_z - B_0)$ conversion from observed r' to rest frame B. We note that because this calculation relies on the success of the surface brightness fits and it will not return an accurate value for the total BCG magnitude in the case where the fit does not accurately represent the BCG component of the profile. There will also be error in $M_{B,tot}$ for the clusters that lie on lines of sight passing near bright foreground stars. For these reason we leave out any systems for which these complications are apparent.

Figure 6.3 displays the relationship between BCG $M_{B,tot}$ versus L_x offset from the mean L_x-T_x relation derived in section 6.2. There seems to be a general increase in BCG magnitude with increasing offset from the L_x-T_x relation. The data is binned according to projected offset of the BCG center from the peak of the X-ray distribution. X-ray peak positions are taken from either Chandra or XMM-Newton. The five bins correspond to the following intervals:

$R_{offset} \leq 10kpc$

$10kpc < R_{offset} \leq 20kpc$

$20kpc < R_{offset} \leq 40kpc$

$80kpc < R_{offset} \leq 80kpc$

$R_{offset} > 80kpc$

The binned data is represented by increasing point size for increasing projected BCG-X-ray offset. Those clusters for which no high resolution X-ray data is available are plotted with open symbols. It is immediately apparent that the clusters that have the largest projected BCG-X-ray offsets are also the major outliers from the correlation. A least squares fit to the full range of data results in $M_{B,tot} = -1.29\Delta log(L_x/E(z)) - 22.77$ and is shown as a solid line in figure 6.3. If we concentrate on the clusters that have the smallest projected offsets ($R_{offset} \leq 20kpc$) there is a much tighter correlation. A least squares fit to these clusters with small

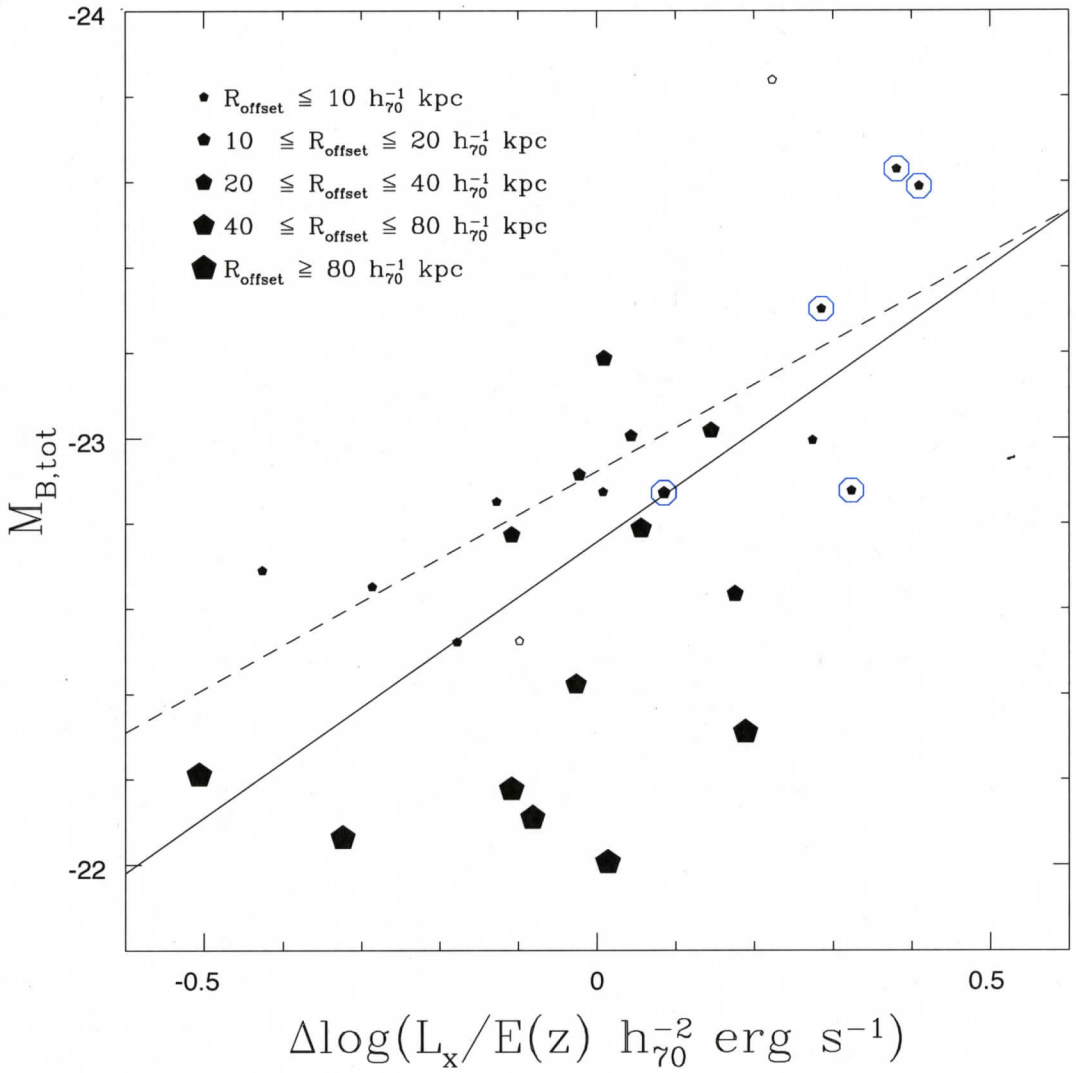

Figure 6.3: BCG total magnitude in the B band versus $\Delta log(L_x/E(z))$ binned in BCG projected offset from the X-ray peak (R_{offset}). Blue core BCGs are identified with blue circles. The solid line represents a least squares fit to all the data while the dashed line is a least squares fit to the BCGs that lie at $R_{offset} \leq 20h_{70}^{-1}kpc$. The total magnitude of the BCG correlates with the residual from the mean L_x-T_x of its host cluster: $M_{B,tot} = -1.36\Delta log(L_x/E(z)) - 22.77$ for small offset systems. Outliers from the trend have large offsets. Open symbols represent the systems for which no X-ray data is available and so no offset is determined.

projected offsets gives $M_{B,tot} = -1.02\Delta log(L_x/E(z)) - 22.92$ and is shown as a dashed line in the figure. We interpret these data as a positive correlation between the cooling state of the cluster gas and the total mass in stars of the BCG for systems where the BCG is situated near the peak of cluster gas emission. It is interesting to note that although only the clusters at the high luminosity end of the scatter in the L_x-T_x relation display the observable signature of active star formation (see figure 6.2), the trend in total BCG luminosity spans the entire range of scatter in L_x-T_x. It is also interesting that the trend accounts for a difference of over one magnitude in BCG luminosity across the full observed range in $\Delta log(L_x/E(z))$ which is an especially important detail for the use of BCGs as "standard candle" distance indicators. The interpretation presented here is reinforced by the fact that the BCGs with large projected offsets have significantly smaller magnitudes than those with small offsets. This behavior is easily understood if the BCGs in these clusters lie outside the cooling region r_{cool} of the ICM and therefore do not undergo the cold gas replenishment that is required in order to form new stars and grow via this mechanism.

The existence of the trend seen in figure 6.3 implies that whatever is responsible for producing the scatter in the L_x-T_x relation is also assisting in the growth of stellar content of BCGs. If we interpret the scatter in the L_x-T_x relation to be caused by the variation in cooling properties from one cluster to another, it is natural to assume that the cooling is also partly responsible for the difference in total magnitude of the BCG. If this is the case however, the star formation in the BCG central regions cannot be in a steady-state mode and must proceed in intermittent bursts in order to account for the lack of a continuous trend in central color gradient with $\Delta log(L_x/E(z))$ (see figure 6.2).

We must caution the reader that the interpretation of BCG luminosity increase by the cooling out of material from the ICM is only one of the possible interpretations of the data. There are other mechanisms than the balance of heating and

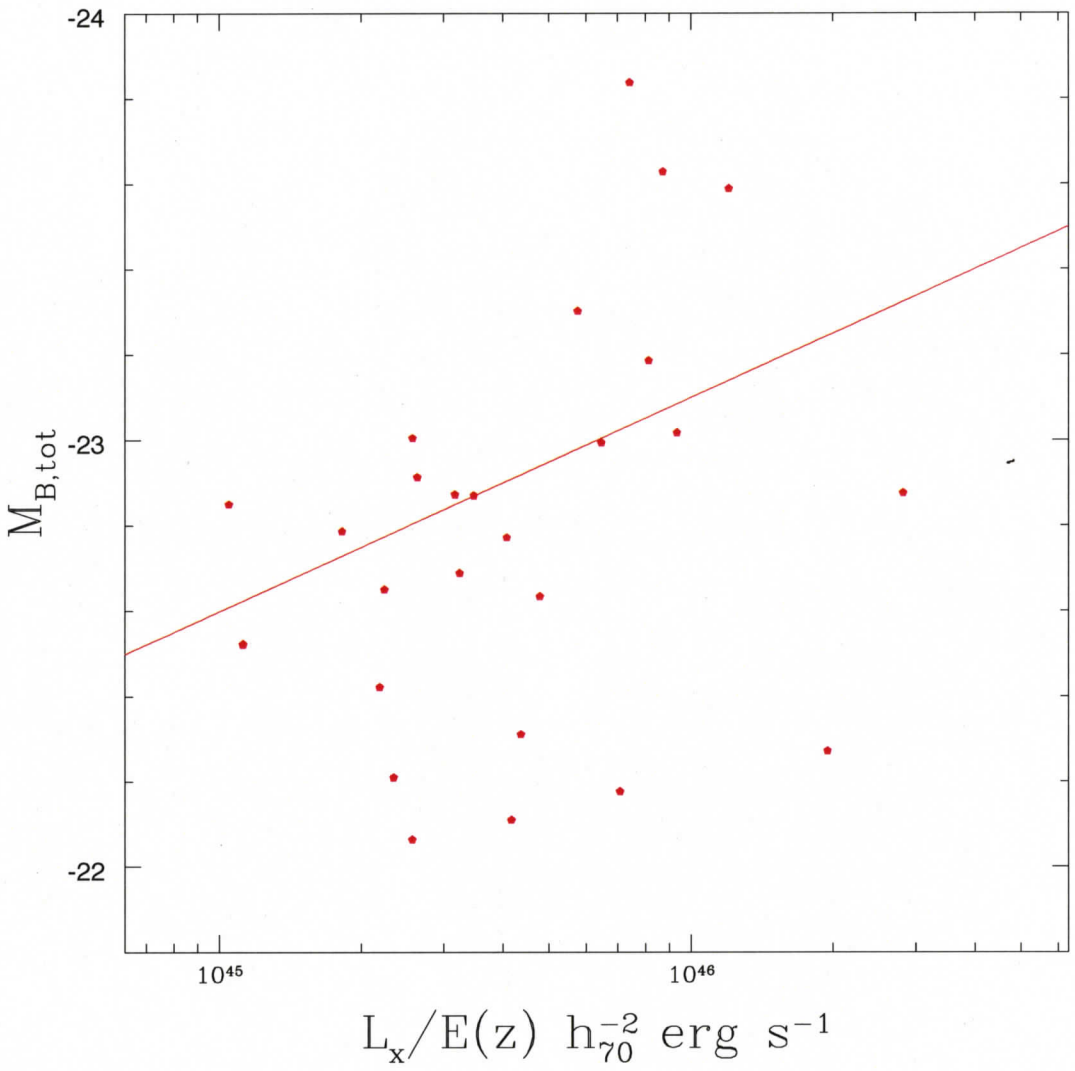

Figure 6.4: BCG total magnitude (corrected to B-band) versus X-ray luminosity of the host cluster. The solid line is a least-squares fit to the data.

cooling by which one can create scatter in the L_x-T_x relation. It has also been proposed that scatter may be introduced by mergers with massive substructures and the intrinsic variation of the underlying dark matter halo density profiles. Recent papers by Randall et al. (2002), Ritchie & Thomas (2002), Rowley et al. (2004) and Kay et al. (2006) show that although merging in clusters is capable of affecting scat-

ter in the X-ray scaling relations, this scatter is short lived and does not account for the degree of scatter seen in the observations. In addition, recent work by Balogh et al. (2006) shows that the variation in dark matter density profiles introduces some scatter but that the scatter introduced is also not sufficient to reconcile the observations. Another caveat of our interpretation is that it does not seem explain the large scatter seen in figure 6.3. This scatter highlights the over-simplicity of our interpretation. It is possible that effects such as the BCG's distance from the ICM cooling region, as well as the overall dynamical relaxation state of the cluster as a whole may complicate this picture somewhat.

We show in figures 6.4 and 6.5 the BCG $M_{B,tot}$ versus L_x and T_x respectively of their host clusters. There is some indication of correlation in BCG total magnitude and X-ray luminosity. This correlation is related to that seen in figure 6.3 for two reasons. Firstly the clusters with positive $\Delta log(L_x/E(z))$ are more likely to also have values of L_x that are greater than the mean L_x of the sample. Secondly, because the CCCP sample is not complete, there is a correlation in the data between $\Delta log(L_x/E(z))$ and $L_x/E(z)$ in the sense that there are more high $\Delta log(L_x/E(z))$ objects at high $L_x/E(z)$ and more low $\Delta log(L_x/E(z))$ objects at low $L_x/E(z)$. The correlation between $\Delta log(L_x/E(z))$ and $L_x/E(z)$ is shown in figure 6.6. L_x is also quite sensitive to the existence of a cool compact core as can be seen from the cooling function (see equation 5.1); which depends upon the square of the density and only weakly on the temperature. If we believe that there is link between BCG magnitude and host cluster X-ray luminosity we must also be able to explain the extreme outliers from the general trend in figure 6.4. One of these outliers is the cluster RXJ1347.5-1145 which is the brightest known X-ray source in the sky and lies at the extreme L_x end of the diagram. This object also has a very high value of T_x possibly enhanced by the fact that it seems to be undergoing a massive merger (Cohen & Kneib 2002). The effect of the merger could be elevating both L_x and T_x without significantly affecting $\Delta log(L_x/E(z))$ (Poole et al. 2006).

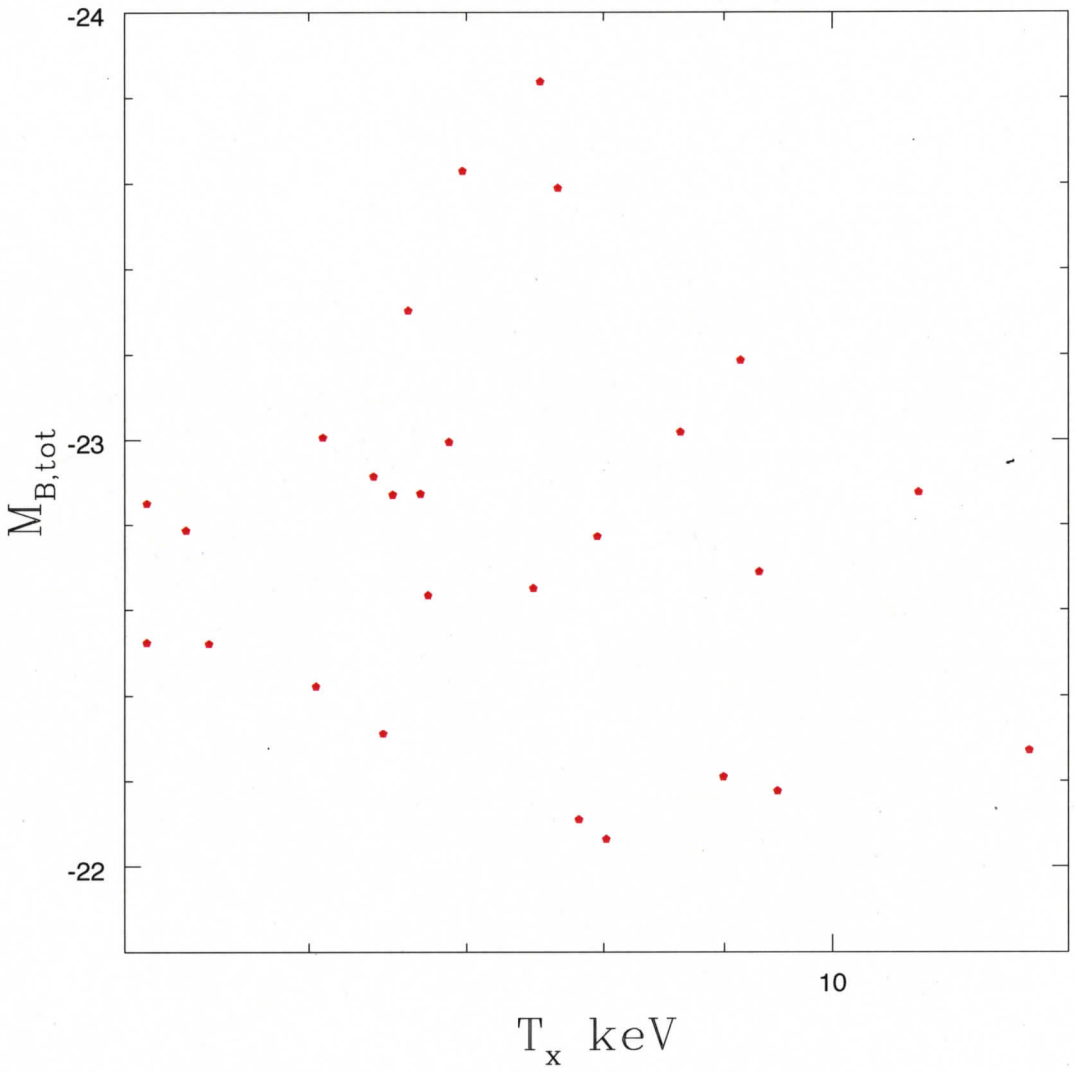

Figure 6.5: BCG total magnitude (corrected to B-band) versus X-ray temperature of the host cluster. There is no obvious correlation of BCG magnitude with X-ray temperature (mass proxy).

In contrast to the trend seen with L_x, the BCG total luminosity does not seem to correlate at all with cluster T_x (figure 6.5). Since the X-ray temperature is known to correlate with cluster mass and X-ray luminosity, the apparent lack of a correlation between $M_{B,tot}$ and T_x may seem odd. It implies that on average,